Novel Antiferromagnets for Spintronic Devices

Teodor Huminiuc

Doctor of Philosophy

University of York

Physics

April 2017

Abstract

Spin electronic or spintronic devices which are used in hard disk drive (HDD) read heads are expected to replace the current silicon based transistor technology used in volatile memories. A prime example for the net advantage of employing spin rather than electric charge manipulation is found in the newly developed magnetic random access memory (MRAM) which is proposed as a replacement for the dynamic random access memory (DRAM) based on three terminal metal-oxide-semiconductor (MOS) devices. Besides the decrease of energy consumption by a factor three arising from manipulating electron angular momentum, the magnetic memories are non-volatile hence they do not require constant power to store information. This allows for additional energy saving due to data stability when the storage device is powered off.

This work is focused on finding a suitable and cost effective replacement for the highly anisotropic and corrosion resistant IrMn and PtMn antiferromagnetic (AF) alloys. AF materials exhibit a temperature dependent compensated antiparallel arrangement of the atomic magnetic moment. When a ferromagnetic (F) material is in close contact with an AF and the structure is cooled in a magnetic field through or from near the Neel temperature of the AF, magnetic coupling via exchange bias is observed as a shift of the hysteresis loop of the ferromagnet. Ternary full-Heusler alloys which have the chemical formula X_2YZ were chosen as a starting point for this study as their magnetic properties can easily be tuned by atomic substitution and among more than 3000 reported compositions, a small number of candidates such as Fe_2VAl and Ni_2MnAl and Ru_2MnGe were predicted or shown to have thermally stable AF configuration. Ru_2MnGe was found to have the most thermally stable AF phase at 126 K. The low temperatures required for thermal stability of the AF properties are caused by the intrinsically non anisotropic cubic structure of the Heusler alloys. The study extends to the binary tetragonal antiferromagnetic compound MnN which has shown some desirable properties such as thermal stability and increased pinning strength. The compound induces a loop shift of 1.4 kOe when coupled to a ferromagnetic layer and the exchange bias vanishes at 388 K. Although MnN satisfies the industrial standards for magnetic pinning, the minimum thickness of the compound and seed layer need to be decreased.

Contents

Abstract..2

List of figures..6

List of tables.. 10

Declaration.. 11

1 Introduction..**12**

1.1 Note on Units and Errors..17

2 Heusler Alloys..**18**

2.1 Heusler Alloy Structures..18

2.2 Electronic Structure and Band Gap in Heusler Alloys................21

2.3 Generalised Slater-Pauling Rule for Heusler Alloys..................24

2.4 Antiferromagnetic Heusler Alloys...27

3 Magnetoresistance and Spintronic Devices..................................**32**

3.1 Magnetoresistance..32

3.1.1 Giant Magnetoresistance (GMR)...................................33

3.1.2 Applications of GMR..37

3.2 Current Induced Magnetisation Switching.............................38

3.3 Tunnelling Magnetoresistance...40

3.4 Magnetic Random Access Memory (MRAM)............................43

4 Exchange Interactions...**46**

4.1 Direct Exchange..46

4.2 Indirect Exchange..48

4.3 Magnetic Anisotropies...50

4.3.1 Magnetocrystalline Anisotropy......................................50

4.3.2 Exchange Anisotropy...52

4.3.3 Other Anisotropies...53

4.4 Magnetisation Reversal..54

4.4.1 Domain Structures..54

4.4.2 Domain Wall Motion 55
4.5 Single Domain Particles 57
4.5.1 Magnetisation Coherent Rotation 58
5 The York Model of Exchange Bias..60
5.1 Energy Barriers..61
5.2 Time Dependence..62
5.3 The Setting Process 63
5.4 Grain Volume Distribution..65
5.5 The Blocking Temperature in Antiferromagnets 66
5.6 The Anisotropy Constant...68
5.7 Grain size and Film Thickness Dependence 69
6 Sample Fabrication and Magnetic Characterisation 72
6.1 Methods of Thin Film Deposition...72
6.1.1 Magnetron Sputtering 72
6.1.2 High Target Utilisation Sputtering (HiTUS).................76
6.2 Sample structures...78
6.3 Magnetic Characterisation..81
6.3.1 Alternating Gradient Force Magnetometer 82
6.3.2 Vibrating Sample Magnetometer...................................84
6.3.3 The York Protocol for Exchange Bias Measurements ...87
7 Structural and Chemical Characterisation.................................89
7.1 X-Ray Diffraction...89
7.1.1 Scherrer Analysis..93
7.2 Energy Dispersive Spectroscopy (EDS) 94
7.3 Transmission Electron Microscopy (TEM)................................97
7.3.1 Scanning Transmission Electron Microscope (STEM) 102
7.3.2 Cross-sectional TEM 104
8 Novel Antiferromagnets for Spintronic Devices 108
8.1 Alloy Selection 108

8.2 Chemical Analysis of Polycrystalline Heusler Alloys 110
8.3 Structural Characterisation of Polycrystalline Fe_2VAl 111
8.4 Magnetic Characterisation of Polycrystalline Fe_2VAl.........115
8.5 Structural Characterisation of Polycrystalline Ni_2MnAl....117
8.6 Magnetic Characterisation of Polycrystalline Ni_2MnAl 121
8.7 Structural Characterisation of Epitaxial Ni_2MnAl 124
8.8 Magnetic Characterisation of Epitaxial Ni_2MnAl.....................129
8.9 Structural, Magnetic and Electric Characterisation of Ru_2MnGe..130
8.9.1 Epitaxially Deposited Ru_2MnGe 130
8.9.2 Integration of Epitaxial Ru_2MnGe in Spintronic Devices 135
8.9.3 Polycrystalline Ru_2MnGe 138
9 Structural and Magnetic Properties of Polycrystalline MnN ..142
9.1 Polycrystalline MnN Deposited via Reactive Magnetron Sputtering...143
9.2 Polycrystalline MnN Deposited via Reactive HiTUS Sputtering 148
10 Conclusions and Future Work 151
10.1 Conclusions 151
10.1.1 Polycrystalline Heusler Alloys 151
10.1.2 Epitaxial Heusler Alloys...153
10.1.3 The Tetragonal AF Compound MnN 154
10.2 Future Work...155

List of symbols…………………………………………………..157
List of abbreviations…………………………………………….....161
References………………………………………………………164

List of figures

Figure 1.1: Increase of areal density in HDDs with read head and recording media technology [3]. 12
Figure 1.2: a) Schematic diagram of the spin valve structure and b) the corresponding cross sectional TEM image of a TMR HDD read head [5]....... 13
Figure 1.3: Schematic diagram of a 1 transistor-1 MTJ memory cell and typical voltage induced switching for a MgO based MTJ [9]....... 15
Figure 1.4: Abundance (atom fraction) of chemical elements in Earth's upper continental crust [18]....... 16
Figure 2.2: CsCl structure and Heusler structure shifted by ¼ on x, y and z axis [32]. 19
Figure 2.3: Overview of the most common type of ordered and disordered Heusler structures [32]....... 20
Figure 2.4: Total DOS for Co_2MnZ compounds where Z = Al, Si, Ge, Sn [38]. 22
Figure 2.5: Hybridisation between *d* orbitals for minority states for Co_2MnGe considering a) the Co-Co interaction and b) the Mn-(Co-Co) interaction. The shape of the different *d* orbitals are shown in a) [40]....... 23
Figure 2.6: Generalised Slater-Pauling rule for full Heusler alloys [38]. 26
Figure 2.7: a) Magnetisation loops for Ni_2MnAl deposited at increasing substrate temperatures and b) exchange bias of Heusler alloy bilayer system [21]....... 29
Figure 3.1: Schematic diagram of the GMR effect and spin-dependent scattering using a resistor network model [75]....... 34
Figure 3.2: Schematic diagram of "current in the plane" (CIP) and "current perpendicular to the plane" (CPP) GMR geometries [40]. 35
Figure 3.3: a) Schematic representation and b) magnetisation and transport measurements for a top-pin type exchange bias spin valve using the $Co_2FeAl_{0.5}Si_{0.5}$ Heusler alloy [84]....... 36
Figure 3.4: Schematic diagram of the read-write system in HDD and the bit transition with in granular recording media [86] [87]....... 37
Figure 3.5: Schematic representation of a spin wave or magnon [91]....... 38
Figure 3.6: Schematic diagram of the device used for current and magnetisation induced switching for Co/Cu/Co GMR structure [90]....... 39
Figure 3.7: Schematic diagram of quantum tunnelling [92]. 40
Figure 3.8: Schematic representation of TMR mechanism according to the two current model and DOS of the ferromagnetic layers [40]....... 41
Figure 3.9: Cross sectional TEM images of MTJ crystallising in post annealing experiment [103]....... 42

Figure 3.10: Schematic representation of (a) conventional and (b) spin transfer torque MRAM cells [103]. 44
Figure 4.1: Dependence of the exchange integral on the atomic separation normalised to the radius of *d* orbitals at 0 K [116]. 48
Figure 4.2: Dependence of indirect exchange coupling on the thickness of Cr spacer layer between two 2 nm thick Fe layers at 4.5 K [117]. 49
Figure 4.3: Magnetisation curves for bcc iron along different crystal axes [116]. 51
Figure 4.4: a) Shifted hysteresis loop and b) torque variation showing uniaxial induced anisotropy for the Co/CoO nanoparticle system [51]. 52
Figure 4.5: Division of a single crystal into domains [116]. 55
Figure 4.6: Schematic representation of (a) domain wall formation (b) domain wall movement (c) magnetisation rotation (d) and saturation magnetisation in a ferromagnetic material [116]. 56
Figure 4.7: a) Schematic diagram of domain wall movement and corresponding Barkhausen effect [116] b) epitaxial Ru_2MnGe/Fe magnetisation loop where the reversal mechanism is based on rapid domain wall motion. 57
Figure 4.8: a) Schematic diagram of a Stoner-Wolfarth elongated particle and b) the associated hysteresis loops for different angles of the applied magnetic field [120]. 58
Figure 5.1: Time dependence of H_{EX} for the AF setting process [132]. 64
Figure 5.2: Magnetic viscosity as a function of TSET [132]. 64
Figure 5.3: The grain volume distribution showing the critical volumes. 65
Figure 5.4: Standard thermal activation process compared to the York protocol [83]. 67
Figure 5.5: Grain volume distributions and critical volumes for varying thicknesses of IrMn [138]. 70
Figure 5.6: Variation of H_{ex} with t_{AF} and grain diameter for IrMn/CoFe [138]. 71
Figure 6.1: Schematic diagram of a radio frequency (RF) magnetron sputtering system [142]. 74
Figure 6.2: Unevenly eroded Ta magnetron target. 75
Figure 6.3: Schematic diagram of the HiTUS sputtering system. 76
Figure 6.4: Powder pressed custom drilled target with doping pegs. 77
Figure 6.5: Schematic diagram of Heusler alloy sample structure for XRD analysis. 79
Figure 6.6: Schematic diagram of the relative position of a Heusler alloy unit cell in relation to a single crystal MgO substrate [40]. 79
Figure 6.7: Schematic diagram of the exchange biased stack using Cr/Ag seed layers. 80
Figure 6.8: Cross sectional TEM image of the MnN/CoFe specimen. 81
Figure 6.9: Schematic diagram of Micromag 2900 AGFM [40]. 83
Figure 6.10: Schematic diagram of ADE model 10 vector VSM. 85
Figure 6.11. Schematic diagram of measurement steps of the York Protocol and representation of the grain size distribution function [83]. 88
Figure 6.12: Hysteresis loops and blocking temperature graph used for determining K_{AF}. 88

Figure 7.1: Schematic diagram of out of plane and in plane X-ray diffraction measurements [156]. 90
Figure 7.2: Schematic diagram of a rocking curve measurement[157]. 91
Figure 7.3: Schematic representation of in plane pole figure scan [160]....................92
Figure 7.4: Representation of kinematical diffraction on a polycrystalline thin film [158]. 93
Figure 7.5: Schematic diagram of SEM [165]. 95
Figure 7.6: Schematic representation of the electron beam interaction in SEM [164]. 96
Figure 7.7: a) Schematic diagram of bright field (BF) TEM operation with image. b) Schematic diagram of diffraction mode operation with a diffraction pattern. 98
Figure 7.8: Bright field and dark field TEM images. 100
Figure 7.9: Schematic diagram of spherical aberration induced by a conventional electromagnetic lens and correction using a divergent multipole lens. 101
Figure 7.10: Schematic diagram of bright field (BF) and high angle annular dark field (HAADF) scanning tunnelling electron microscopy (STEM). 103
Figure 7.11: Schematic representation of a cross-sectional TEM a) specimen before thinning and b) during the ion polishing step. 105
Figure 7.12: Schematic diagram of a liquid metal ion source (LMIS) in FIB [169]. 106
Figure 7.13: a) Strip of platinum deposited on top of the lamella. b) Cutting pattern set for the automatic FIB control. c) Separation of the lamella from the sample. d) End result after thinning the specimen. 107
Figure 7.14: Diffraction pattern and Kikuchi lines corresponding to the MgO(001) zone axis. 107
Figure 8.1: XRD spectra for Fe_2VAl annealed at elevating temperatures. 112
Figure 8.2: Q factor graph for Fe_2VAl annealed at elevating temperatures. The positions of the (220) Heusler peaks are recorded below data points. 113
Figure 8.3: X-ray diffraction pattern of Fe_2VAl deposited increasing values of V_B. 114
Figure 8.4: X-ray diffraction pattern of Fe_2VAl deposited at -300V. 115
Figure 8.5: Hysteresis loop for the post annealed Fe_2VAl. 116
Figure 8.6: Hysteresis loops for post annealed Fe_2VAl deposited at -300V. 117
Figure 8.7: X-ray diffraction pattern for Ni_2MnAl deposited at V_B= -300 and -900V. 118
Figure 8.8: X-ray diffraction pattern of Ni_2MnAl deposited on Cr/Ag seed layers. 119
Figure 8.9: Q factor graph for Ni_2MnAl deposited on Cr/Ag seed layer. The positions of the (220) Heusler peaks are recorded below data points. 120
Figure 8.10: Hysteresis loop of the post-annealed Ni_2MnAl/Co_2FeSi bilayer 122
Figure 8.11: Hysteresis loop of the post-annealed Ni_2MnAl/CoFe bilayer. 122
Figure 8.12: Hysteresis loop for the Ni_2MnAl/Co_2FeSi bilayer deposited on Cr/Ag seed layer and annealed at 250°C. 123
Figure 8.13: X-ray diffraction pattern for epitaxial Ni_2MnAl/Fe bilayer deposited on MgO(001) at elevating temperatures [175]. 124

Figure 8.14: a) Cross sectional TEM image and b) corresponding diffraction pattern for epitaxial Ni_2MnAl layer deposited at RT c) MgO (001) substrate/ Ni_2MnAl interface. 125
Figure 8.16: a) Cross sectional TEM image and b) diffraction pattern of the MgO/Ni_2MnAl/Fe bilayer deposited at 600°C where orange circles belong to MgO diffraction spots c) HR-TEM image of the substrate interface. 127
Figure 8.17: X-ray diffraction pattern for epitaxial Ni_2MnAl/Fe bilayer deposited on MgO(001) at elevating temperatures [175]. 128
Figure 8.19: Hysteresis loops for the Ni_2MnAl/Fe bilayers measured at 10, 30 and 100 K. The Ni_2MnAl films were deposited at a) RT and b) 600°C [175]. 129
Figure 8.20: Cross-sectional TEM image of the epitaxially deposited Ru_2MnGe(110)/Fe bilayer on a MgO(001) substrate... 131
Figure 8.21: X-ray diffraction pattern for epitaxial Ru_2MnGe [149]...................... 132
Figure 8.22: a) Hysteresis loop and b) blocking temperature graphs for the epitaxial Ru_2MnGe/Fe exchange bias bilayer. 133
Figure 8.23: Polar plot of the coercivity (black) and squareness (blue) for Ru_2MnGe/Fe. 134
Figure 8.24: Cross sectional TEM image and TMR curve for Ru_2MnGe/Fe/MgO/Fe MTJ [178]. 135
Figure 8.25: TMR curve for Ru_2MnGe/Fe/MgO/Fe MTJ at 3 K: a) majour loop showing the switching of the whole stack b) minor loop showing only the switching of the free ferromagnetic Fe layer [178]. 136
Figure 8.26: a) TMR ration measured at 300 K for post annealed Ru_2MnGe based MTJ stacks. b) Low temperatre multi-domain switching behaviour of the free Fe layer of an MTJ annealed at 250°C [178]. 137
Figure 8.27: Cross-sectional TEM image of the polycrystalline Ru_2MnGe/Fe bilayer. 138
Figure 8.28: a) HR-TEM image of the polycrystalline Ru_2MnGe/Fe bilayer. b) Grain boundary in polycrystalline Ru_2MnGe. 139
Figure 8.29: SEM images of a nanopillar specimen for 3D APT measurements. ... 140
Figure 8.30: Elemental mapping for the polycrystalline Ru_2MnGe/Fe bilayer. 140
Figure 9.1: Representation of unit cells corresponding to different phases and stoichiometries of MnN 142
Figure 9.2: X-ray diffraction pattern for the Ta/MnN/CoFe stack.......................... 144
Figure 9.3: Cross-sectional TEM images of the polycrystalline Ta/MnN/CoFe stack. 145
Figure 9.4: Exchange bias hysteresis loop for MnN/CoFe at room temperature. 146
Figure 9.5: Blocking temperature measurement of the AF polycrystalline θ- MnN. 147
Figure 9.6: XRD spectrum for Ta/MnN/CoFe deposited via HiTUS at -900V. 148
Figure 9.7: BF TEM image and grain size distribution for polycrystalline MnN deposited at V_B = -900V. 149
Figure 9.7: York protocol measurements for θ-MnN deposited via HiTUS........... 150

List of tables

Table 2.1: Lattice parameters and crystal structure of Ru_2MnZ compounds……….30

Table 8.1: Properties of the selected Heusler alloys as reported in the literature….108

Table 8.2: Results of the chemical analysis performed by InterTek……………..110

Table 8.3: Q factor and lattice constant calculation for Fe_2VAl deposited at -900V and post-annealed……………………………………………………………….113

Table 8.4: Q factor and lattice constant calculation for Ni_2MnAl deposited at -300V on a Cr/Ag seed layer and post-annealed…………………………………………120

Declaration

I declare that the work presented in this thesis is based purely on my own research, unless otherwise stated, and has not been submitted for a degree in this or any other university. All sources are acknowledged as references.

1 Introduction

Spin electronics is expected to replace volatile silicon based transistor technology in the near future and it already exists in data storage devices such as hard disk drives (HDDs). The spintronics research field was initiated by the discovery of giant magnetoresistance (GMR) in 1988 by Grünberg and Fert [1, 2] which was implemented in HDDs in 1998 [3]. Although initially, the principles of giant magnetoresistance were proven in simple trilayer structures, the increasing demand and performance of magnetic sensors which was required by the data storage industry resulted in extensive use of exchange bias in read head devices. As the storage capability of disk drives increased, a smaller and more efficient read head was required. This triggered sustained research efforts to try and improve the magnetic and electrical properties of magnetoresistive sensors such as GMR and tunnelling magnetoresistance (TMR) devices. Figure 1.1 shows the exponential increase of storage capacity of HDDs and the emerging read head and recording media innovations.

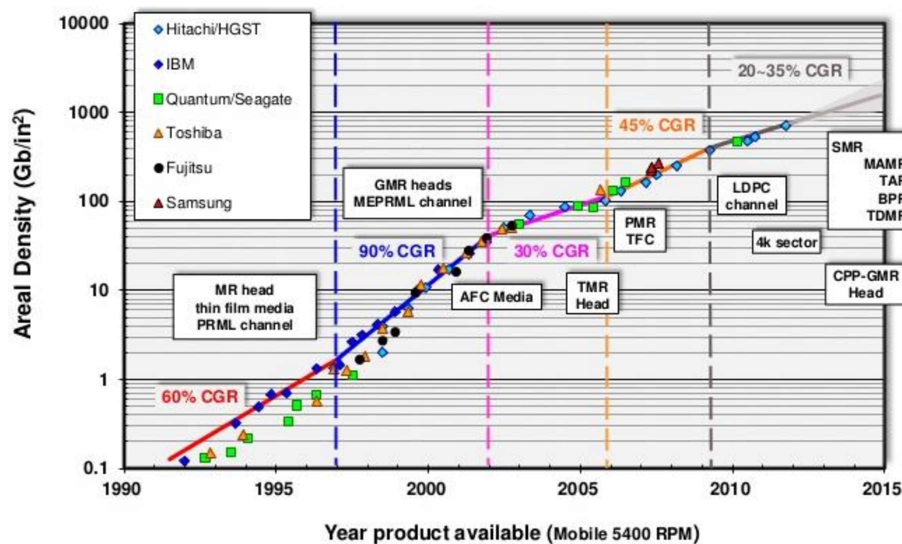

Figure 1.1: Increase of areal density in HDDs with read head and recording media technology [3].

As the data recording industry progressed towards the goal of 1 Tbit/in^2, the read head technology changed from GMR based devices to magnetic tunnel junctions (MTJ) and the first TMR based read head was announced by Segate in 2005 [4]. In order to increase the storage density, a shorter bit length and increased detection sensitivity are required. The bit size can be controlled by modifying the grain size of the recording media while accounting for the changes in time and thermal stability of the material used. The read head needs to have similar dimensions when compared to the recorded bit of information (30-50 nm). Both GMR and TMR devices also known as spin valve structures rely on strong magnetic pinning via exchange bias in order to keep the magnetisation of a "fixed" layer constant while the neighbouring free layer is allowed to align to the direction of the magnetised information bit it passes over. Structurally, GMR and TMR spintronic sensors are very similar except the nature of the spacer layer which is designed to control coupling between the ferromagnetic (F) layers. As the name suggests, the MTJ uses quantum tunnelling through a thin insulating barrier while the GMR sensor is conductive and uses a non-magnetic spacer layer. Figure 1.2 a) shows a schematic diagram of a spin valve device used as a read head in a hard drive.

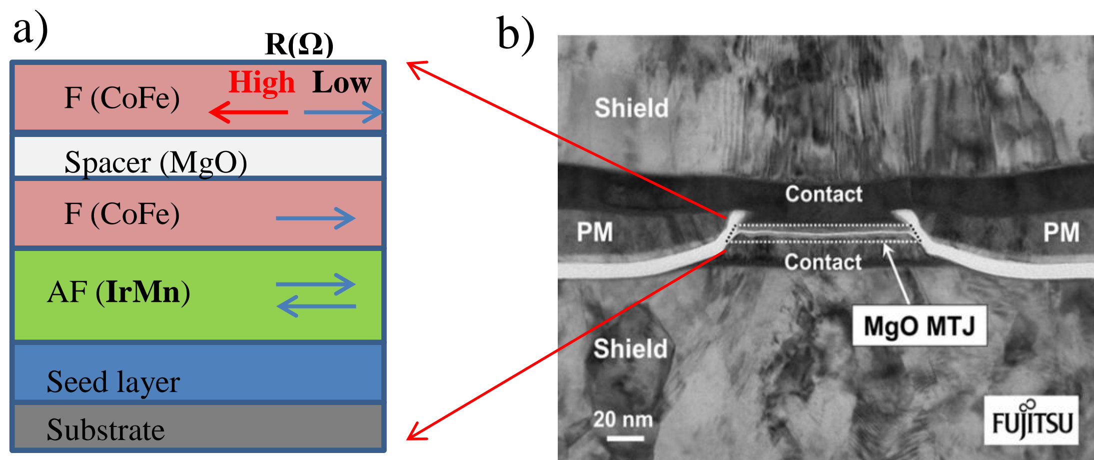

Figure 1.2: a) Schematic diagram of the spin valve structure and b) the corresponding cross sectional TEM image of a TMR HDD read head [5].

As shown in Figure 1.2 a), a spin valve sensor has two resistance states which correspond to the parallel and antiparallel alignment of the F layers. The difference in resistance arises from the amount of scattering induced on a spin polarised current transiting from a F layer to the other with the low resistance state corresponding to

the parallel alignment of the magnetisation. The diagram represents the basic layout of a magnetic sensor where the layers are magnetised in the plane of the substrate.

If the spin valve changes resistance with the reorientation of the free layer when subjected to an external magnetic field resulting in different values of the resistance according to the amount of spin scattering, the inverse mechanism of driving a current through a spin valve structure may induce the switching of the free layer. The phenomenon is known as spin transfer torque (STT) and was predicted to occur at the interface between a ferromagnet and a non-magnetic material when a spin polarised current passes through into the ferromagnetic layer [6, 7]. The spin polarisation occurs when driving a current through preferably a saturated ferromagnetic material where the conduction electrons become spin-polarised. Given enough current density, the polarised electrons can switch the magnetisation direction of the material then by interacting with the localised electron spins.

The current induced switching mechanism became the basis for the development of a new type of memory device which is expected to replace the current complementary metal-oxide-semiconductor (CMOS) based technology. The magnetic random access memory (MRAM) consists of a spin valve structure which can be switched between a low and high resistance state via a small magnetic field generated by a neighbouring ferromagnet (similarly to a HDD read head) or via spin transfer torque induced by a current passing along the spin valve.

The new type of memory has a number of advantages when compared to current semiconductor technology such as non-volatility, nanosecond access time, high storage density potential and reduced power consumption by at least a factor 3. This makes MRAM a worthy candidate for universal memories. Figure 1.3 shows a schematic diagram of a STT MRAM cell which using this design requires an isolation transistor for each cell.

Continuous development of magnetic memories resulted in the recent announcement of a 4Gbit/in^2 density STT-MRAM using perpendicular MTJ realized with compact cell structure” made by *Toshiba Electronics Korea Corporation* at the 62nd International Electron Devices Meeting in December 2016. The chip is expected to be available on the market in up to 2 years [8].

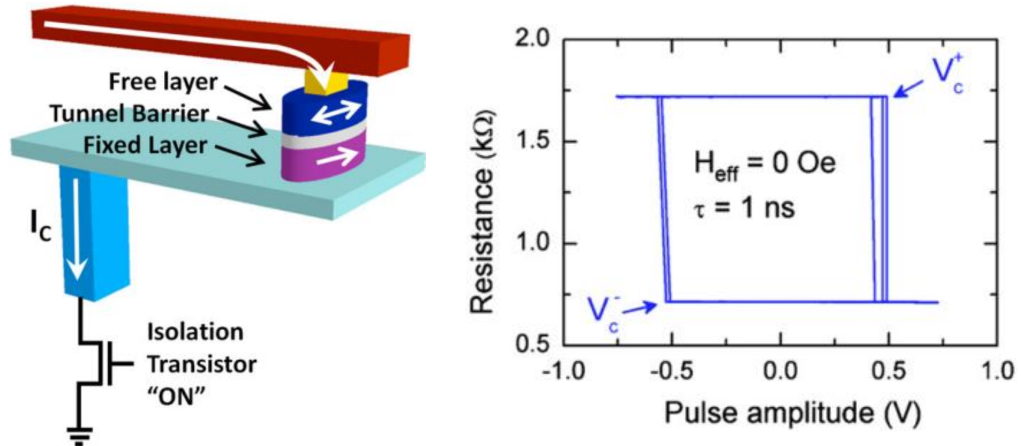

Figure 1.3: Schematic diagram of a 1 transistor-1 MTJ memory cell and typical voltage induced switching for a MgO based MTJ [9].

As research efforts are channelled more towards increasing the efficiency and reducing the power consumption of computing devices as part of a global initiative for creating a more sustainable living environment, important issues arise regarding the abundance of a number of rare metals from the platinum group. A special case in point is iridium which has been extensively used in the spintronics industry as part of the well-known antiferromagnetic (AF) alloy $IrMn_3$. IrMn is the alloy of choice for spintronic applications due to superior chemical stability and very large value of antiferromagnetic anisotropy. The value of the effective anisotropy was determined to be 3.3×10^7 erg/cm^3 which may be the highest value recorded for such a material. The highly anisotropic IrMn has therefore excellent magnetic pinning properties and thermal stability with exchange bias vanishing at $T_B = 477$K [10].

Iridium is a transition metal which belongs to the platinum group and has the second largest bulk density after osmium. Ir is known as the most corrosion resistant metal even at temperatures as high as 2000°C and has a melting point of over 3000°C [11]. The metal is a main constituent of asteroids but it is very scarce on Earth making it far less common than many of the rare metals. As a by-product of processing platinum and palladium ores, iridium is found in concentrations of 1~2%. The concentration of Ir in the Earth's crust is estimated at 4×10^{-4} parts per million (ppm) which is significantly less than other critical metals such as neodymium (33 ppm), lithium (17ppm), dysprosium (6.2 ppm), gold, platinum, ruthenium and palladium

($\sim 10^{-3}$ ppm) [12]. Iridium was reported as the scarcest element by the *United States Geological Survey Agency* as shown in Figure 1.4.

Demand for Iridium has increased drastically in the last decade with a figure in 2010 of approximately 10 tonnes compared to approximately 2 tonnes in 2009 [13]. The rapid increase in the demand for iridium was due to the development of new applications such as HDD read heads and MRAM devices. Some other applications include crucibles for production of single crystal oxides [14], spark plugs [15] and light emitting diodes [16]. This has led to a significant increase in the price of iridium by almost a factor 5 in the last decade [17] which has been caused by the global demand of around 10 tonnes outstripping the global supply of around 6 tonnes per year. The electronics industry has been the main source of new technological applications for iridium compounds.

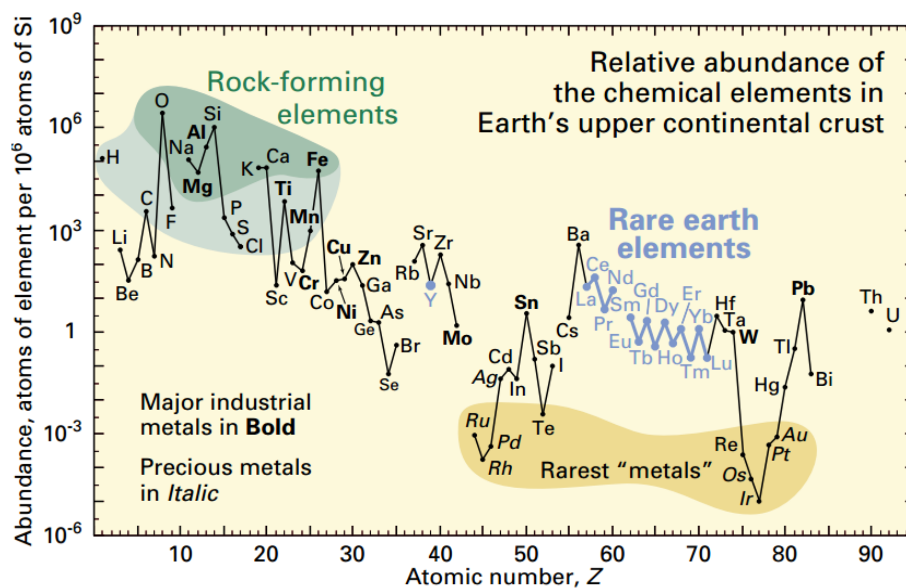

Figure 1.4: Abundance (atom fraction) of chemical elements in Earth's upper continental crust [18].

The only alternative AF material for commercial use is PtMn. The as deposited face centred cubic (fcc) phase requires a transformation into the face centred tetragonal (fct) structure to form AF ordering. This phase transformation requires high temperatures of about 800 K in sheet form and is impractical for many devices because of possible damage to other layers in the stack [19].

The aim of this work is to find a suitable AF material to replace the rare metal Ir alloy. The work is focused mainly on Heusler alloys (HAs) which are known to form AF phases with an fcc crystal structure [20]. The HAs consist of either an XYZ or an X_2YZ formula where X and Y are usually common transition metals (Fe, Co, Ni or Mn) and Z is either a semiconductor or a non-magnetic metal such as Si or Al. The AF phases often form when high moment transition metals such as Ni, Ru, Fe, Co or Mn are part of the composition. All these elements are plentiful and relatively inexpensive compared with iridium or platinum, which are already very expensive and predicted to become more so. HAs have a major advantage because their lattice constant and magnetic structure can be controlled by atomic substitution.

Another advantage of HAs is that the spin magnetic moment can be tuned by modifying the total number of valence electrons in the unit cell [20]. This may allow for designing new antiferromagnetic HAs to satisfy the requirement that the overall spin moment essentially cancels in zero field. A literature survey shows very little experimental work reporting stable AF phases in Heusler alloy thin films [21, 22]. The experiments show that HAs require low temperatures for thermal stability of AF phases. These premises constitute the starting point for the following work which is focused on investigating the origins and implications of novel antiferromagnetic structures in an attempt to find a suitable cost effective replacement for the current AF alloys such as IrMn and PtMn.

1.1 Note on Units and Errors

For this work, the Gaussian c.g.s. unit system was employed throughout as it is the standard system used in the magnetic recording industry which is the main area of application for the materials and techniques presented. The c.g.s. system is widely used by the entire magnetism community. Some of the most common units used in this work are the Oersted (Oe) for the magnetic field strength due to the more applicable dimensions in daily phenomena, the erg (1erg = 10^{-7} Joule) for energy and the unit of magnetic moment, m as emu (emu = erg/Oe).

Where possible, errors on numerical results in graphs and tables presented in this thesis were calculated using the standard Gaussian error technique. When reference values are quoted without error, it is implied that the error is not known.

2 Heusler Alloys

Heusler alloys belong to a special class of compounds with purely metallic or intermetallic constituents. With a usual ternary compound or alloy structure, the Heusler alloy Cu_2MnAl was first reported at the very beginning of the 20th century having ferromagnetic properties despite the non-magnetic nature of the individual elements [23]. There are over 3000 known Heusler alloys and certainly a lot more possible compositions which can be synthesised. Therefore this family of alloys sits among the most versatile materials that can be used in the current storage and memory devices. Some of the properties associated with the Heusler structure are: superconductivity [24], topologically insulated states [25], semiconducting [26], thermoelectric, magneto optical [27] and magneto caloric behaviour [28]. Despite all the different effects found intrinsic to the Heusler structure, the magnetic and transport properties define this class of alloys which is usually associated with half-metallic ferromagnetism [29] and describes the spin polarisation capability of the Heusler alloys. Having control over the spin angular momentum of electrons, the hybrid spintronic research topic has emerged as detailed in this chapter. Finally, a review of abundant antiferromagnetic Heusler alloys and compounds will be presented focusing on materials and techniques suitable for applications.

2.1 Heusler Alloy Structures

All Heusler alloys are defined via a specific atomic arrangement of the unit cell which consists of four interpenetrating face centred cubic (fcc) lattices. There are two main types of ternary Heusler compounds according to the relative elemental ratios. The 1:1:1 stoichiometry also known as the XYZ, half-Heusler or semi-Heusler alloy and the 2:1:1 stoichiometry also known as the X_2YZ or full-Heusler alloy.

The X_2YZ full-Heusler alloys are ternary compounds where X and Y are usually transition metals and Z is a main group element. In some cases the Y position can be replaced by a rare earth element or an alkaline earth metal. The full-Heusler alloys crystallise in a cubic structure which is similar to the half-Heusler unit cell but this time the symmetry is kept in relation to the centre of the atomic arrangement which belongs to space group no 255, $Fm\overline{3}m$. The prototype full Heusler alloy structure is

found in Cu_2MnAl which crystallises in the highly ordered $L2_1$ phase [30, 31]. Similar to the half-Heusler structure, four interpenetrating fcc sublattices form the unit cell which is described in the literature as a CsCl-type superstructure as seen in Figure 2.2. The Heusler structure can be described as a combination of two binary alloys crystallising in the CsCl structure[32].

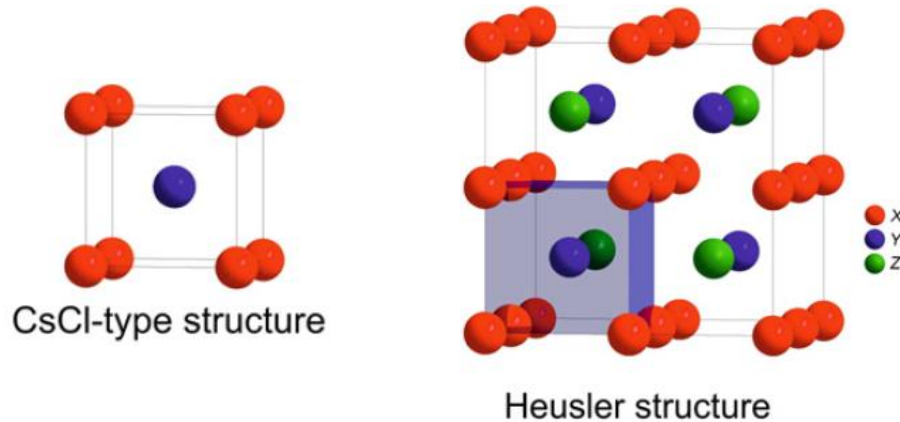

Figure 2.2: CsCl structure and Heusler structure shifted by ¼ on x, y and z axis [32].

The properties of Heusler alloys are strongly dependent on the degree of atomic disorder within the unit cell. Commonly, the highly ordered Heusler alloys crystallise in the $L2_1$ structure. The X element which is known to be the most electronegative transition metal occupies the Wykhoff position 8*c* (1/4, 1/4, 1/4). The Y element can be an electronegative transition metal but also a rare earth or alkaline earth metal positioned on the 4*b* (1/2, 1/2, 1/2) sites. The Z atom can be a main group element and sits on the 4*a* (0 0 0) position [33]. Different variations of the standard $L2_1$ atomic structure can be obtained by intermixing the X, Y and Z elements and their atomic position in the unit cell therefore obtaining different local atomic symmetries and consequent structures [34] as seen in Figure 2.3.

- The DO_3-type structure corresponds to the $Fm\bar{3}m$ space group where the X and Y or X and Z elements are mixed resulting in a BiF_3 structure type.

- The *B*2-type structure is characterised by the intermixing of the Y and Z atoms which leads to a reduction in symmetry (space group $Pm\bar{3}m$). The X atoms are distributed on the 1*b* Wykhoff position while the Y and Z atoms are randomly distributed on the 1*a* position.

- The *A*2-type structure is a total randomly intermixed version of the semi-disordered *B*2 phase where any of the elements can occupy any atomic site. The reduction in symmetry places the structure in the $Im\bar{3}m$ space group which has a tungsten (W) type body centred cubic (bcc) unit cell.

- The *B*32*a*-type structure forms when the X atom of two fcc lattices mix with different atoms in separate sublattices. The corresponding space group becomes $Fd\bar{3}m$. This kind of atomic arrangement is not commonly found experimentally.

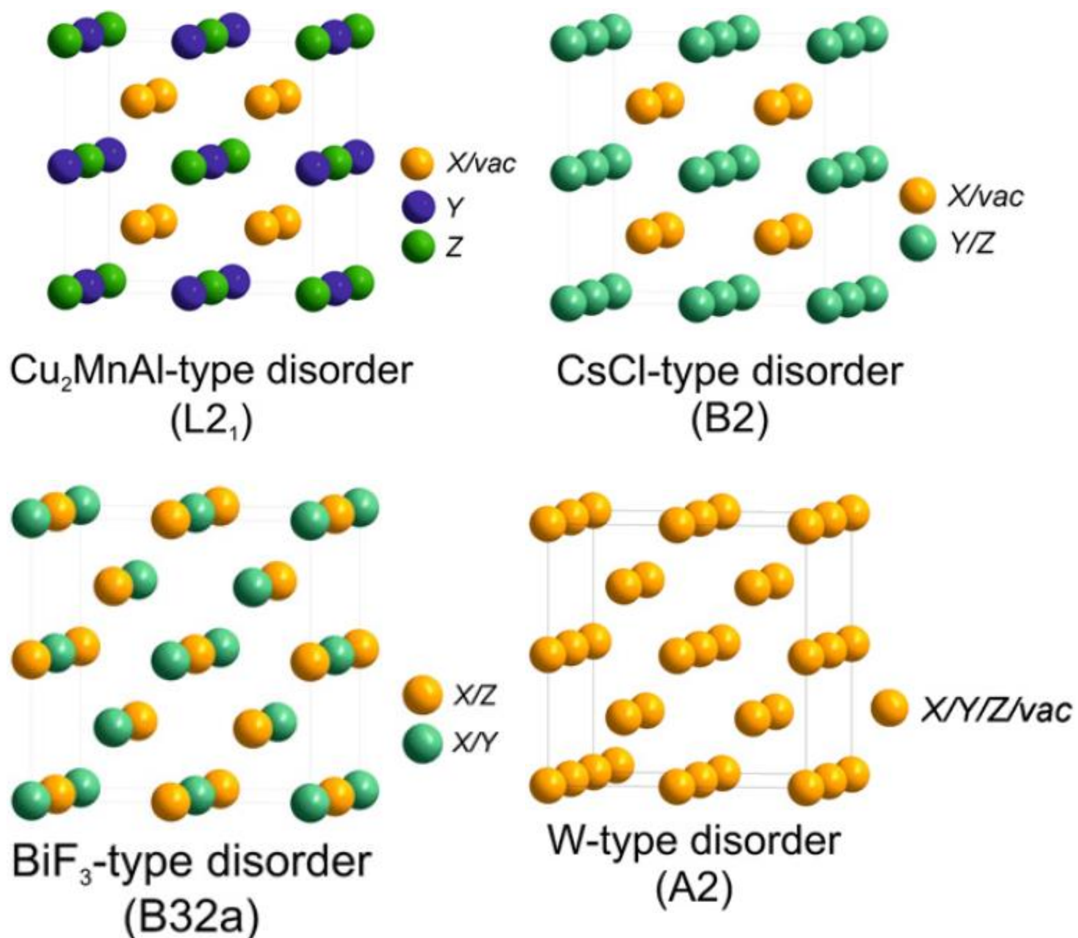

Figure 2.3: Overview of the most common type of ordered and disordered Heusler structures [32].

The Heusler alloy structure has cubic symmetry which may limit the usage of the material when high magnetocrystalline anisotropy is required, i.e. in exchange bias configurations requiring thermal stability of the AF configuration. A tetragonal distortion was reported for the Mn_2YZ Heusler alloy structure and originates from a

stretching of the c axis in which two Mn atoms are allowed in two local symmetries i.e. cubic and tetragonal for example in Mn_2NiSn [35].

The easiest and most available macroscopic method of determining the certain degree of disorder in Heusler structure is X-ray diffraction (XRD). Theoretical XRD patterns have been simulated for Co_2MnSi having different states of atomic disorder [36]. The Highly ordered $L2_1$ and inverse Heusler structures are predicted to show characteristic (220), (200) and (111) superlattice reflections while the semi disordered $B2$ phase is expected to show no (111) superlattice reflection. For the completely disordered $A2$ phase, only the (220) family of reflections is expected.

2.2 Electronic Structure and Band Gap in Heusler Alloys

Heusler alloys have interesting transport properties such as almost 100% spin polarisation which attracted substantial research interest in the spintronics community. A large amount of work has been put into determining the origin of the band gap in half- and full- Heusler alloys as part of understanding their electronic and magnetic properties. It is claimed that for Heusler alloys, the total spin magnetic moment is related to the number of valence electrons. This can help the development of novel materials with bespoke magnetic properties such as half-metallic ferro and antiferromagnets but also magnetic and spin-gapless semiconductors [32]. Full-Heusler alloy structures were studied as candidates to exhibit AF ordering.

Co and Mn based full-Heusler alloys attracted the most attention due to their stable ferromagnetic ordering and high Curie temperatures (over 600 K). most alloys exhibit highly ordered crystalline phases [37]. The alloys crystallise in the $L2_1$ phase shown in Figure 2.3 a) where the Co (X element) atoms occupy two different sublattices and have equivalent atomic surroundings. As the Co atoms are sitting on the second nearest neighbour position, their interaction is important in determining the magnetic properties of the compounds. Figure 2.4 shows the calculated spin resolved density of states (DOS) plots for a number of Co based Heusler alloys.

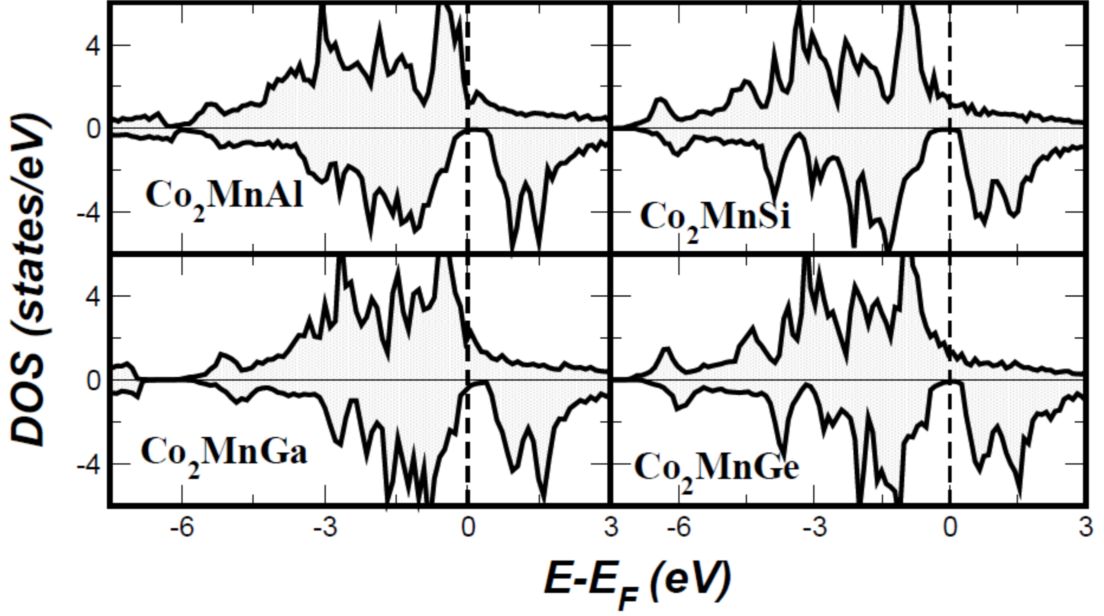

Figure 2.4: Total DOS for Co_2MnZ compounds where Z = Al, Si, Ge, Sn [38].

In the case of Co_2MnSn, both the calculations and photoemission experiments conducted by Brown *et al.* [39] have shown that the valence band stretches around 6 eV below the Fermi level and the up-spin density of states shows a large peak immediately below the Fermi level for this compound.

The origin of the half metallic properties in full-Heusler alloys was described by Galanakis *et al.* [38] for the Co_2MnGe compound. The Heusler alloy lattice is treated initially as that of the Co atoms which form a simple cubic structure while the Mn and Ge atoms fill the body centred sites having the 8 Co atoms as nearest neighbours. The Co atoms are now second nearest neighbours but the hybridisation between the energy levels. Figure 2.5a) shows a schematic representation of the hybridisation of the Co atoms where the 5 *d*-orbitals are divided into twofold degenerate d_r^{2} , d_x^{2} - d_y^{2} and the threefold degenerate d_{xy}, d_{yz}, d_{zx} states. The e_g orbitals (t_{2g} orbitals) can only couple with the e_g orbitals (t_{2g} orbitals) of the other Co atom forming bonding hybrids denoted by e_g (or t_{2g}) and antibonding orbitals denoted by e_u (or t_{1u}) where t_{1u}, t_{2g}, e_g and e_u are the chemical nomenclature describing the shape (angular momentum) of the hybrid orbitals. The coefficients in front of the orbitals show the degeneracy.

The calculation follows with the hybridisation of the Co-Co orbitals with the Mn *d*-orbitals. As shown in Figure 2.5b), the double degenerated e_g orbitals hybridize with the d_r^2 and d_x^2- d_y^2 of the Mn that transform also with the same representation. A doubly degenerate bonding e_g state is created that is very low in energy and an unoccupied antibonding one above the Fermi level. The three t_{2g} Co orbitals couple to the d_{xy}, d_{yz}, d_{zx} of the Mn resulting in 6 new orbitals, 3 of which are bonding and are occupied and the other three are high energy antibonding orbitals. Finally the two e_u and three t_{1u} Co orbitals cannot couple with any of the Mn *d*-orbitals since none of these is transforming with the *u* representations and they are orthogonal to the Co e_u and t_{1u} states.

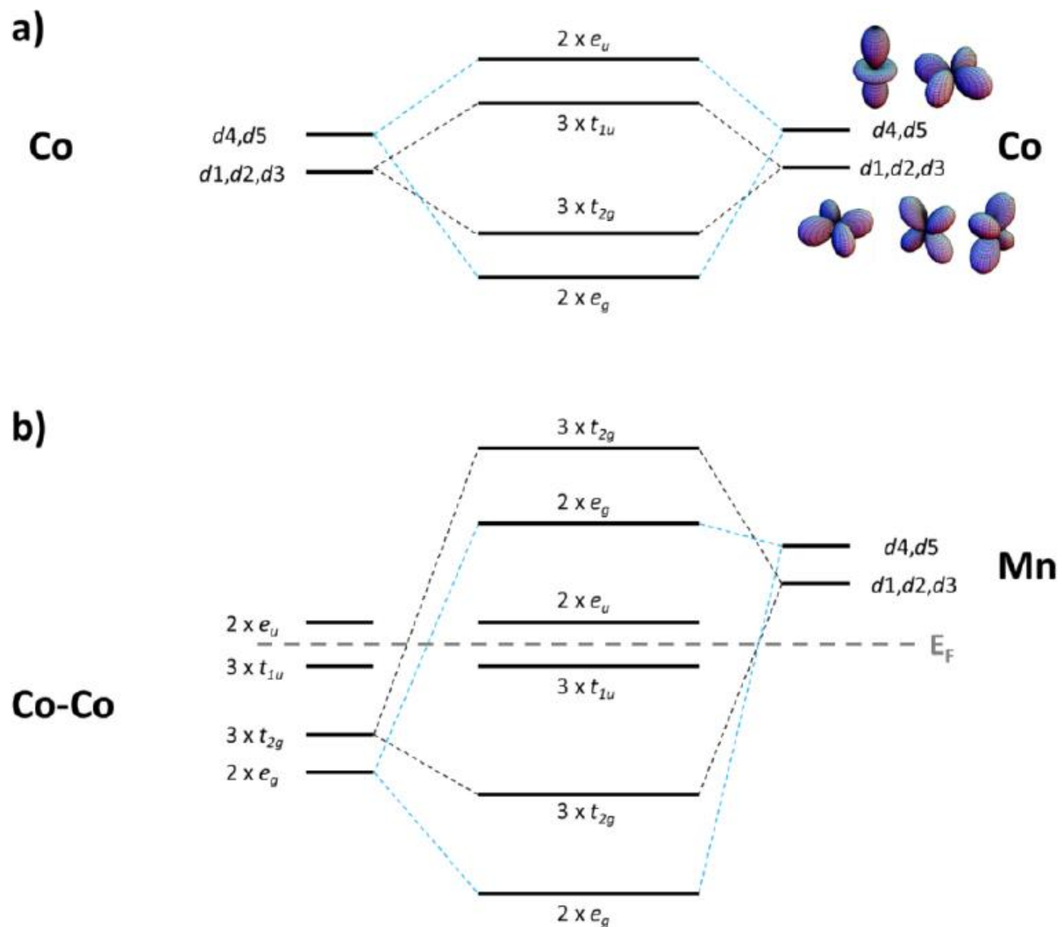

Figure 2.5: Hybridisation between *d* orbitals for minority states for Co_2MnGe considering a) the Co-Co interaction and b) the Mn-(Co-Co) interaction. The shape of the different *d* orbitals are shown in a) [40].

With respect to the Mn and the *sp*-atoms these states are therefore non-bonding. The t_{1u} states are below the Fermi level and they are occupied while the e_u states are just above the Fermi level. Thus in total 8 minority d-bands are filled and 7 are empty. Therefore all 5 Co-Mn bonding bands are occupied and all 5 Co-Mn antibonding bands are empty, and the Fermi level falls in between the 5 non-bonding Co bands, such that the three t_{1u} bands are occupied and the two e_u bands are empty. The calculated maximum moment of the full-Heusler alloys is therefore 7 μ_B per unit cell, which is achieved, if all majority d-states are occupied. Measured values are closer to 5 μ_B per unit cell at room temperature as shown in Chapter 2.4. This creates a band gap for the minority spins at the Fermi level.

2.3 Generalised Slater-Pauling Rule for Heusler Alloys

Slater and Pauling [41] [42] studied the origin of ferromagnetism in transition metals considering the band structure of the elements. They have concluded that the magnetic moment m of $3d$ elements and binary alloys of these elements can be estimated taking into account the average number of valence electrons, N_{Vat} of the individual atoms. The Slater-Pauling relationship for Heusler alloys shown in Figure 2.6 includes the section of low valence electron concentration where $N_{Vat} \leq 8$ which corresponds to localised magnetism found in bcc and variations of this cubic structure. The high valence electron concentration area where $N_{Vat} \geq 8$ is associated with itinerant magnetism and close packed structure such as fcc and hcp [43]. Iron is situated at the borderline between the localised in itinerant states. Heusler compounds are situated in the localised part of the curve. Although the $L2_1$ structure is comprised of 4 fcc lattices, the result is in effect a supercell made up of 8 bcc CsCl-type unit cells. In this region of the curve, the generalised Slater-Pauling rule can be approximated to [44].

$$m \approx N_{Vat} - 6 \tag{2.1}$$

For half-metallic ferromagnets the band gap for the minority states requires that the number of filled minority states be an integer. For the rule described above, the number of minority states may be non-integer if the value of the average number of valence electrons is not an integer value.

In the case of full-Heusler structures (X_2YZ), the mechanism can be extrapolated to the number of valence electrons per unit cell where

$$m_{uc} \approx N_V - 24 \tag{2.2}$$

The magnetic moment of half-metallic Heusler compounds shows a linear dependence with the number of valence electrons per unit cell (N_V) according to Equation 2.2 as shown in Figure 2.6. A few compounds with less than 24 valence electrons, e.g. Mn_2VAl, are known to be half-metallic ferromagnets, in this case with 22 valence electrons [45]. Replacing Co for half on the Mn atoms on the X position, supresses the total magnetic moment for $(Co_{0.5}Mn_{0.5})_2VAl$ with $N_V = 24$ [20]. This shows, that the Slater-Pauling rule is also valid for quaternary Heusler compounds. Moreover, the Curie temperature (T_C) of Co based Heusler compounds shows a linear increase with the total magnetic moment [29]. T_C also follows a linear trend, when plotted against the number of valence electrons, as shown in Figure 2.6. The linear dependence does not apply for materials with $N_V = 27$. Theoretical calculations prove that the magnetic moments on the X (Co) and on the Y sites increase simultaneously with N_V which leads to a non-linear correlation with the total magnetic moment [32]. It should be noted that the decrease of the magnetisation with temperature is very slow. For Co_2MnSi a reduction of less than 1% is observed when increasing the temperature from 5 K to room temperature. Co_2FeSi is the Heusler alloys with the highest magnetic moment of 5.97 μ_B at 5 K and the highest Curie temperature of 1100 K [46].

Besides the generalised Slater–Pauling rule, another rule, as proposed by Kübler *et al.* [47], states that the properties of Mn on the Y position in the Heusler alloys (HAs) must be included. Kübler shows that Mn on the Y position in Heusler alloys tends to have a high, localized magnetic moment. According to electronic structure calculations, in the half Heusler alloys, Mn on the Y position has a magnetic moment of approximately 4 μ_B. Mn may be formally described as Mn^{3+}, with a d^4 configuration. In accordance with the itinerant character of the 3*d* transition metals, one will find a lower magnetic moment, even if there is a partial localization of the *d* electrons.

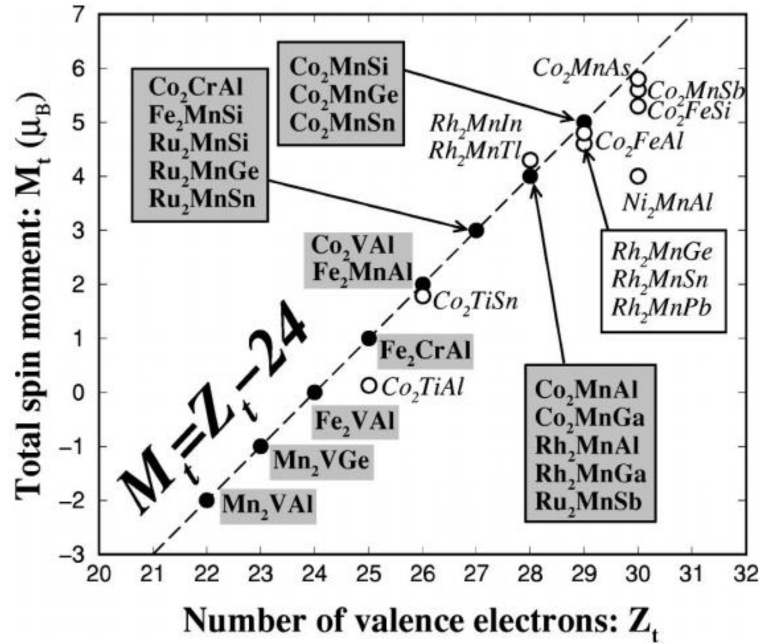

Figure 2.6: Generalised Slater-Pauling rule for full Heusler alloys [38].

A combination of the generalised Slater–Pauling rule and the Kübler rule as discussed previously leads to a rule for the prediction of half-metallic fully compensated-ferrimagnetism in HAs with 24 valence electrons and with Mn on the Y position. In these alloys, the two atoms on the X site have to compensate the magnetic moment of the Mn on the Y site. This rule is in agreement with the approach of de Groot in [48] where the abovementioned rule was implicitly applied in the case of MnCrSb, resulting in the prediction of the completely compensated magnetic moments in MnCrSb.

As shown in Figure 2.6, the non-magnetic character of full Heusler alloys should be easy to determine although exceptions to this rule are discussed in the next section referring to Fe_2VAl and Ru_2MnGe. A completely different challenge is determining whether the ground state of the materials is one of compensated ferrimagnetism or antiferromagnetism.

2.4 Antiferromagnetic Heusler Alloys

Antiferromagnetic materials have become an interesting research topic fairly recently when they were implemented in spin valve structures after the discovery of giant magnetoresistance (GMR) in 1988 [2]. Recently, pioneering research on antiferromagnetic spintronics has shown a number of advantages in using AF materials for data storage such as insensitivity to external magnetic fields, the lack of short range magnetic interactions and intrinsic high frequency AF dynamics. The magnetically compensated AF materials are expected to replace commonly used ferromagnetic materials for data storage [49]. Prior to the extensive industrial use of antiferromagnets (AFs), the intrinsically antiparallel aligned non-magnetic materials were referred to as interesting and useless as suggested by Louis Néel in 1970 [49, 50]. This perception inspired a general lack of interest in understanding the basic mechanisms and possible use of AFs and even despite the discovery of exchange bias in 1956 [51], AF materials were treated more like a curiosity rather than a necessity. Given this context, one would expect that the interest for studying an obscure class of materials which is the antiferromagnetic Heusler alloys (HAs) was initially very low.

One of the pioneering experimental works showing the crystallisation of the AF Cu_2MnSb belongs to Oxley *et al.* (1962) [52] and shows a brief chemical and crystallographic analysis of the bulk compound. The AF transition is proven by magnetic susceptibility and the Néel temperature is found at 38 K. This early study sets the benchmark for the experimental procedure designed to identify AF phases in Heusler alloys prior to the discovery of exchange bias. Early theoretical work published by Kübler *et al.* [47] presents a detailed screening of magnetic properties as a function of temperature for several X_2MnZ full HAs where the calculation of the energy difference between the ferromagnetic (F) and antiferromagnetic (AF) ground states show a favourable AF configuration for Pd_2MnIn at less than 60 K and an associated band gap at the Fermi level.

Kanomata *et al.* reports a study on bulk properties of Ru_2MnZ full Heusler alloys where the Z element is chosen as Si, Ge, Sn and Sb [53]. The crystallographic analysis of the resulting Heusler unit cells shows the ability to easily tune the lattice constant of the materials via atomic substitution as seen in Table 2.1 where R_{nn} is the

nearest neighbour Mn-Mn distance. Temperature dependent magnetisation measurements show values of the paramagnetic transition temperatures for Ru_2MnSn at ~ 300 K and for Ru_2MnSb at 197 K. The changes to the magnetic stability of the structures are attributed to indirect exchange mechanism between moment carrying Mn atoms caused by lattice distortions.

Table 2.1: Lattice parameters and crystal structure of Ru_2MnZ compounds [53].

Compound	a (Å)	R_{nn} (Å)	Crystal structure
Ru_2MnSi	5.8873	4.1629	Ru–Si disorder
Ru_2MnGe	5.9848	4.2319	ordered $L2_1$
Ru_2MnSn	6.2167	4.3959	ordered $L2_1$
Ru_2MnSb	6.2009	4.3847	ordered $L2_1$

The occurrence of itinerant antiferromagnetism in Heusler alloys was discussed by Neumann *et al.* as part of an early study concerning magnetic transitions observed in bulk Pd_2TiIn [54]. Susceptibility measurements show a value for the Néel temperature of 110 K but more importantly, a total magnetic moment of 4.9 μ_B/ formula unit when none of the constituent elements has a large spontaneous moment. The value of the high induced magnetic moment is similar to Pd_2MnIn where the moment is confined to the Mn atom in a collinear AF type-2 structure where the moments are aligned parallel in the (111) plane with antiparallel alignment between the planes. The explanation proposed for the large induced moment for the Ti based Heusler alloy is based on the presence of spin fluctuations characteristic of weak itinerant ferromagnets [55].

Although the early studies showed the existence of AF stable phases in full-Heusler alloys and gave a correlation between structural and magnetic properties in an attempt to highlight the origins of the AF coupling, the experiments were not focused on practical applications and parameters such as pinning strength or temperature dependence of exchange bias. Moreover, the materials were prepared in bulk form. The experiments on AF Heusler alloy thin films became popular at the beginning of the 21st century.

A particularly interesting report which represents the motivation for part of this work was published by Dong *et al.* and presents a study on antiferromagnetic epitaxial

Ni_2MnAl thin films [21]. The highly ordered Heusler alloy was deposited by molecular beam epitaxy (MBE) on GaAs (001) single crystal substrates using a thin seed layer of $Sc_{0.3}Er_{0.7}As$ in order to improve lattice matched growth of the HA. The authors showed that the degree of ordering in the Heusler structure can be altered by changing the deposition temperature from 180°C for the partially disordered *B*2 structure and 400°C for the completely ordered $L2_1$ phase. The stable AF phase of partially disordered Ni_2MnAl was confirmed by an exchange bias measurement when adding a ferromagnetic Heusler layer in contact to the AF as seen in Figure 2.7. It is shown that the critical parameter is the growth temperature, T_g which changes the degree of ordering in the Heusler alloy structure.

The magnetisation loops show the phase transformation as a function of growth temperature for Ni_2MnAl and a modest loop shift of 35 Oe when the bilayer sample is field cooled to 10 K.

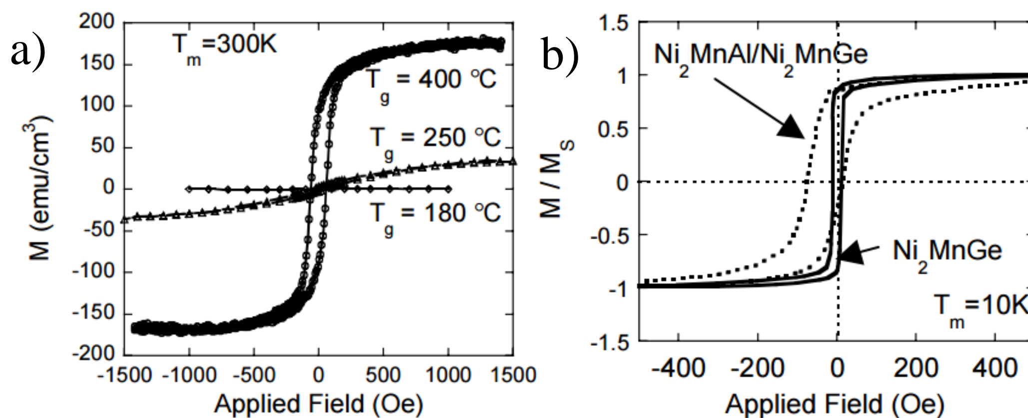

Figure 2.7: a) Magnetisation loops for Ni_2MnAl deposited at increasing substrate temperatures and b) exchange bias of Heusler alloy bilayer system [21].

The layer structure used for the exchange bias measurements is 64 nm Ni_2MnAl/ 12 nm Ni_2MnGe. Data regarding thermal stability of the AF Heusler alloys is not reported and makes the object of this work.

Another material which was assessed in this study is Fe_2VAl. For this particular alloy several inconsistencies are observed in the measurements and predictions of the transport and magnetic properties. Nishino *et al.* [26] performed temperature dependent resistivity and photoemission spectroscopy measurements and associated the results with the response of a non-magnetic narrow gap semiconductor for

Fe_2VAl and heavy-fermionic behaviour with weak magnetic ordering observed at temperatures as low as 2 K for off stoichiometric compositions. Popiel *et al.* [56] showed that the magnetic properties of Fe_2VAl depend on the crystal structure whereupon *A*2 structures are ferromagnetic but the *B*2 structure is superparamagnetic down to 4.2 K. Venkatesh *et al.* [57] have supported this by performing *ab initio* calculations of $L2_1$ ordered Fe_2VAl where several types of disorder were considered for the unit cell. The calculations were then compared to magnetic measurements of DO_3-type Fe_2VAl which provided further evidence for the magnetic properties being dependent on the atomic disorder in the lattice sites but the results point towards paramagnetic and weak magnetic ground states. Singh and Mazin [58] have predicted a metastable antiferromagnetic state of Fe_2VAl when the compound is iron rich to become $Fe_{2.5}V_{0.5}Al$. Their calculations considered a supercell that was created by quadrupling the $L2_1$ structure along the (111) axis. The nearest neighbours of each atom were consistent with the *B*2 disorder allowing for Fe and V atoms to be easily interchanged. The antiferromagnetic ground state was found by tuning the composition of $Fe_{2+x}V_{1-x}Al$ and iterating the calculations with a pre-defined antiferromagnetic ordering. A metastable state was found when the Fe sites had an alternating moment of $\pm 2.3\ \mu_B$ or $\pm 0.6\ \mu_B$ whilst being antiferromagnetically coupled to each other. The results suggested that the Iron with the larger moment was acting as a quasi-free ion which means that its spin arrangement was independent of the lower moment Iron atoms. A speculation of AF phases existing in Fe_2VAl was discussed by Feng *et al.* [59] as a result of a lower than expected superparamagnetic response observed from a sample. There is no clear evidence that Fe_2VAl would have a stable AF phase. It is expected however that combinations of antiferromagnetic and ferromagnetic phases might form in polycrystalline samples as previously reported for Ni_2MnAl [60].

A very close relative of Fe_2VAl, Fe_2VSi was reported to have a stable antiferromagnetic tetragonal ground state at low temperatures [61-63]. Fukatani *et al.* used this material in thin film form deposited on MgO and $MgAl_2O_4$ to prove the effects of biaxial strain on the magnetic and transport properties of the Heusler alloy [64]. The results show an increase of more than 50% of the Néel temperature with a maximum value of 193 K as determined by temperature dependent resistivity measurements.

The Ru_2MnZ Heusler alloys were studied in detail as they showed the potential to form stable AF phases. Moreover, the early experimental work by Kanomata [53] proved that this composition has the tendency to order antiferromagnetically for a number of Z elements in bulk materials. Among these compositions, Ru_2MnGe makes the object of this study.

Ru_2MnGe was studied by Ishida *et al.* [65] in a theoretical report which calculated the spin configuration for three types of AF ordering in the fully ordered $L2_1$ phase, one of which was determined experimentally via neutron scattering by Gotoh *et al.* [66]. The AF type 2 structure was attributed to the antiparallel alignment of the Mn atomic moments along the (111) direction with a magnitude of ~ 3.8 μ_B and a distance between neighbouring Mn atoms of about 0.4 nm. The results were explained using the localised 3*d* atomic moment of Mn and indirect exchange mechanism mediated by conduction electrons. More importantly, the Néel temperature for Ru_2MnGe was found at 295 K.

Fukatani *et al.* reported a study on epitaxially deposited thin film of Ru_2MnGe where the Néel temperature of the AF Heusler alloy is controlled via inducing in plane compressive strain from the lattice mismatch of ~1% with the single crystal MgO (001) substrate. An increase of 37 K of the transition temperature is observed when compared to the value registered for the bulk compound which brings T_N to 353 K measured by temperature dependent resistivity. The stability of the partially disordered (*B*2) AF phase is confirmed with a low temperature exchange bias measurement. A 5 nm thick Fe_2CrSi ferromagnetic Heusler alloy is used to prove the pinning strength of Ru_2MnGe. The bilayer structure shows a modest exchange bias field H_{ex} of almost 50 Oe at 77 K. A more detailed study of the AF stability and magnetisation reversal mechanism of Ru_2MnGe is given in Chapter 8.

3 Magnetoresistance and Spintronic Devices

With the discovery of giant magnetoresistance (GMR), spin electronics raised an intense commercial and research interest. Magnetoresistive sensors can be found in the read head of every hard disk drive on the market are also used for any other application where a precise determination of a magnetic state is required. Spintronics continues to spread towards applications such as magnetic random access memory (MRAM) which is designed to replace the current transistor based technology. The progress in manipulating spin rather than electron charge would offer a stable logic state when the device is powered off however the materials needed for implementing such processes require a new set of properties. Typical transition metal ferromagnets are not suitable for spin manipulation due to inferior spin polarisation capability hence low spin injection efficiency, usually less than 50%. Half-metallic Heusler compounds and alloys are a leading candidate to replace current materials and offer much greater spin polarisation which was predicted to be up to 100%. Heusler alloys offer a broad range of materials with tuneable transport and magnetic properties for the emerging data storage technology.

3.1 Magnetoresistance

The concept of magnetoresistance originates from early experiments conducted in 1856 by Thomson [67] where the interaction between the electrical current and magnetisation of the conductor was observed. Ordinary magnetoresistance is known to be present in both magnetic and non-magnetic materials due to the Hall effect.

In the case of ferromagnetic materials, the magnetoresistance is affected by the intrinsic anisotropy of the material and therefore the anisotropic magnetoresistance (AMR) is observed. This process is dependent on the direction of the applied magnetic field and it is explained by spin orbit coupling within the ferromagnetic material [68]. In AMR, the electron spin-orbit coupling gives rise to a difference in the scattering cross section when the charge current is parallel or perpendicular to the atomic magnetic moments which are oriented by an applied magnetic field [69]. The effect is significant but the magnitude of the change in resistance is only a few percent which does not offer accuracy in differentiating between two possible states of magnetisation.

3.1.1 Giant Magnetoresistance (GMR)

In 2007, Grünberg and Fert were awarded the Nobel Prize for the discovery of the giant magnetoresistance effect (GMR) which is based on spin-dependent scattering and initially investigated for bulk ferromagnetic materials in the first half of the 20th century [70, 71]. The phenomenon was theoretically described firstly by Mott in 1936 [72] using the two current model which stated that the current flowing through a transition metal can be separated into two spin channels. The pioneering work allowed for detailed research on spin dependent scattering to be conducted by Fert and Campbell in the second half of the 20th century which resulted in good agreement with the available experimental data [73, 74].

A GMR structure is purposely engineered to exploit the spin-dependent scattering and can be explained using a simple resistor diagram seen in Figure 3.1. Considering the two current model or independent spin up and spin down electron transport channels, the ferromagnetic layers act as resistors in a parallel configuration for the spin channel paths. The representation includes both the minority and majority carriers but the effect will be dominated by the majority spins. It is then clear that the only mechanism that can be used to differentiate between the low resistance state and the high resistance state of the GMR stack is to switch the magnetisation of the two magnetic layers between parallel, R_P (low resistance) to antiparallel R_{AP} (high resistance) state as seen in Equation 3.1 [75]:

$$\frac{\Delta R}{R} = \frac{R_{AP} - R_P}{R_P} = \frac{(R\downarrow - R\uparrow)^2}{4R\downarrow R\uparrow} \tag{3.1}$$

Despite the apparent simplicity of the GMR mechanism, a detailed analysis of electron scattering dynamics reveals some limitations of the magnetoresistance effect. Statistically, the electron scattering process can be elastic or inelastic and may or may not result in momentum change or spin flipping [76]. Scattering processes also occur at the interfaces and in the bulk of materials. This implies that the electrons must remain coherent in their orientation before experiencing any spin-dependent scattering. Considering the potential travel path of a spin polarised electron, this distance needs to be shorter than the mean free path of the electron

itself (usually tens of nanometres) [75]. The difference in electron path lengths is best shown by the two main geometries of GMR sensors as seen in Figure 3.2.

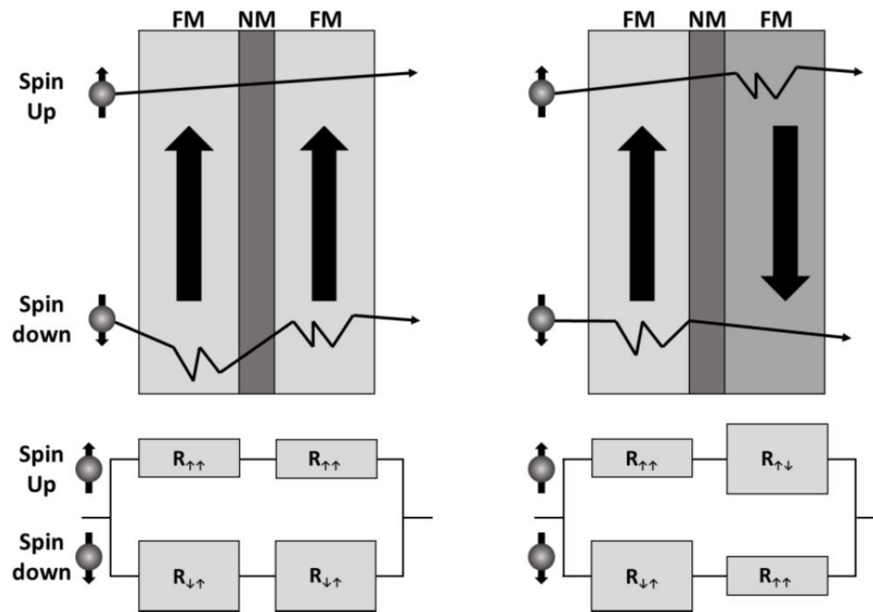

Figure 3.1: Schematic diagram of the GMR effect and spin-dependent scattering using a resistor network model [75].

Although the transition from parallel to antiparallel magnetisation of the two ferromagnetic layers is the only requirement for a GMR sensor to work efficiently, applying a large enough magnetic field may cause the structure to switch to the parallel configuration by overcoming the exchange interaction between the magnetic layers. The obvious solution was the introduction of a pinning mechanism which would keep the magnetisation direction of one of the layers constant while allowing switching of the second layer in the presence of an external field.

The resulting multilayer structure was developed by researchers in the IBM laboratories and is called a spin valve [77-80]. Spin valves consist of a classic GMR configuration with the addition of an antiferromagnetic thin film designed to pin a neighbouring ferromagnetic layer via exchange bias while allowing the rotation of the remaining (free) magnetic layer when an external field is applied.

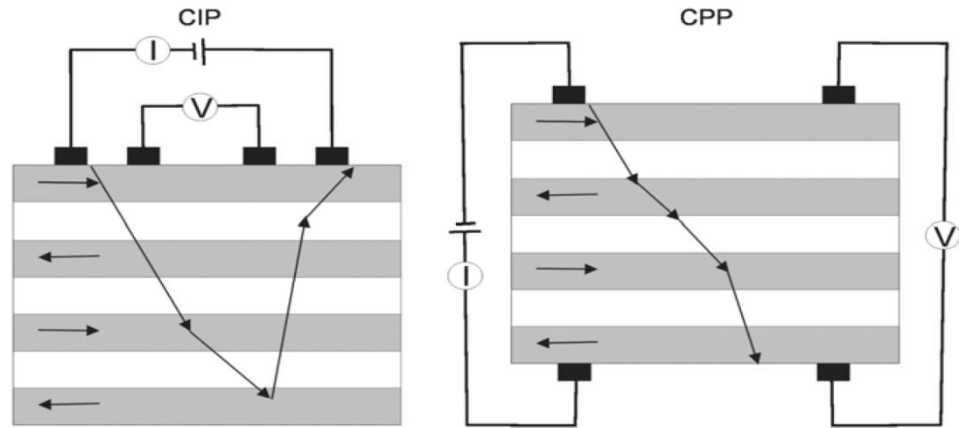

Figure 3.2: Schematic diagram of "current in the plane" (CIP) and "current perpendicular to the plane" (CPP) GMR geometries [40].

A soft ferromagnetic material is chosen as the free layer which can be switched easily in a small detected field. The easy axis of the magnetisation of the free layer can lie parallel or perpendicular to the magnetisation of the reference layer. The change in resistance is then proportional to the dot product of the two magnetisation vectors. This makes the change in resistance, $\Delta R/R$ proportional to the cosine of the angle between the two magnetisation vectors. For a linear response of the magnetic sensor, a 90° offset in the magnetisation vector directions is sought. A recent example of a spin valve structure using a ferromagnetic Heusler alloy is shown in Figure 3.3. Another possibility of pinning a magnetic layer consists in engineering a series of soft and hard magnetic layers spaced out in such a way that any two layers have antiparallel coupling therefore creating what is known as a synthetic antiferromagnet (SAF) [81].

The spin valve structure relies on the strong pinning of the fixed ferromagnetic layer via exchange bias so therefore pioneering research on antiferromagnetic (AF) materials was conducted. Initial GMR structures could utilise antiferromagnets such as, NiO and CoO which had low anisotropy and poor thermal stability. Improvements were noted for AF alloys such as IrMn and PtMn [82] for increasing the anisotropy (~10^7 erg/cm^3) and therefore the thermal stability of the alloys. The demand for strong, stable and reliable magnetic pinning fuelled research in the field of exchange bias [83].

Increasing the complexity of the GMR spin valve structures and the number of magnetic and spacing layers can cause a series of spin scattering events which may decrease the efficiency of the sensing structure. The reduction of the electron mean free path limits the spin diffusion length. The spin independent scattering may arise from nanocrystalline defects such as vacancies, grain boundaries and roughness and interlayer mixing at the interfaces. The quality of the multilayer structures can be improved by utilising advanced deposition techniques and annealing in order to promote crystallisation quality of the thin film components.

An ongoing research effort is made in order to develop superior ferromagnetic compounds with increased spin-dependent scattering. One of the candidate group of materials are the half-metallic Heusler compounds which have the majority spin

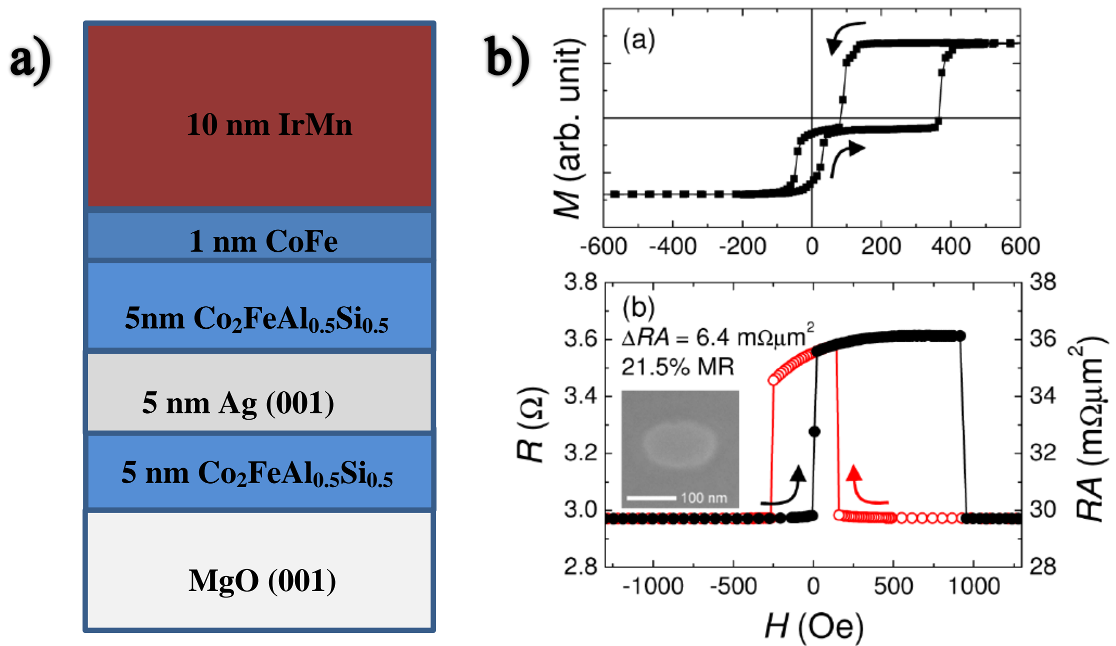

Figure 3.3: a) Schematic representation and b) magnetisation and transport measurements for a top-pin type exchange bias spin valve using the $Co_2FeAl_{0.5}Si_{0.5}$ Heusler alloy [84].

band shifted below the Fermi level resulting in a theoretical 100% spin polarisation as discussed in Chapter 2. Figure 3.3 shows an example of a spin valve structure which uses Heusler alloys.

3.1.2 Applications of GMR

The discovery of GMR allowed for notable progress in the data storage industry and offered a new perspective for electronic devices which could in theory transport spin rather than the electron charge. The efficiency in detection of magnetic fields meant that in less than ten years from the discovery of the effect, hard disk drives (HDDs) received GMR based read heads. Due to the increased efficiency of the magnetoresistance sensor, the data bit size could be decreased and therefore the areal density of storage increased exponentially.

(HDDs) store the information on a magnetic medium which is coated onto a disk. One or several of the rotating disks make the hard drive. The disks are coated with a series of thin films, one of which is the recording medium itself. A granular Co based alloy (CoCrPt) is deposited in such a way that the individual grains are separated by a non-magnetic compound such as Cr or SiO_2 and exchange decoupled in order to preserve the different orientation of the magnetisation of neighbouring regions or bits of information. The binary information is read as 1 or 0 according to the presence or absence of a magnetic transition at certain intervals. Once the information is written by the write head, it can be re-written by switching the magnetisation of the information bits. A comprehensive review of the magnetic recording technology can be found at [85]. Figure 3.4 shows a schematic diagram of the read-write head in a perpendicular recording media configuration.

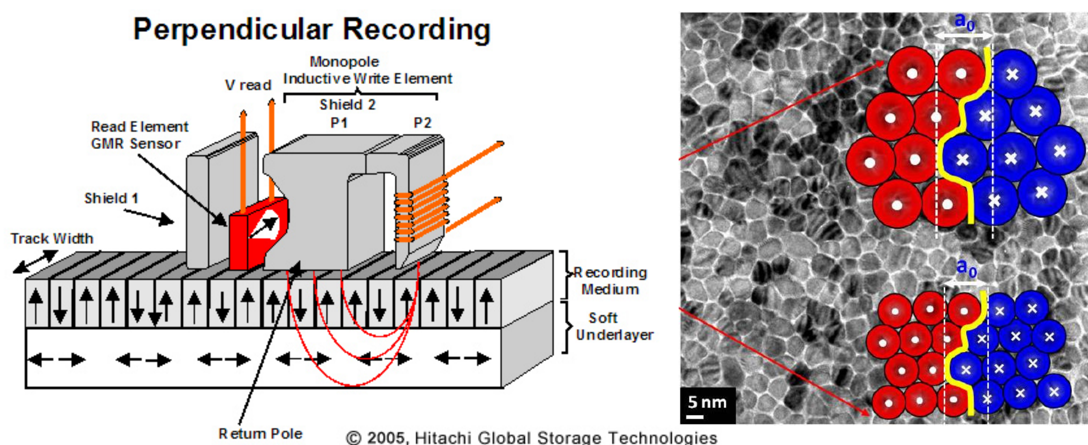

Figure 3.4: Schematic diagram of the read-write system in HDD and the bit transition with in granular recording media [86] [87].

The current perpendicular to plane (CPP) configuration of GMR sensors emerged as the need for downsizing the lateral size of storage bits required a similar size sensor dimension. The current in plane (CIP) GMR heads reached their limitation mainly due to edge degradation effects induced by the device manufacturing process coupled with increased shunting probability caused by the decreased sensor length.

3.2 Current Induced Magnetisation Switching

Theoretical studies conducted by Berger and Slonczewski [88, 89] showed that a spin polarised current is able to induce spin transfer torque which could switch the magnetisation direction in a ferromagnetic layer without the need of an external magnetic field. The effect was proven experimentally by Katine [90]. In metallic ferromagnetic materials, the 4*s* conduction electrons are exchange coupled to the 3*d* magnetism inducing electrons which undergo excitation in the form of spin waves or magnons as shown in Figure 3.5. The phenomenon is similar to the quantised crystal lattice vibrations known as phonons and the photon light quanta. The pioneering work done by Berger also predicted scattering at the material interface. Slonczewski related the current induced torque to the spin polarisation and absorption of the component of the spin which is perpendicular to the magnetisation.

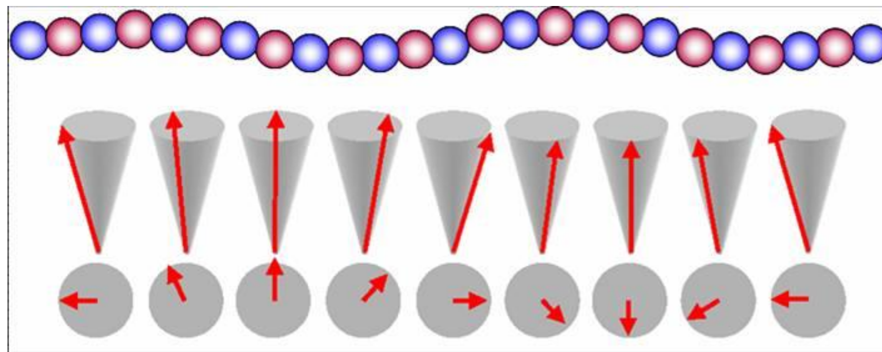

Figure 3.5: Schematic representation of a spin wave or magnon [91].

Experiments on (CPP) magnetoresistive devices showed that the current passed through the device as a probe of the resistance (relative alignment of the magnetisation directions of the ferromagnetic layers) of the GMR structure can switch the magnetisation direction of the layers. As electrons pass through a ferromagnetic layer, they become spin polarised in the direction of the magnetisation

of the F layer. Electrons with antiparallel spin orientation are scattered and do not participate in the conduction mechanism. If, for example the current passes through the pinned ferromagnetic layer, the electrons spins orientate parallel to the magnetisation direction and pass through the non-magnetic spacer layer whilst maintaining their polarisation. As they interact with the free magnetic layer, the transfer of angular momentum can be seen as an effective torque applied on the magnetisation. Given enough current density, the magnetisation of the free layer can be reversed.

Katine [90] reported current driven magnetisation reversal in Co/Cu/Co nanopillars as shown in Figure 3.6. A current density of 10^8 A/cm^2 is required in order to switch the magnetisation in a low magnetic field. Applying a high magnetic field, magnetisation precession is observed. The switching is dependent on the current direction which proves the reversal mechanism is initiated by spin transfer torque rather than magnetic field. For larger applied magnetic fields, a current bias of the proper polarity can excite uniformly precessing spin-wave modes, and in this regime the authors find excellent quantitative agreement between experimental data and the spin-transfer theory, especially with respect to the damping parameter α_d.

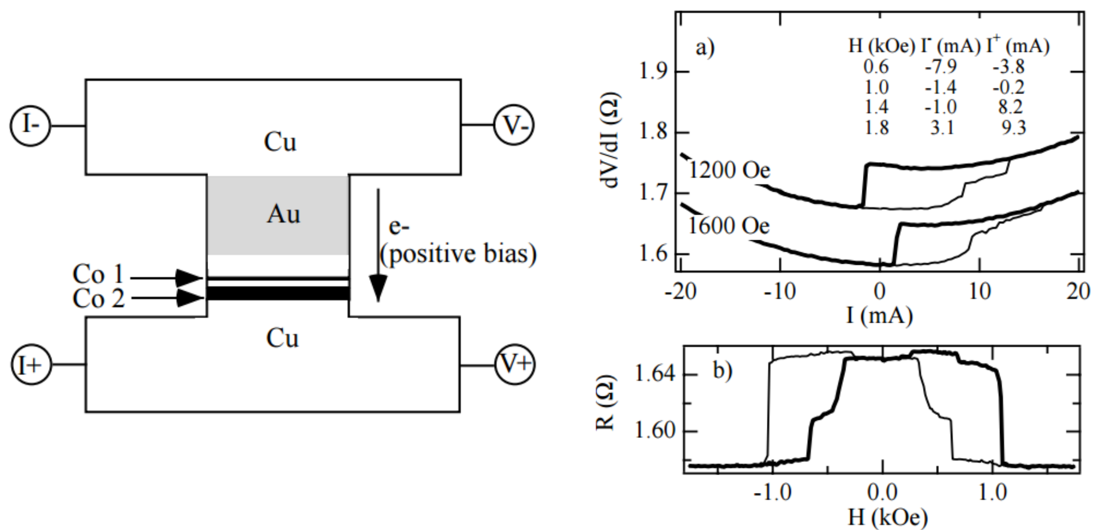

Figure 3.6: Schematic diagram of the device used for current and magnetisation induced switching for Co/Cu/Co GMR structure [90].

Although GMR started the scientific interest in spintronics, magnetic tunnel junctions (MTJ) have taken over GMR devices in HDD read heads and MRAM applications offering higher magnetoresistance, intrinsically high resistance which

makes tunnel junctions compatible with CMOS technology, ease of scaling and stability with temperature. The TMR based devices will be discussed in the following section.

3.3 Tunnelling Magnetoresistance

The tunnelling megnetoresistive (TMR) junctions are very similar to the GMR structures but instead of a conductive non-magnetic interlayer, magnetic tunnel junctions (MTJ) have an insulating oxide layer which separates the two ferromagnetic films. In order to avoid the metallic conduction through the multilayer structure, the CPP configuration is adopted. As the name suggests, the conduction mechanism in TMR structures is based on quantum tunnelling of electrons through the non-conductive barrier.

TMR depends on the conduction states available to tunnel across the insulating oxide barrier, not just the spin-dependent scattering within the electrodes. This is shown schematically in Figures 3.7 and 3.8. For the parallel orientation there are a large number of majority conduction states and majority valance states resulting in a large electron flow and hence low resistance. For the antiparallel orientation there are fewer majority and minority states resulting in a high resistance. This makes TMR dependent upon the number of available states for each spin direction at the Fermi energy or the spin polarisation as seen in Equation 3.2:

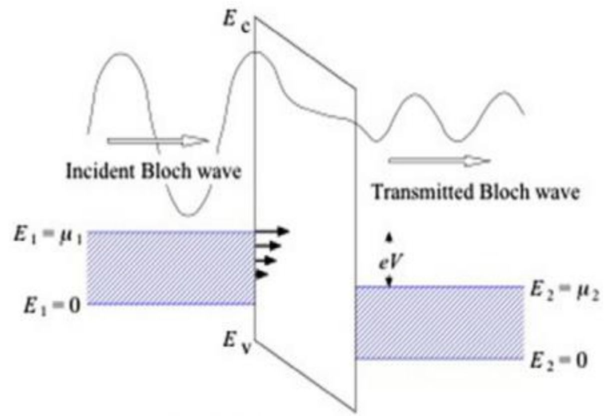

Figure 3.7: Schematic diagram of quantum tunnelling [92].

$$\frac{\Delta R}{R} = \frac{R_{AP} - R_P}{R_P} = \frac{2P_{F1}P_{F2}}{1 - P_{F1}P_{F2}} \tag{3.2}$$

where $P_{F1}$and P_{F2} are the spin polarisations of the two ferromagnetic layers in the junction. The polarisation P_F can be defined as:

$$P_F \equiv \frac{N_{majority} - N_{minority}}{N_{majority} + N_{minority}} \tag{3.3}$$

where $N_{majority}$ and $N_{minority}$ are the number of electrons in the majority and minority spin channels at the Fermi level (E_F) as described by the density of states (DOS) of the ferromagnetic layers. Considering that spin polarised materials such as Heusler compounds are predicted to exhibit 100% spin polarisation, as discussed in Chapter 2 the TMR values are expected to be extremely high.

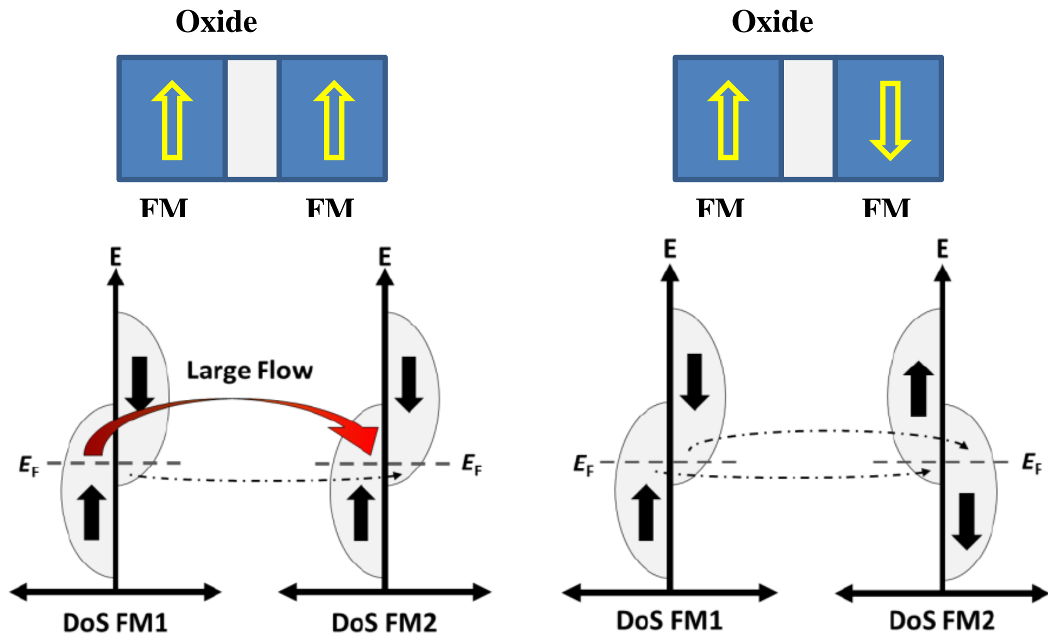

Figure 3.8: Schematic representation of TMR mechanism according to the two current model and DOS of the ferromagnetic layers [40].

The TMR effect was discovered by Julliere in 1975 using a Fe/Ge/Co in plane magnetic tunnel junction (iMTJ) using low temperature electrical measurements [93]. At the end of the 20th century, TMR ratios of more than 10% were reported for IMTJs using an AlO_x barrier measured at room temperature (RT) [94, 95]. The development continued for the Al oxide based MTJs but the theoretical limit of the magnetoresistance ratio of 70% was already achieved [96]. This value was predicted by Julliere's formula [93] in which the TMR ratio depends on the spin polarisation of the ferromagnetic layers.

At the very beginning of the 21st century, theoretical predictions for obtaining a TMR ratio of more than 1000% were made by Bulter *et al.*, Mathon and Umerski [97, 98]. The calculations were made for Fe (001)/MgO (001)/Fe (001) structures where (001) crystalline orientation of the bcc Fe layer is necessary for increased transmittance of spin polarised electrons. The development of the Fe based iMTJ continued and reached TMR values of 88% at RT for epitaxial structures deposited by molecular beam epitaxy (MBE) [99]. TMR ratios between 200 and 300% were reported at RT for systems using CoFe and CoFeB magnetic layers in iMTJs deposited using conventional sputtering technology on Si substrates [100, 101]. Figure 3.9 shows the crystallisation of a magnetic tunnel junction at increasing annealing temperatures. Recently, Ikeda *et al.* demonstrated a TMR ratio of over 600% at RT and over 1000% at low temperatures using pseudo-spin-valves without the pinning antiferromagnetic layer and post annealed at 525°C. These results agree with the theoretical predictions of the effect [102].

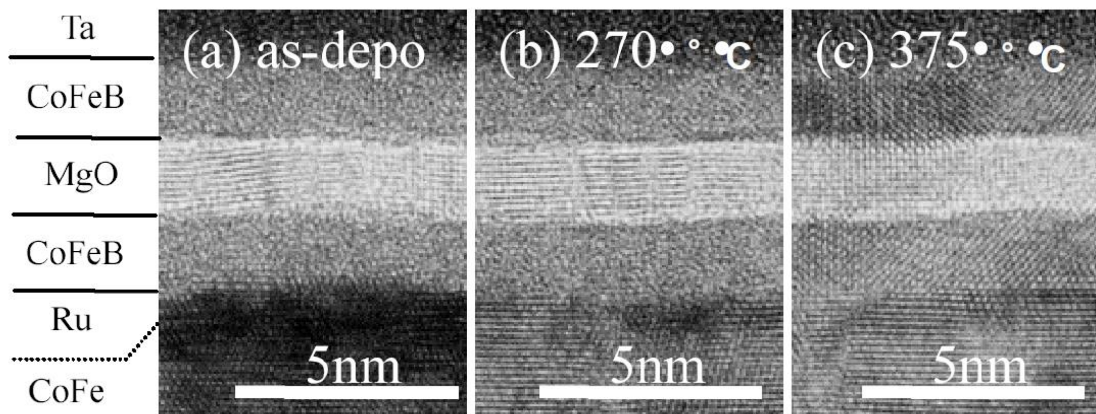

Figure 3.9: Cross sectional TEM images of MTJ crystallising in post annealing experiment [103].

The development of perpendicular magnetic tunnel junctions (pMTJ) faced a few difficulties such as the deposition of highly crystalline bcc CoFeB (001) /MgO (001) /CoFeB (001) with perpendicular anisotropy. Conventional perpendicular anisotropic materials such as CoCrPt and Co/Pt multilayers cannot be used as they have a different crystal structure therefore preventing epitaxial growth throughout the MTJ. TMR ratios of over 90% were reported for pMTJs using $L1_0$ ordered FePt [104], Co/Pt superlattice arrangements [105]. Initial efforts in developing pMTJs were

based on a combination of materials with in plane and perpendicular anisotropy and required complicated deposition procedures. Ikeda *et al.* reported a TMR ratio of 100% for conventional CoFeB/MgO/CoFeB MTJs and showed that a very thin CoFeB layer has perpendicular anisotropy when deposited on MgO (001). This result triggered the mass production of pMTJs for magnetic random access (MRAM) applications [106].

Both GMR and TMR sensors can be used in HDD read heads and MRAM applications, each having advantages and disadvantages. There is a noticeable difference in the resistance area product (*RA*) which is higher for TMR sensors due to the tunnelling effect. The intrinsically high resistance of MTJs can cause noise problems and a high resistor capacitor (RC) time constant reducing the operation bandwidth. On the other hand, the superior TMR ratio increases output voltage signal such that the data reading process is susceptible to less errors. GMR sensors use considerably less energy but due to the decreased MR ratio of about 20%, high current densities are needed in order to achieve a useable signal voltage. This may affect the thermal stability of the device but more importantly, for spin transfer torque applications, large currents can affect the magnetic stability of the devices.

3.4 Magnetic Random Access Memory (MRAM)

The magnetic random access memory (MRAM) is an innovation for computing architecture based on non-volatile RAM which is capable of retaining information when the device is switched off. The technology is currently advancing towards further reduction in power consumption together with conventional low voltage technology [107-109]. The ultimate goal is to develop computing equipment that can be rapidly switched off when not used and instantly resume once the power is reconnected thus contributing to a global effort in decreasing overall energy consumption and creating a sustainable living environment.

Figure 3.10 shows the conventional MRAM cell based on magnetic field writing induced by current passing through a world line (used as a gate operation device for the isolation transistor) (WL) and a bit line (BL). This type of architecture requires a larger current in order to reduce the size of the tunnel junction as the field required for switching increases when scaling down the MTJ. This is a non-viable alternative

as the power consumption increases with the capacity of the chip. [103]. Another device layout is based on the spin transfer torque mechanism described in Section 3.3.

In the case of magnetic tunnel junctions the spin polarised current exerts spin transfer torque on the magnetisation of the free layer and when the current threshold limit is exceeded, the magnetisation direction of the free layer is switched. For the inverse mechanism, after electrons passing through the free layer reach the pinned (fixed) layer, if the spin polarisation is parallel, the spin current will pass through. For the antiparallel configuration, the inversely polarised electrons are reflected back at the pinned layer interface with the tunnel barrier. Above a threshold value, the reflected spin current becomes strong enough and switches the magnetisation of the free layer.

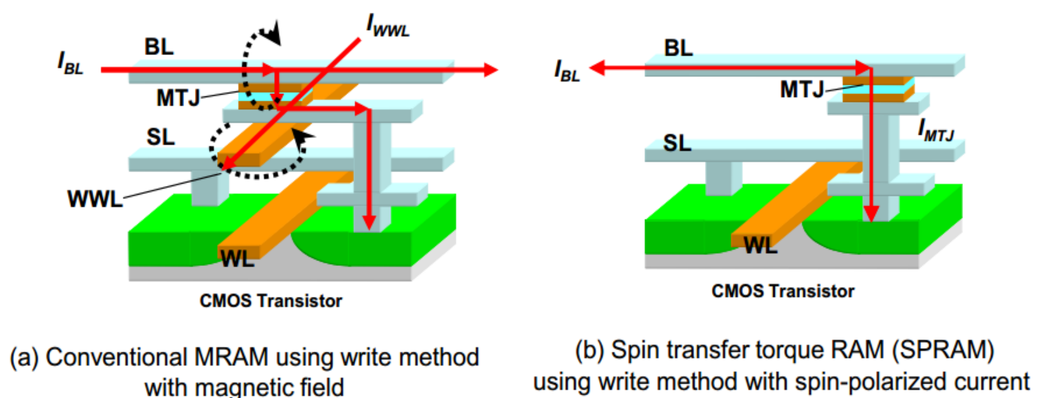

Figure 3.10: Schematic representation of (a) conventional and (b) spin transfer torque MRAM cells [103].

The first MTJ was used for MRAM demonstration in 1996 [110, 111]. In 2016, SK Hynix and Toshiba Corp announced a prototype 4 Gbit STT-MRAM which consists of eight 512-Mbit banks. The cell area is as small as $9F^2$, which is equivalent to that of DRAM (about $8F^2$) where F represents the fabrication rule [8]. The next-generation MRAM and spin-RAM, the current issues need to be addressed: the reduction of the switching field or critical current density and a reduction of the fabrication rule. Based on the scalability of MRAM and spin-RAM bits, STT must be used as explained previously. A synthetic ferromagnet, such as CoFeB/Ru/CoFeB, was implemented as the free layer by AIST [112], resulting in a

five times increase in thermal stability with an 80% increase in the critical current density. This configuration can achieve a 10 Gbit spin-RAM device. The remaining issue to realize a high-density spin-RAM is the reduction of the fabrication rule, which may be achieved by replacing the additional transistor with a possible new device design [92].

Besides the necessity for increased thermal stability, the research community still focuses on increasing the TMR ratio. A value of more than 150% is desirable in order to achieve sub 10 ns read-out. The write current density, J_c lower than $1x10^6$ A/cm^2. The MTJ breakdown voltage should be more than 3 times larger than the write voltage (~0.5V at 10 ns). For STT applications, where strong perpendicular anisotropy is required, the Gilbert damping constant, α_d needs to be as low as possible despite the large intrinsic spin-orbit coupling of materials with high anisotropy such as Pt, Pd and Au [113].

4 Exchange Interactions

Magnetic materials have been used extensively in diverse applications in either bulk or thin film form. The magnetism of thin film structures has become the core mechanism of modern data storage technology. The necessity for more efficient and higher density information storage devices has driven the current research to the state of atomic engineering where novel materials are deposited with a precision of one atomic layer [114]. The resulting effects can only be described and reproduced if the properties of magnetic materials and the associated interaction mechanisms are understood. This chapter gives an overview of the basic theory of magnetism applied in thin films and especially exchange bias systems. The discussion ranges from fundamental concepts such as exchange interactions, continues with an overview of relevant anisotropies and presents effects of the fundamental concepts on the magnetisation reversal process in real systems.

For this work, the c.g.s. unit system was chosen as it is used in the magnetic recording industry. The main source texts used in this chapter are the extended reviews published by O'Handley [115] and Culity and Graham [116] which are key references for the information given unless otherwise stated.

4.1 Direct Exchange

The first major breakthrough in understanding the self-ordering in ferromagnetic (F) materials was made by Weiss at the beginning of the 20th century with the theory of molecular fields:

$$\boldsymbol{H}_m = \gamma_m \boldsymbol{M} \tag{4.1}$$

where $\boldsymbol{H}_m$ is the molecular field vector, $\boldsymbol{M}$ is the magnetisation vector and γ_m is the molecular field coefficient. This equation describes a magnetisation process for which the molecular field aids the applied field in magnetising the substance. This model managed to describe the behaviour of paramagnetic materials (Curie-Weiss law). The theory, despite being incomplete lead to the formulation of two postulates: spontaneous magnetisation and the existence of magnetic domains which were proven afterwards.

The physical origin of the molecular field introduced by Weiss was not understood until Heisenberg attributed the interaction to quantum mechanical exchange forces. The quantum mechanical approach explained the formation of the hydrogen molecule by applying Pauli's exclusion principle for the two atoms. Heisenberg showed that the exchange energy plays an important role in ferromagnetism. For two atoms, i and j, with spin angular momentum $\boldsymbol{S}_i h/2\pi$ and $\boldsymbol{S}_j h/2\pi$ the exchange energy E_{ex} is:

$$E_{ex} = -2J_{ex}\boldsymbol{S}_i\boldsymbol{S}_j = -2J\boldsymbol{S}_i\boldsymbol{S}_j cos\phi_{ij} \tag{4.2}$$

where $\boldsymbol{S}_i$, $\boldsymbol{S}_j$ are the spin angular momentum vectors of two atoms J_{ex} is the exchange integral and ϕ_{ij} is the angle between the spins. For positive J_{ex}, E_{ex} is minimum for parallel spins while for negative J_{ex}, spins lie antiparallel. Equation 4.2 applies only to a pair of atoms so for a more complex multi-atomic system, the exchange integral can be approximated to the sum over all atomic pairs. The nearest neighbour approximation is valid due to the very short range of exchange forces. Even using these approximations, the exchange integral cannot be accurately determined for elements with the atomic number Z > 2 which makes it impossible to predict the magnetic characteristics of materials from first principle calculations.

As the exchange forces were proven to be responsible for magnetic properties, it's possible to predict the occurrence of ferromagnetism in some metals. As shown in Figure 4.1 known as the Bethe-Slater curve, a variation of the exchange integral with the r_a/r_d is postulated. r_a and r_d are the atomic and *d* electron shell radii.

As the atoms in solids are overlapping electron orbitals with each other, bringing two atoms close together without changing the *d* shell radius will result in an initial increase of the positive exchange interaction which favours parallel spin alignment. Further decreasing the interatomic distance causes the exchange integral to decrease to the point where the *d* electrons are so close together that the spins must align antiparallel hence resulting in antiferromagnetic (AF) ordering (J_{ex}< 0). The Bethe-Slater curve cannot explain the magnetism of alloys or compounds which are ferromagnetic despite the non-magnetic nature of the composing elements. The Cu_2MnAl Heusler alloy is an example of a ferromagnet with no magnetic elements.

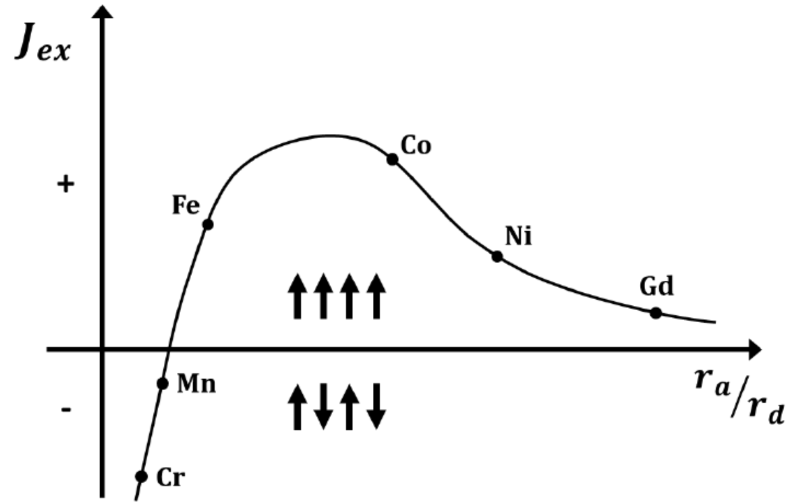

Figure 4.1: Dependence of the exchange integral on the atomic separation normalised to the radius of d orbitals at 0 K [116].

In metallic systems where the electrons form a band structure, the magnetic moment of the material is determined by the energy of aligning spins parallel or antiparallel in bands near the Fermi energy (E_F). Magnetism occurs according to the Stoner criterion:

$$J_{ex}(E_F)n(E_F) > 1 \tag{4.2}$$

where $J_{ex}(E_F)$ and $n(E_F)$ are the exchange integral and the density of states at the Fermi energy.

4.2 Indirect Exchange

Indirect exchange is a consequence of the polarisation of conduction electrons by the unpaired bound electrons. The resulting polarised conduction electrons can exchange their polarisation with the bound electrons in the neighbouring atom. The sign of the coupling is controlled by the separation between the atoms. The indirect exchange interaction can explain long range magnetic ordering that occurs across non-magnetic or frustrated boundaries. Indirect exchange coupling can therefore occur across defects and grain boundaries in polycrystalline thin films and constitutes an important mechanism in intergranular coupling.

Parkin *et al.* [117] shows experimental evidence of the long range magnetic interaction by varying the thickness of a Cr spacer layer between Fe thin films. As seen in Figure 4.2, the coupling between the ferromagnetic (F) layers oscillates periodically from parallel (low saturation field) to antiparallel (high saturation field) when the thickness of the non-magnetic spacer layer is increased.

For parallel alignment of the F layers, empty states are available in the *e.g.* spin up band for both the spacer and F layers. This would allow the up spin electrons to move freely through the stack while the down spin electrons are confined within the spacer layer similarly to a quantum well. For antiparallel alignment, the assumed spin up electrons will travel through one of the F layers and the spacer until they reach the interface with the opposite magnetised material which only allows the conduction of down spins.

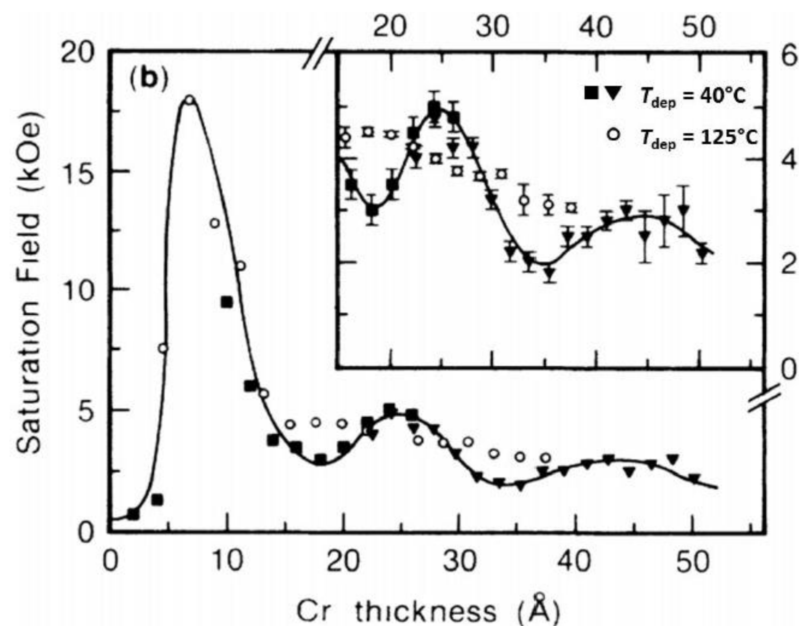

Figure 4.2: Dependence of indirect exchange coupling on the thickness of Cr spacer layer between two 2 nm thick Fe layers at 4.5 K [117].

The concept was introduced and studied by Ruderman, Kittel, Kasuya and Yoshida (RKKY) in order to explain the presence of exchange coupling in rare earth metals which have highly localised and ordered *4f* electrons despite their wavefunction not overlapping. In polycrystalline ferromagnetic thin films, the intergranular coupling mechanism is well known and is assumed to arise from RKKY interactions across

grain boundaries. In polycrystalline antiferromagnetic (AF) films, there is little to no intergranular coupling. This is because the moments within the bulk of the grains are fully compensated and the uncompensated spins at the grain boundaries are not sufficient to induce a dipole moment.

4.3 Magnetic Anisotropies

An important feature of long range ordered magnetic materials *i.e.* ferro, ferri and antiferromagnetic materials is magnetic anisotropy. This concept can be easily understood macroscopically and means that the magnetic properties of a material depend on the direction in which they are measured. Two main origins of anisotropy are identified: magnetocrystalline and shape. The competing dominance of anisotropies is system dependent and defines the shape of the magnetisation curve and as such an understanding of the role of anisotropies is required. There are a number of other induced anisotropies which arise as a consequence of external effects such as stress, plastic deformation and irradiation. A detailed description of these induced effects will not be given as they are external modifications of either the magnetocrystalline or shape anisotropies *i.e.* stress or strain induced to a single crystal will change the lattice constant along a single direction and induce a change in the magnetocrystalline anisotropy.

4.3.1 Magnetocrystalline Anisotropy

The magnetocrystalline anisotropy is an intrinsic material property which relates the magnetisation process to the crystallographic direction in a given crystal. If a cubic system such as iron is considered, the magnetisation curve is different when applying an external magnetic field along the three main directions of the unit cell: (100), (110) and (111). In other words, the magnetocrystalline anisotropy controls how easily magnetised a given crystalline structure is when an external field is applied on a certain crystal axis. Figure 4.3 shows an example of magnetisation curves for a bcc Fe unit cell.

The origin of the magnetocrystalline anisotropy can be attributed to the so called “crystal field” and it arises from the spin-orbit coupling and the coupling of orbital magnetic moments to the crystal lattice. As the orbital magnetic moments are

quenched by the crystal lattice, applying large magnetic fields will not result in reorienting the electron orbit.

Applying an external magnetic field will result in an attempt of aligning the electron spins which are coupled to the orbital angular momentum. As the orbital moments are immobile as discussed above, the material will oppose resistance to the spin orientation. An anisotropic material will therefore be more easily magnetised along a certain crystallographic direction also known as easy axis. The inverse mechanism where magnetisation requires a larger applied field defines the hard axis.

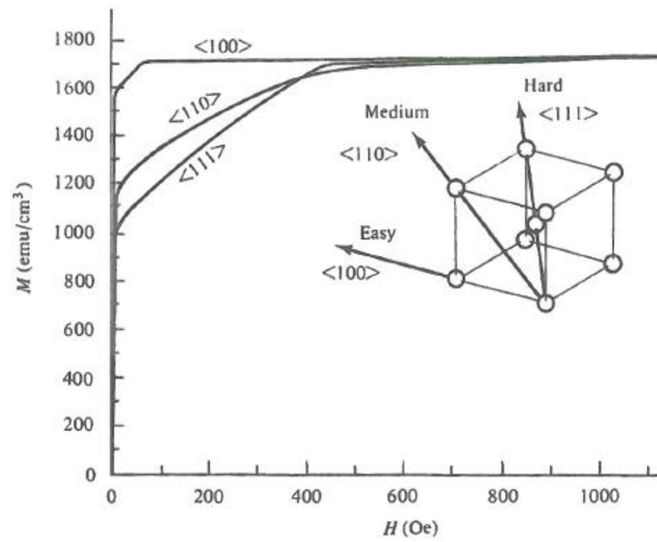

Figure 4.3: Magnetisation curves for bcc iron along different crystal axes [116].

To magnetise a sample along a direction which is not parallel to the easy axis, some work is spent to overcome the spin-orbit coupling. When saturation is achieved along the hard axis, the magnetocystalline (or crystal) anisotropy energy E_K can be expressed as a series expansion:

$$E_K = K_0 + K_1(\alpha_1^2\alpha_2^2 + \alpha_2^2\alpha_3^2 + \alpha_3^2\alpha_1^2) + K_2(\alpha_1^2\alpha_2^2\alpha_3^2) + \cdots \tag{4.3}$$

where $K_0, K_1, K_2 \ldots$ are anisotropy constants for a material at a particular temperature expressed in erg/cm^3 and $\alpha_1, \alpha_2, \alpha_3$ are the cosines of the angles between the magnetisation vector and the easy axis. This relationship applies to cubic systems such as Heusler alloys which have been studied in this work.

The magnetocrystalline anisotropy force can be understood in terms of a magnetic field attempting to hold the magnetisation parallel to a certain axis. The resulting field is called anisotropy field and is given the notation H_K. The torque exerted by the magnetocystalline anisotropy is dependent on the crystal structure, anisotropy constants, easy axis direction and occasionally the crystallographic plane in which *Ms* rotates away from the easy axis. The measurement of the anisotropy constant is not trivial and contains additive anisotropy contributions due to shape and induced effects *i.e.* stress which in the case of granular thin films are difficult to identify and separate. A special case is the determination of the antiferromagnetic anisotropy K_{AF} which is usually measured indirectly using the effect it exerts on a neighbouring ferromagnetic material via exchange bias [118] or by ferromagnetic resonance [119].

4.3.2 Exchange Anisotropy

The exchange anisotropy was discovered by Meiklejohn and Bean in 1956 [51] in Co/CoO core-shell nanoparticles when the nanoparticle system was cooled down from above T_N (CoO) = 293 K to 77 K in a saturating applied field, a shift in the hysteresis loop of the particles was observed as shown in Figure 4.4.

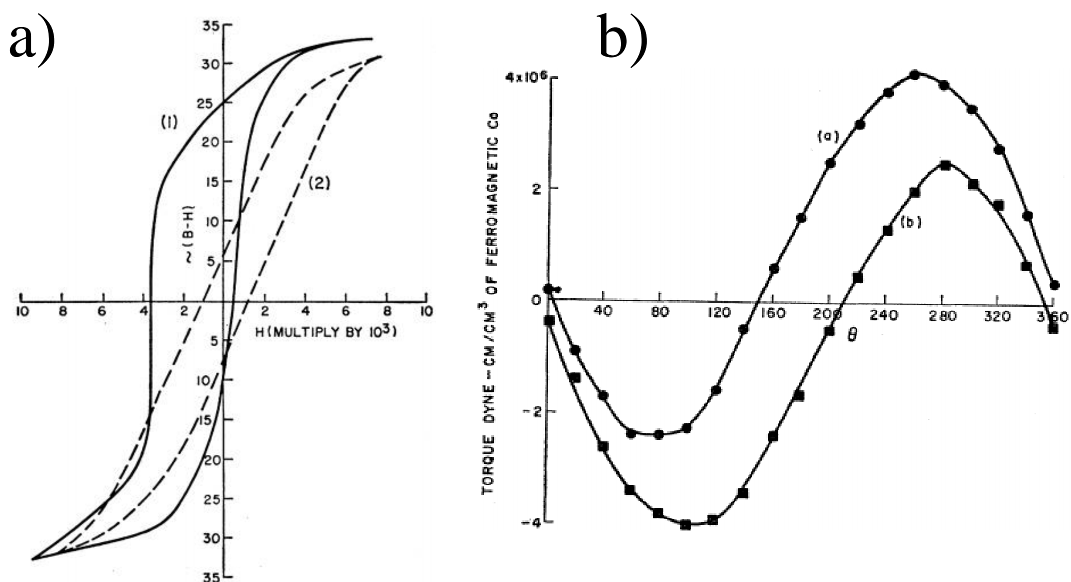

Figure 4.4: a) Shifted hysteresis loop and b) torque variation showing uniaxial induced anisotropy for the Co/CoO nanoparticle system [51].

The shift in the hysteresis loop shown in Figure 4.4 is defined as exchange bias and the associated field (H_{EX}) which is given by $H_{EX} = (|H_{C1}| + |H_{C2}|) / 2$ where H_{C1}

and H_{C2} are the points where the loop intersects the x axis which define the coercive field of the system. The loop shift is attributed to an interaction between the ferromagnetic Co and the antiferromagnetic CoO where the coupling between the two materials induces an additional uniaxial anisotropy on the F material. As shown in Figure 4.4b), the torque of the exchange bias system is proportional to $sin\ \theta$ where θ is the angle between the applied field used in the cooling process and the field used in the torque measurement.

The "new magnetic anisotropy" as it was described by the authors later became the basis for the stabilisation of magnetic sensors such as spin valve structures via the induced exchange anisotropy used as pinning mechanism for ferromagnetic thin films. Although the exchange bias mechanism is not entirely understood, the impact of the unusual loop shift on the modern data storage industry are presented in Chapter 3 and the underlying mechanisms of the interaction in polycrystalline thin films is described in Chapter 5.

4.3.3 Other Anisotropies

The effects of shape anisotropy in granular films with in plane magnetisation are considered negligible despite the non-spherical shape of the individual grains. Polycrystalline thin films are more than 90% dense therefore the formation of free poles is prevented.

Recent progress in spintronics is based however on perpendicular anisotropy induced in thin films. Magnetic memory devices such as perpendicular magnetic tunnel junctions use a combination of materials, deposition and processing techniques which allow for the reorientation of the easy axis out of plane. The technique is usually based on inducing lattice deformations using seed layers or long range coupled repetitive magnetic structures. More details about spintronic devices are discussed in Chapter 3.

When a magnetic material is saturated in an external field, a fractional length change along the magnetisation direction is observed. The phenomenon is known as magnetostriction and it originates from reorientation of atoms which minimises internal energy in the crystal structure. No external stress was applied for the samples in this study.

4.4 Magnetisation Reversal

The mechanism of magnetisation reversal in a crystalline magnetic material is difficult to predict due to the complexity and multitude of interactions which may affect the ordering as a function of the applied field, time and temperature. The complexity of the magnetisation process in real systems *i.e.* polycrystalline thin films arises from the intrinsic character of a many-body problem with more than one type of interaction to be considered. Moreover, as a result of the short range exchange interaction, microscopic effects usually induce important and observable perturbations in magnetisation. Predicting the magnetisation reversal process in real systems is still an important challenge and despite the complexity of the models proposed, they are usually based on fundamental processes such as coherent reversal also known as the Stoner-Wolfarth model or domain wall motion. These basic mechanisms will be discussed in detail in this section.

4.4.1 Domain Structures

The exchange interaction which was described at the beginning of the chapter is responsible for the parallel alignment of the electron spins in a ferromagnet (F) if the temperature is below the Curie point (T_C). This does not explain however how some ferromagnetic materials such as bulk iron is found in a demagnetised state. In an attempt to explain the unusual behaviour, at the beginning of the 20th century, *Weiss* postulated the spontaneous occurrence of magnetic regions called domains in the ferromagnetic material. If the domains have equal and opposite magnetisation, the resulting bulk moment will be zero.

Figure 4.5 shows that when a F material reaches saturation magnetisation (M_S) in a certain direction an opposing field is created as a consequence of flux closure. This is the demagnetising field (H_D) which stores the magnetostatic energy (E_{ms}):

$$E_{ms} = \frac{2}{3}\pi M_S^2 D_T \tag{4.4}$$

where D_T is the thickness of the domain. The equation gives the energy per unit area of the top surface. The magnetostatic energy is dependent primarily on the value of the magnetisation. In order to reduce this magnetisation, and therefore E_{ms}, a

magnetic material divides into domains. In a material with uniaxial anisotropy, the magnetic moments of different domains are opposed and preferentially lie along the easy axis of the unit cell.

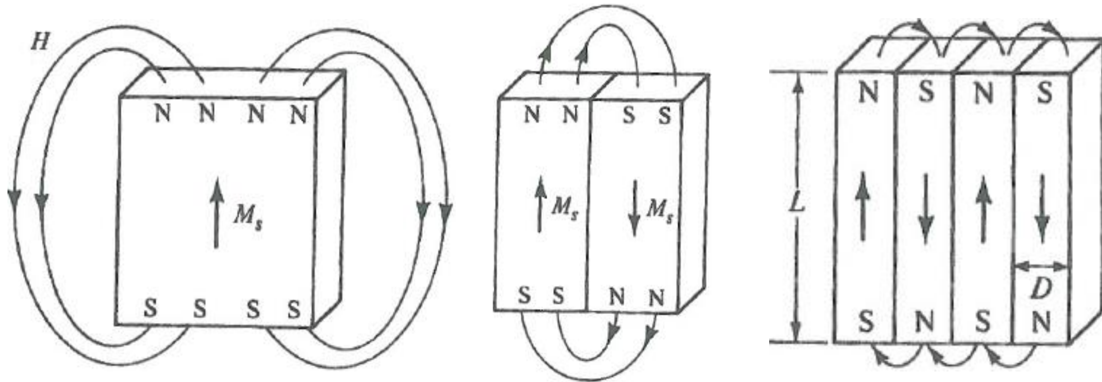

Figure 4.5: Division of a single crystal into domains [116].

It is also possible for materials to break into multiple domains for further reduction of H_D. In materials with cubic anisotropy such as Heusler alloys, the domain structure becomes more complex. As a result of the coexistence of multiple easy axes, domains with magnetisations aligned at 90° to each other can be formed.

4.4.2 Domain Wall Motion

The magnetisation process implies converting a multi-domain structure into a single domain via domain wall motion as shown in Figure 4.6. For large grain epitaxial systems or single crystal materials where the exchange coupling governs the reversal mechanism, the magnetisation switches via a series of processes such as domain nucleation, propagation and rotation which are shown in Figure 4.6. As domain wall movement is a low energy process, the application of low external fields will result only in domain wall movement while further increasing the field will cause the magnetisation of a single domain to rotate overcoming the anisotropy energy if needed.

In real systems which can have any number of imperfections such as structural defects, contamination or dopant inclusions, stress or other local variations of the anisotropy, domain wall motion is not smooth but rather subjected to strong local pinning events. Furthermore, in real polycrystalline thin films, due to the texture of

the material, there will be a distribution of easy axis across the grain size distribution. All these effects will contribute to modifications in the shape of a hysteresis loop. A schematic diagram of the magnetisation mechanism in a real system is shown in Figure 4.6.

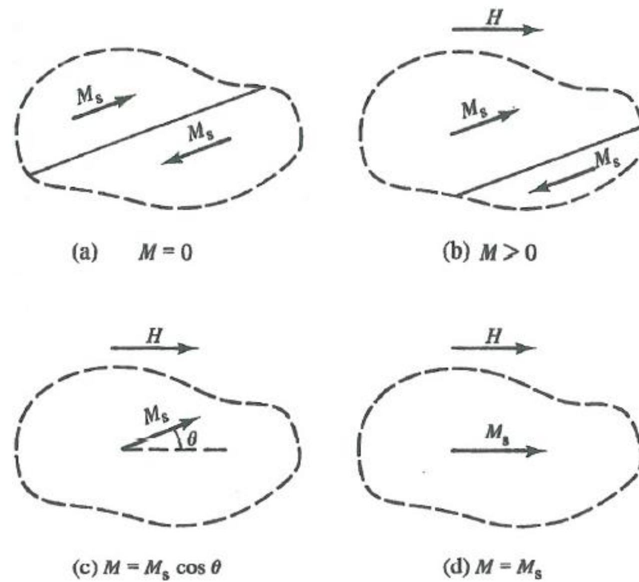

Figure 4.6: Schematic representation of (a) domain wall formation (b) domain wall movement (c) magnetisation rotation (d) and saturation magnetisation in a ferromagnetic material [116].

As shown in Figure 4.7 and discussed previously, the growth of domains in the magnetisation process requires domain wall movement. The motion of domain walls is not continuous due to the constant pinning and depinning of domain walls on crystalline defects known as "Barkhausen jumps" [116]. The effect is easily proven by magnetising a bulk ferromagnetic material placed in the centre of a coil. Due to the incremental movement of domain walls, the stray field generated by the bulk ferromagnet will change incrementally as well. The changes in flux will be signalled as voltage spikes in the inductive circuit.

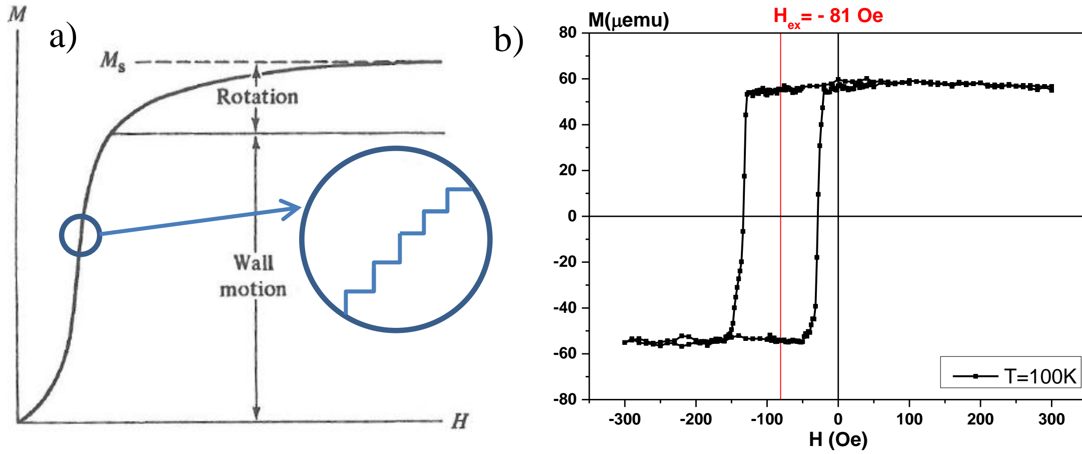

Figure 4.7: a) Schematic diagram of domain wall movement and corresponding Barkhausen effect [116] b) epitaxial Ru_2MnGe/Fe magnetisation loop where the reversal mechanism is based on rapid domain wall motion.

4.5 Single Domain Particles

When a magnetic material is not a single crystal or a large grain epitaxial system, the structure is divided into numerous small particles or grains which may consist of singular magnetic domains. The single domain state may be energetically favourable if for example the width of a domain wall is greater than the size of the particle or grain therefore not allowing enough space for a second domain to form. The more accurate approach for the single domain state involves comparing the different energy contributions associated to the fundamental interactions discussed at the beginning of the chapter. This means that in a given circumstance, the formation of a single domain in an entity has to be energetically favourable.

For simplicity, a spherical particle will be considered for which the magnetostatic energy, E_{ms} varies with the volume (D^3) as $E_{ms} \propto M^2$ and for which the domain wall energy varies as a function of the cross sectional area of the grain or particle (D^2). A critical size for a single domain spherical particle is estimated and given by the critical radius, r_c for single domain formation:

$$r_c \approx \frac{9\sqrt{A_{ex}K}}{\mu_0 M_S^2} \tag{4.5}$$

where A_{ex} is the exchange stiffness and K is the anisotropy constant.

Equation 4.5 gives an approximation for materials with large anisotropy. A comprehensive discussion about particle or grain parameters affecting the critical radius for single domain formation is found in O'Handley [115].

4.5.1 Magnetisation Coherent Rotation

Having previously discussed rather complex mechanisms of magnetisation reversal, we end up with what is considered the baseline knowledge in the field of magnetisation dynamics *i.e.* the single domain particle. The single domain particle was originally examined by Stoner and Wohlfarth [120] which considered the case of a prolate spheroid shape as shown in Figure 4.8.

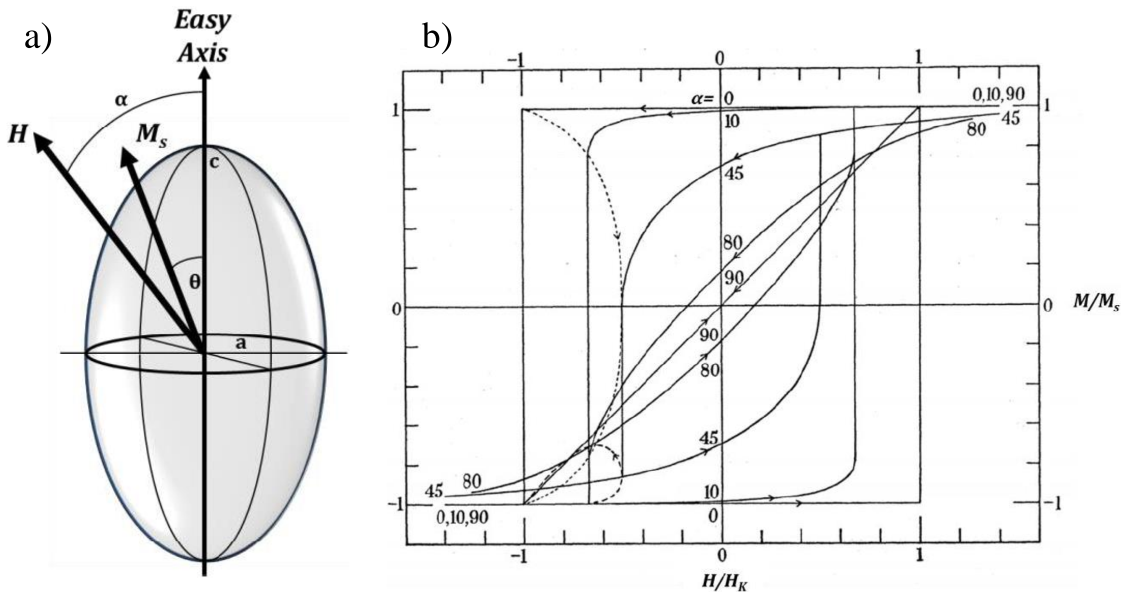

Figure 4.8: a) Schematic diagram of a Stoner-Wolfarth elongated particle and b) the associated hysteresis loops for different angles of the applied magnetic field [120].

The trivial situation for the single particle system is found when the magnetisation and the applied field are parallel to the easy axis set by the shape anisotropy. In this case, the energy required to rotate the magnetisation through the particle is a product of the particle volume V and the anisotropy K:

$$\Delta E = KV \tag{4.7}$$

where ΔE is the energy barrier to reversal and represents the external energy provided by the magnetic field which is equal to the anisotropy energy at 0 K. The energy is also expressed in terms of an anisotropy field, H_K.

When the applied field is not collinear with the easy axis and the angle between the two directions is θ, the total energy of the system E_T at $T = 0$ is given by the anisotropy energy E_K and Zeeman energy E_Z.

$$E_T = E_K + E_Z = V[K_U sin^2\theta - HM_S\cos(\alpha - \theta)] \quad (4.8)$$

where θ is the angle between the magnetisation and the easy axis, K_U is the uniaxial anisotropy, M_S is the saturation magnetisation and V is the volume of the particle. When differentiating E_T with respect to θ the equilibrium position of M_S is found and in the general case is given by:

$$sin\theta cos\theta = H_n \sin(\alpha - \theta) = 0 \quad (4.9)$$

where the component of the magnetisation in the direction of the field is given by $M_n = \cos(\alpha - \theta)$ where H_n is the normalised field H/H_K and M_n is the normalised magnetisation M/M_S. M_n can be calculated as a function of H for different values of α by the second derivative of E_T. The resulting hysteresis loops obtained for a single domain particle are shown in Figure 4.8b). For $\alpha = 0$ the energy barrier to reversal coincides with the anisotropy energy but for $\alpha \neq 0$, torque is applied to the magnetic moment and a reduction of the energy barrier is observed shown by the reduction of the coercive field H_c.

The theory of coherent reversal is the basis used for the reversal mechanism considered in this work for polycrystalline thin films. It is worth remembering that some of the requirements of the magnetisation rotation model do not apply to real systems for which the particles or grains do interact with one another so domain wall motion may occur. Another requirement is for all the electron spins to remain parallel during the rotation process which is not the case for more complex spin dynamic mechanisms such as rotation. A limiting factor is the temperature which induces a considerable instability of the magnetic moment as discussed in Chapter 5.

5 The York Model of Exchange Bias

When an antiferromagnetic material is placed in intimate contact with a ferromagnetic material and field cooled through or from near its Néel temperature (T_N), a hysteresis loop shift (H_{EX}) and an increase of coercivity (H_C) are observed. The magnetic interaction is known as exchange bias (EB) and since the discovery of the phenomenon in 1956 [51], no unified theory was formulated in order to describe the effect. Some examples of the models designed to explain exchange bias were formulated by Meiklejohn and Bean [121] assuming single domain ferromagnetic (F) and antiferromagnetic (AF) materials with a flat interface. The domain state model [122] is based on formation of domains in the AF due to crystalline defects which lead to the formation of domain states. Fulcomer and Charap [123] introduced the first model for granular systems using AF oxides such as NiO and CoO. Despite the incomplete understanding of this remarkable and complex magnetic interaction, exchange bias has been extensively used in spin valve structures. The discovery and implementation of giant magnetoresistance (GMR) in devices such as hard disk drive (HDD) read heads from 1998 [75] created an opportunity for researchers to try and understand and improve the magnetic pinning mechanism especially in thin film structures with flat interfaces.

This work focuses on the York Model of Exchange bias which describes the interaction between an AF and F sputtered polycrystalline thin films. The York model answers some important questions regarding the mechanism, implementation and limitations of the exchange interaction in a granular thin film system used in industrial applications. The theory and experimental procedures can accurately determine the grain size and film thickness dependence of H_{EX}, the value of the antiferromagnetic anisotropy and the contribution of interface effects. The supporting experiments use sputtered thin films of IrMn and CoFe which are used exclusively in read head type devices [83].

5.1 Energy Barriers

Ferromagnetic materials

As shown by Brown [124], the magnetic moment of a single domain particle fluctuates around the equilibrium position. The reversal of the magnetic moment is possible when the thermal energy, $k_B T$ overcomes the anisotropy energy barrier. The Néel Arrhenius law describes the reversal of the magnetisation of a single grain and gives the relaxation time for this process as used by Fulcomer and Charap [123]:

$$\tau^{-1} = f_0 \exp\left[-\frac{\Delta E}{k_B T}\right] \tag{5.1}$$

where τ is the time in which the magnetisation decays to *1/e* (*e* is the base of the natural logarithm) of its initial value and f_0 is the oscillation attempt frequency of the magnetic moment due to thermal fluctuations. f_0 was measured to be $1\text{x}10^{11}$ s^{-1} [125]. Superparamagnetic behaviour occurs when the relaxation time is 100 s resulting in $\Delta E = 25\ k_B T$.

In order to determine the energy barrier to reversal, a simplified case of perfectly aligned single domain nanoparticles with the easy axis is considered aligned to the magnetic field. The system will exhibit a perfectly square hysteresis loop and the total energy associated with the reversal process includes the anisotropy energy, $KV \sin\theta$ and Zeeman energy, $-M_S VH \cos\theta$ as described in Chapter 4. The system has two stable states when the magnetisation is aligned or lies in the opposite direction of the magnetic field direction. The switching field required needs to be larger than the energy barrier which is the difference between the minimum and maximum energy state (ΔE) of the system and is given by:

$$\Delta E = KV\left(1 - \frac{H}{H_K}\right)^2 \tag{5.2}$$

where H_K is the anisotropy field of the ferromagnet which defines the maximum coercivity of the material. V is the volume of the grain (particle) and the K is the anisotropy constant. In real systems there is no single value of the grain volume and

anisotropy constant but rather a distribution of these values hence the energy barrier also becomes a distribution, $f(\Delta E)$.

Antiferromagnetic materials

The York Model is based on the single domain behaviour of the antiferromagnetic grains in a sputtered thin film hence applying the same considerations as described above, the energy barrier for a single domain AF grain is:

$$\Delta E = K_{AF}V\left(1 - \frac{H^*}{H_K^*}\right)^2 \quad (5.3)$$

where H^* is the exchange field from the F layer acting on the AF layer. H_K^* is defined as a pseudo-anisotropy field in the antiferromagnet. The value of the pseudo-anisotropy field and the exchange field are unknown. However we assume that H^*/H_K^* is small. Due to the polycrystalline nature of the AF, a distribution of anisotropies is expected similar to the case of the F layer.

5.2 Time Dependence

When a ferromagnetic material is subjected to an external field, the magnetisation does not reach a final value immediately. A delayed response is observed after a change in magnetisation due to magnetic viscosity. Street and Woolley [126] showed a logarithmic dependence of the magnetisation M as a function of time:

$$M(t) = constant + S(H)\ln\left(\frac{t}{t_0}\right) \quad (5.4)$$

where t_0 is a constant and $S(H)$ is the magnetic viscosity coefficient which is the rate of change of the magnetisation with $\ln t$ and it is positive with increasing applied fields. Considering that $\Delta E > 25k_BT$ the magnetic viscosity stays constant for long periods of time. $S(H)$ was calculated by Gaunt [127]:

$$S(H) = \frac{dM}{d(\ln t)} = 2M_s k_B T\, f(\Delta E_C) \quad (5.5)$$

where T is the temperature, M_s is the saturation magnetisation of the ferromagnet and ΔE_C is the critical energy activated at field H. The expression can be written for an AF material if P_{AF} is considered to be similar to the magnetisation in ferromagnetic materials:

$$S(H) = \frac{dM_{AF}}{d(\ln t)} = 2P_{AF}k_B T\, f(\Delta E_C) \tag{5.6}$$

where P_{AF} is the saturation value of the antiferromagnetic order. In a granular AF system, the energy barrier for switching a single grain is proportional to the grain volume [123]. A distribution of the grain volume leads to a distribution of energy barriers. The $\ln t$ behaviour is characteristic for fine particle systems with a wide distribution of energy barriers [128] but does not apply for other systems. *El Hilo* showed that the logarithmic dependence is a particular case where $f(\Delta E(t))$ is constant over the time of the measurement [129]. The logarithmic time dependence of exchange bias was shown by Hughes [130] in measurements similar to those performed by van der Heijden [131].

5.3 The Setting Process

The "setting" of the antiferromagnet is performed by heating the material up to or above its Néel temperature (T_N) in a large enough field which brings the neighbouring ferromagnetic layer to saturation. The AF grains are then aligned by the exchange field H^* of the F layer as they become thermally active. The exchange bias (H_{EX}) was shown to be time dependent as seen in Figure 5.1 for the IrMn/CoFe systems used as a reference in this work, lower setting temperatures were used in order to prevent damage to the films.

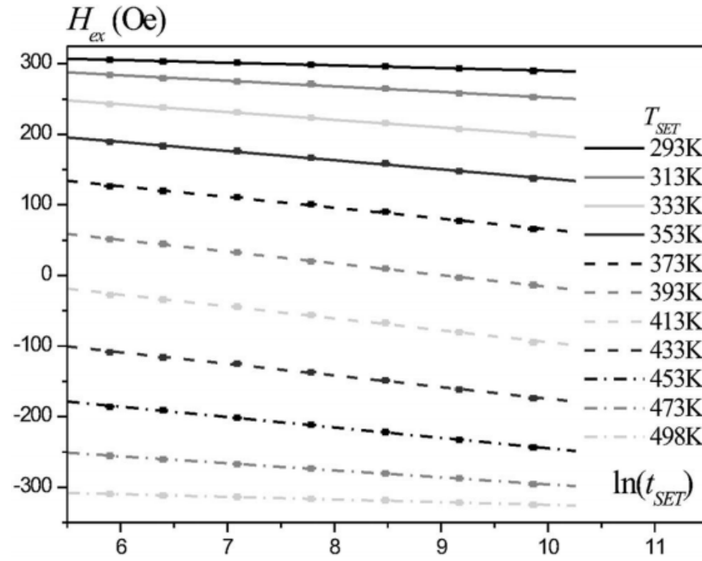

Figure 5.1: Time dependence of H_{EX} for the AF setting process [132].

The $\ln t$ dependence was verified by Vallejo-Fernandez *et al.* [132] in a measurement of the exchange bias at setting temperatures T_{SET} varying from 293 to 498 K. A linear relationship is observed when plotting $\ln t_{SET}$ against H_{EX}.

From the gradient of the straight lines, the magnetic viscosity is calculated using:

$$S(T, H^*) \ = 2P_{AF}k_BT\, f(V_{ACT}) \tag{5.7}$$

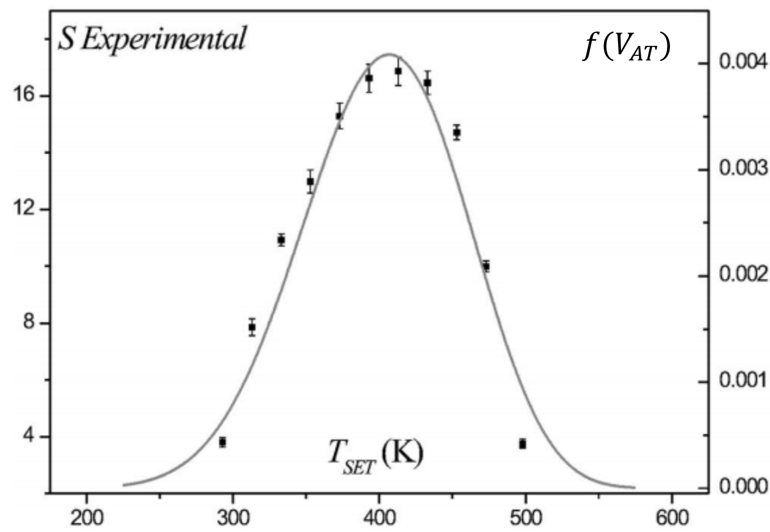

Figure 5.2: Magnetic viscosity as a function of T_{SET} [132].

where V_{ACT} is the volume of a grain for which the energy barrier to reversal is exceeded at a given temperature. The grain volume was measured by transmission electron microscopy (TEM) images as described in Chapter 7. The magnetic viscosity was then plotted as a function of temperature as seen in Figure 5.2.

As shown in Figure 5.2, some deviations occur at the extreme values of the temperature range which are attributed to uncertainties arising from the low number of counts of the very small and very large grains at the extremities of the distribution. The time and grain volume dependence of exchange bias results confirm the validity of the York Model for single domain AF grains.

5.4 Grain Volume Distribution

The time dependence of the setting process and the thermal instability of small AF grains suggest the existence of two critical volumes within the grain volume distribution of an antiferromagnet. As seen in Figure 5.3, V_C defines the lower grain volume limit under which thermal instability does not lead to exchange bias while V_{SET} defines the upper volume limit above which the thermal energy is not sufficient in order to set the AF grains. The exchange bias can therefore be considered proportional to the fraction of the grains lying between the defined limits:

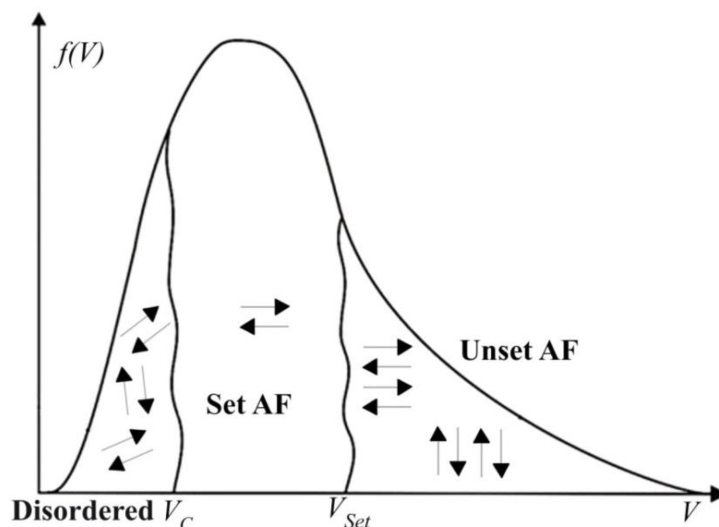

Figure 5.3: The grain volume distribution showing the critical volumes.

$$H_{EX}(T_{ms}) \propto \int_{V_C}^{V_{SET}} f(V)dV \tag{5.8}$$

Considering that the relaxation time for a single domain AF grain is given by the Néel-Arrhenius law as seen in Equation 5.1 the boundary volume values for the contribution to exchange bias are found as:

$$V_{SET} = \frac{k_B T_{SET} \ln(f_0 t_{SET})}{K_{AF}(T_{SET})} \tag{5.9}$$

$$V_C = \frac{k_B T_{ms} \ln(f_0 t_{ms})}{K_{AF}(T_{ms})} \tag{5.10}$$

where T_{ms} and t_{ms} are the temperature and time of the measurement respectively.

The grain volume distribution leads to a distribution in energy barriers. The York Model assumes a constant value for the anisotropy of each grain. This means that the grain volume distribution controls the energy barrier distribution. These considerations determine a distribution of blocking temperatures (T_B) which means that each grain has an individual T_B at which it becomes thermally unstable and can suffer thermal activation. The blocking temperature is defined as the temperature at which the exchange bias becomes 0.

$$K_{AF}V = \ln(t_{ms} f_0)\, k_B T_B \tag{5.11}$$

Sputtered polycrystalline materials usually have a grain size distribution which follows a log normal function.

5.5 The Blocking Temperature in Antiferromagnets

Similar to superparamagnetism occurring in small ferromagnetic particles as mentioned in Section 5.1, thermal fluctuations can lead to switching of the AF grains. As discussed in the previous section the distribution of energy barriers is dictated by the grain volume distribution and has two limits of unstable low energy small grains and high energy large grains which cannot be oriented by thermal activation.

Conventional blocking temperature measurements for exchange bias systems record hysteresis loops at constantly increasing temperatures until the loop shift (H_{EX}) becomes zero. This method leads to the determination of the maximum blocking temperature corresponding to the grains with the highest energy barrier. Another issue consists in the logarithmic time dependence of the magnetisation as shown previously which introduces a variation of the values measured in different conditions.

The York protocol is able to avoid these variations by always measuring the magnetisation curve at the temperature of non-activation of T_{NA} which is determined by reversing the magnetic field used in the setting process while keeping the measurement temperature constant. If the temperature allows for thermal activation of the AF grains which is observed by decreased H_{EX} values, a lower value of the temperature must be tested by trial and error.

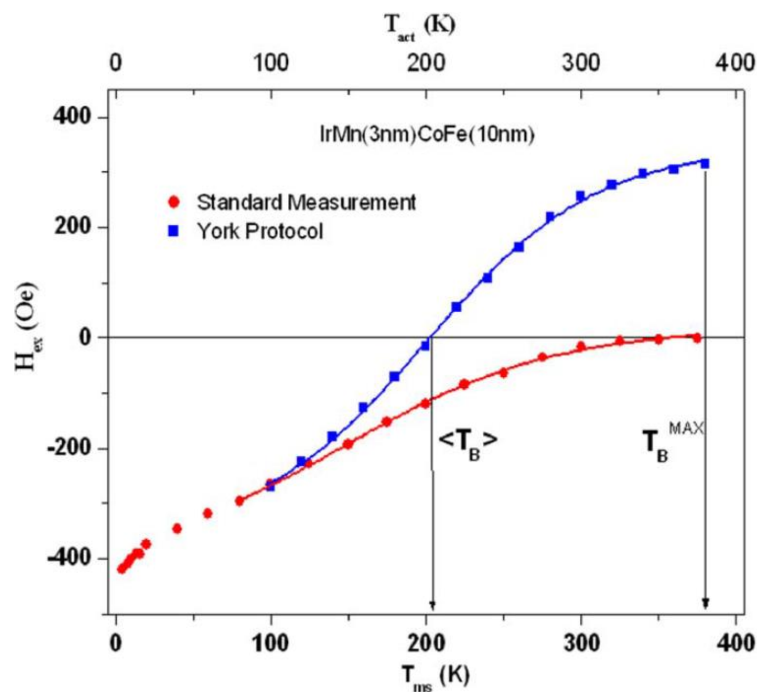

Figure 5.4: Standard thermal activation process compared to the York protocol [83].

In the York protocol, the average (median) blocking temperature, $<T_B>$ is determined and corresponds to equal and opposite oriented portions of the antiferromagnet in the thermal activation process. The grains which are activated at this temperature determine the median grain volume V_{med}. Figure 5.4 shows a

comparison between the York model and traditional blocking temperature measurements.

A measurement procedure was developed in order to obtain reproducible results by Fernandez-Outon *et al.* [133]. A detailed review of the York protocol for exchange bias measurements is found in Section 6.3.3.

5.6 The Anisotropy Constant

The measurement procedure for accurate determination of the antiferromagnetic anisotropy constant was developed by Vallejo-Fernandez [118]. The detailed thermal activation process begins after the exchange bias sample is field cooled to T_{NA} after being set at temperature T_{SET} and time t_{SET} as discussed previously. The applied field is then reversed in order to reverse the direction of the magnetisation of the F layer. The sample is then heated to an activation temperature T_{ACT} and held there for an activation time t_{ACT}. A portion of AF grains will activate or switch during this process. The sample must be cooled down to T_{NA} in order to avoid any additional thermal activation. T_{NA} is the only temperature used for the measurement of hysteresis loops. The thermal activation process is iterated until the AF is completely switched and the loop shift changes direction.

As T_{ACT} increases, an increasing fraction of the AF grains will be oriented in the opposite direction. The value of H_{ex} measured after an activation step is given by:

$$H_{EX}(T_{ACT}) \propto \int_{V_{ACT}}^{V_{SET}} f(V)dV - \int_{0}^{V_{ACT}} f(V)dV \tag{5.12}$$

where V_{ACT} is the volume of the largest grain that can be thermally activated at T_{ACT} and is given by:

$$V_{ACT} = \frac{k_B T_{ACT} \ln(f_0 \times t_{ACT})}{K_{AF}(T_{ACT})} \tag{5.13}$$

When increasing T_{ACT}, there is a point when H_{EX} becomes zero and as shown in Equation 5.12, there is an equal fraction of AF grain volume distribution oriented in opposite senses. This occurs at the median volume, V_{med} of the measured grain size

distribution. The temperature corresponding to H_{EX} = 0 is the median blocking temperature $<T_B>$ as seen in Figure 5.4. Combining Equations 5.1 and 5.3 results in:

$$K_{AF}(< T_B >) = \frac{k_B < T_B > \ln(f_0 t_{SET})}{V_{med}} \tag{5.14}$$

The York Model calculates the value of K_{AF} when equal fractions of the AF grains are oriented in opposite directions partially cancelling the effect of the interfacial spin disorder which is grain size dependent. The model also assumes the temperature dependence of the AF anisotropy of IrMn as:

$$K_{AF}(T) = K_{AF}(0)\left(1 - \frac{T}{T_N}\right)^n \tag{5.15}$$

This is because the temperature dependence of the sublattice magnetisation of the AF is given by $P_{AF} \propto (T_N - T)^{\frac{1}{3}}$ and $K_{AF} \propto P_{AF}^3$. [134]. Accurate and reproducible measurements of K_{AF} require similar methods for determining $<T_B>$ and T_{NA} which can be realised by using the York protocol presented in Section 6.3.3.

5.7 Grain size and Film Thickness Dependence

There are many reports in the literature relating the magnitude of exchange bias to the thickness of the AF layer. H_{ex} is reported to increase with the thickness of the AF (t_{AF}) while for large thicknesses an inverse relationship is observed.

$$H_{ex} \propto \left(\frac{1}{t_{AF}}\right)^n \tag{5.16}$$

The parameter n ranges from 0.3 in FeMn [135] to 1 in CoO [136]. For granular AF systems no definitive trend is reported. Both the increase and decrease [137] of H_{EX} with the film thickness have been observed. Vallejo-Fernandez reported experimental results for CoFe/IrMn systems with different thicknesses of IrMn [138]. Figure 5.5 shows the measured grain size distribution for different values of t_{AF} and their relationship with calculated critical volumes after measuring K_{AF} using the York protocols.

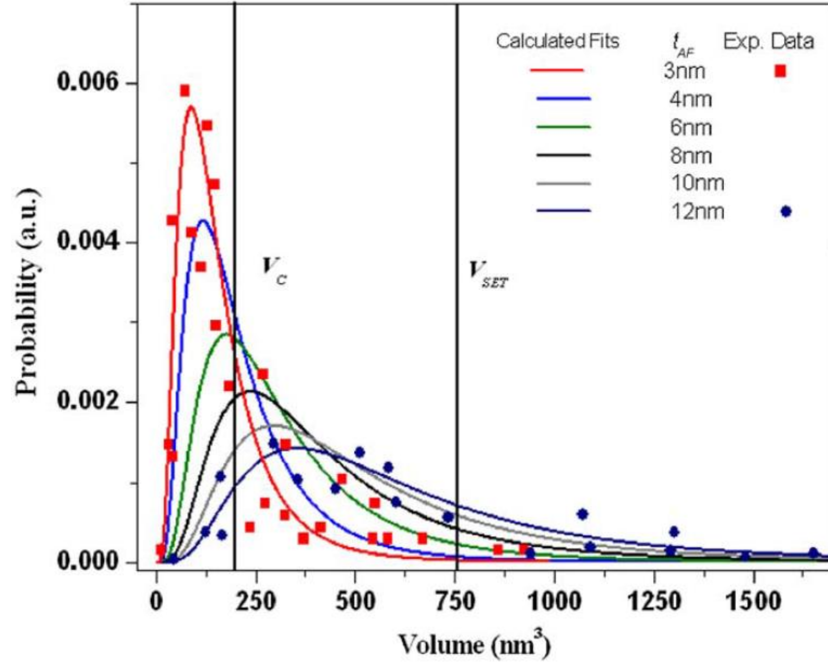

Figure 5.5: Grain volume distributions and critical volumes for varying thicknesses of IrMn [138].

As shown in Figure 5.5, different fractions of the grain size distributions fall within the critical volume range which means that the relationship between the thickness of the AF later (t_{AF}) and H_{EX} is not simple. Magnetic measurements show an increase of H_{ex} with the lateral grain diameter for AF thicknesses of 4 and 6 nm. For t_{AF} = 12 nm, H_{EX} shows a maximum value and decreases with the grain diameter as seen in Figure 5.6. When comparing the results with the grain size distribution shown in Figure 5.5, for t_{AF} below 6 nm, a large number of grains are thermally unstable and cannot contribute to the exchange bias. For thicker AF layers, a large number of grains fall within the requirement for stable volume but when the grains are too large, they cannot be aligned in the setting process therefore H_{EX} decreases.

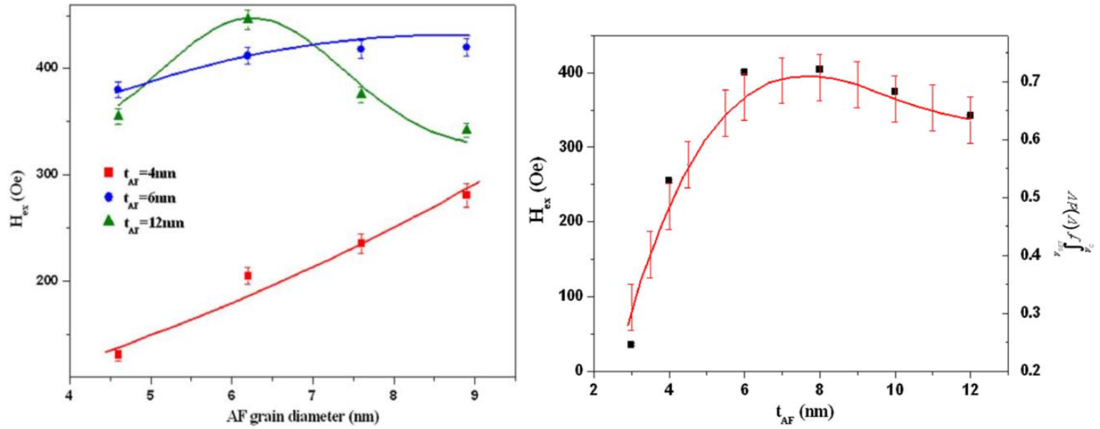

Figure 5.6: Variation of H_{ex} with t_{AF} and grain diameter for IrMn/CoFe [138].

The York model was verified for sputtered polycrystalline exchange bias systems with grain sizes ranging from 5 to 20 nm where the single domain behaviour of the AF crystallites is verified. For large granular structures (~50 nm), epitaxial or single crystal systems the mechanism of exchange bias is not well understood.

Kaeswurm *et al.* [139] proposed a strong domain wall pinning model which is able to interpret previous results observed on the effect of dopants and defects on exchange bias in MBE-grown single crystal or epitaxial large grain systems. The experiments show an increase of H_{EX} up to a threshold value of Cu dopant concentration of He ion irradiation followed by a steady decrease above the threshold value. The authors attribute these results to the generation of strong domain wall pinning sites created by inducing defects in the epitaxial structures thus increasing the anisotropy of the AF. Exceeding the optimal defect concentration may result in the formation of small unstable AF grains which become thermally active at low temperatures.

6 Sample Fabrication and Magnetic Characterisation

The recent developments in data storage and non-volatile memories require a constant improvement and increasing performance of the thin film deposition systems. From the industrial point of view, thin film parameters such as purity, homogeneity, stoichiometry, roughness, thickness, crystalline structure, grain size have to be easily and finely controlled. Throughput is another decisive factor when mass production is involved. Given the existing requirements, only vacuum based thin film deposition techniques will be discussed in this chapter. The solution based methods have the advantage of being able to coat large surfaces and might be more cost effective but the thickness control, film purity and stoichiometry control in case of ternary alloys renders the method unsuitable for this study.

6.1 Methods of Thin Film Deposition

Among the vacuum assisted deposition methods, the most widely used systems are based on Physical Vapour Deposition (PVD) and Chemical Vapour Deposition (CVD). The processes within the two methods are very similar with the addition of a reactive element introduced in the chemical process in order to promote the formation of the sought compound. As the majority of the systems discussed use plasma as a sputtering agent, the addition of a suitable reaction gas to a PVD system can easily turn it into CVD. The only possible limitation of such an upgrade is the ionisation energy of the reactive gas but the electric field used to generate the plasma usually exceeds the ionisation of all inert gases [140]. A prime example of a PVD system which is widely used in the data storage industry and nanotechnology is the magnetron sputtering [141].

6.1.1 Magnetron Sputtering

Magnetron sputtering is an adaptation of the direct current (DC) cathode sputtering process in which a cathode target and substrate are placed in a parallel plate capacitor layout where the target is connected to a high voltage (1-2 kV) power supply. As this system sits in an evacuated chamber where a small amount of process

gas is introduced, plasma is ignited between the metallic target and substrate. The ionisation of the process gas is explained using the premises of floating free electrons near the cathode [141]. These electrons are subjected to acceleration caused by the supplied negative electric potential and collide with existing gas atoms. With a sufficient amount of energy, the collision results in a positive gas ion (*e.g.* Ar^+) and at least one free electron which continues to collide with other atoms starting a "Townsend avalanche" process described by Equation 6.1.

$$\frac{I}{I_0} = e^{\alpha_T d_{ele}} \tag{6.1}$$

where I is the current flowing through the discharge, I_0 is the photoelectric current generated at the cathode surface, α_T is the first Townsend ionisation coefficient expressing the number of ion pairs generated per unit length by an anion and d_{ele} is the distance between electrodes.

The resulting positive ions are then accelerated towards the target where the collision causes atomic and cluster displacement from the metallic surface. The cathode material is therefore sprayed onto the inner surface of the substrate and chamber.

The magnetron configuration includes a system of permanent magnets or electromagnets placed beneath the target as shown in Figure 6.1 where the motion of an electron in the presence of a magnetic field is described by the Larmour rotation. In this case, the electron orbits around the field lines with a frequency $\omega = q_e B/m_e$ where $\boldsymbol{B}$ is the magnetic flux, q_e is the charge and m_e is the mass of the electron. The radius of the motion (R_L) is given by Equation 6.2

$$R_L = \frac{m_e v_e}{eB} \tag{6.2}$$

where v_e is the velocity of the electron perpendicular to the direction of the magnetic field.

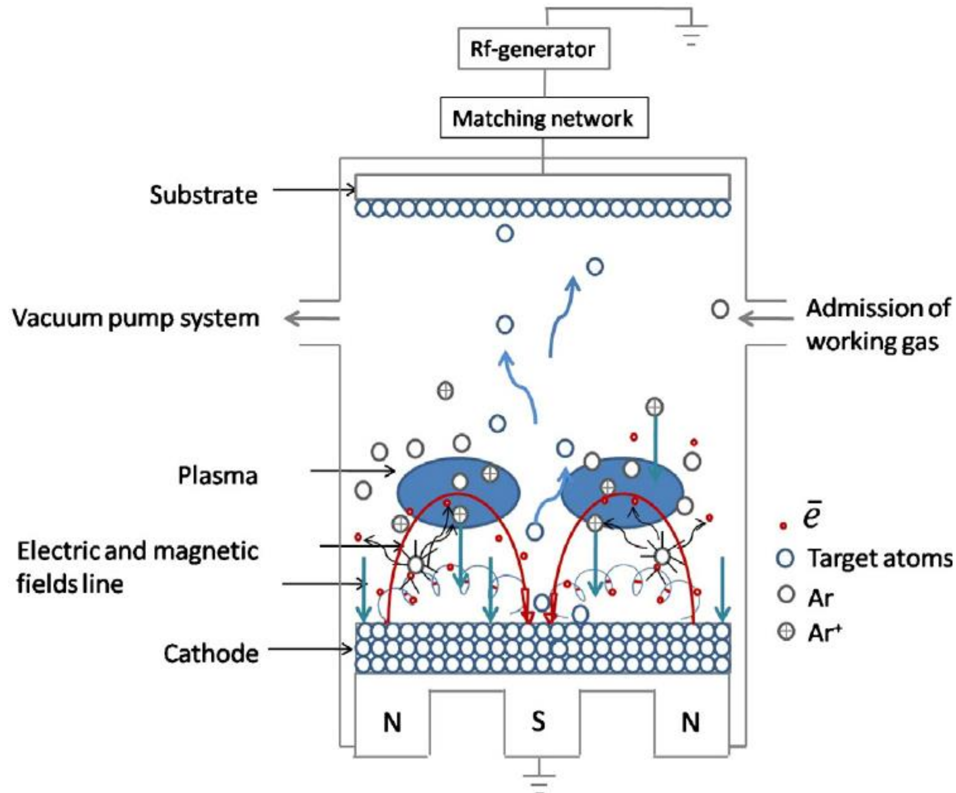

Figure 6.1: Schematic diagram of a radio frequency (RF) magnetron sputtering system [142].

The layout of the magnets underneath the cathode, causes the electrons to bounce between the magnetic poles due to the magnetic mirror effect [141] as an addition to the spiralling movement increasing the travel path and therefore the probability of ionisation (increased sputtering rates). Considering that the electron density is higher where $\boldsymbol{B}$ is parallel to the target, the sputtering will occur mostly underneath this region and following the arrangement of the magnets, the cathode will be eroded in the shape of the electron trajectory. A circular trench or “racetrack” is usually created in the target as seen in Figure 6.2 and the target utilisation is around 30%.

Initial studies conducted by Anderson *et al.* [143] showed a negatively “self-biased” behaviour of the applied voltage in relation to the plasma potential. As the electronic mobility is much larger than the ionic one, the lack of the negative bias will cause an accumulation of negative charges on the surface of the dielectric with no discharge path. The same negative surface charge which is now controlled via the self-bias effect also acts as a repelling field for the external electrons allowing only the

positive ions to surround the target surface. Given sufficient energy from the RF field, the ions will collide with the insulating surface and sputtering occurs. Due to the nature of the external electric field, the ionic collisions will only occur during the negative side of each period in order to neutralise the existing negative surface charge. The lowest reported frequency required for RF sputtering is around 10 kHz. For industrial purposes, the value of the frequency was chosen at 13.56 MHz and the signal is fed to the plasma via an impedance matching unit. Higher frequencies can be used and they affect the sputtering rate through the energy of the incident ions. The process is limited by the relative low mobility of the heavy ionised species. A blocking capacitor can also be used especially for depositing metallic compounds when the residual charges are absorbed by the external circuit [144].

Figure 6.2: Unevenly eroded Ta magnetron target.

Magnetron sputtering is the most commonly used technique for industrial thin film deposition. The ability to deposit both insulating and conductive materials in reactive environments, the relatively fast deposition rate compared to an MBE system, the capability of depositing both epitaxial and polycrystalline thin films with the addition of a heated and rotating sample stage and the possibility of performing co-sputtering from up to four different targets make the magnetron the system of choice for controllable crystalline structures and alloy stoichiometry.

6.1.2 High Target Utilisation Sputtering (HiTUS)

The HiTUS sputtering system is based in the ionised physical vapour deposition (iPVD) concept and was developed by Plasma Quest Ltd. The ionisation of the sputtering gas occurs in a quartz side arm outside the deposition chamber as seen in Figure 6.3. A 13.56 MHz radio frequency (RF) 2.5 kW field is applied via a matching unit and a three turn coil wrapped around the side arm. The interface allows precise control of the RF power output and monitors the reflected power of the system.

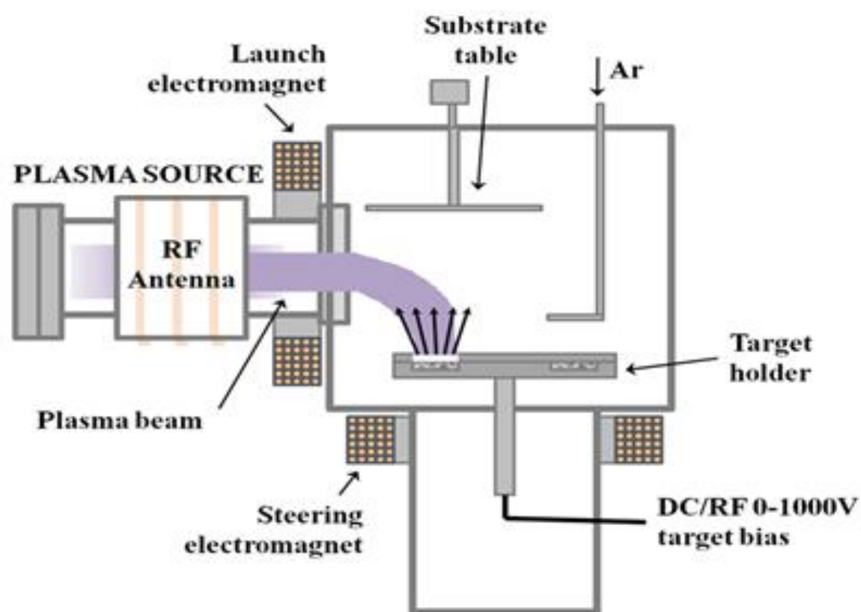

Figure 6.3: Schematic diagram of the HiTUS sputtering system.

Using a series of rotary, turbo and a cryogenic pumps, the base pressure of the sputtering chamber reaches values lower than $5x10^{-7}$ mbar. The cryopump has two cooling stages and a He recirculating compressor which allows the bellows on the back of the chamber to reach a temperature of 9 K. A pneumatically operated gate valve separates the deposition chamber from the cold side of the cryopump using a mechanical throttle and position locking nut. The system allows for different relative positions of the gate valve and therefore different flow rates of the chosen sputtering gas at a constant process pressure of $2.4x10^{-2}$ mbar.

The plasma ignited in the side arm is confined by an electromagnet to a beam with a 5 cm diameter which is steered by a second electromagnet onto the metal target. The rotating, water cooled target plate can fit up to 8 targets for multiple layer deposition. A high voltage power supply is used to apply a bias voltage (V_B) of up to -1000V to the target in order to accelerate the ionised Ar^+/N_2^+ towards the target and increase the sputtering rate and therefore the grain size [145].

The HiTUS uses close to 90% of the sputtering target due to the isotropic plasma beam. As the system does not allow for co-sputtering, the 6 cm diameter targets require a custom design with 16 drilled holes as seen in Figure 6.4. The design allows the insertion of pure metal pegs in the target. The technique is used for doping and compensating stoichiometric imbalance especially in ternary compounds such as Heusler alloys.

Figure 6.4: Powder pressed custom drilled target with doping pegs.

The substrate carousel can accommodate up to 6 custom made sample holders. Circular and rectangular substrates can be used ranging from 5x5 mm^2 to 20x20 mm^2 area. The holders can also fit two 3 mm diameter TEM grids for structural studies and grain size analysis. A radiative substrate heating system was fitted to the system in order to promote crystallisation of alloy films by *in situ* annealing.

The growth rate is monitored constantly using a high frequency piezoelectric crystal placed in the vicinity of the substrate. Typical sputtering rates vary from 0.01 to 0.5 nm/s depending on the material and sputtering conditions. A calibration is performed for every new target in order to determine the correction factor (tooling factor) of the deposition rate monitor. For this work, cross sectional TEM images of multilayer structures and AFM analysis of film edges after a lift-off procedure were performed for the thickness calibration. The substrate temperature does not usually exceed 100°C in order to exclude annealing effects from the deposition.

A thorough cleaning is required every time the system is vented in order to minimise contamination. A sequence of target and substrate cleaning was developed in order

to prepare the surface of the targets and substrates. Ar gas, a bias voltage of 900V and 60% (1.25 kW) of the maximum RF power are the parameters used for target cleaning. The pre-sputtering process can extend up to 30 min in the case of powder pressed targets which have a porous surface and develop a thick layer of oxide. The pre-sputtering is broken down into steps due to outgassing caused by the plasma beam interaction with the surface of the target. The increase of process pressure due to outgassing causes unstable deposition rates and contamination of the thin films. The substrate cleaning was performed by allowing the plasma to reach the top of the chamber when switching the steering electromagnet off. The interaction with the plasma removes contaminants from the surface of the substrate. In the case of Si single crystal substrates, the cleaning process does not remove the surface SiO_2 amorphous layer as observed in cross sectional TEM as seen in Chapter 7.

6.2 Sample structures

In order to assess the crystalline quality and the magnetic properties of the thin films, a number of sample structures were selected. This allows for the results to be quantified and easily compared especially when different alloys are used for the same purpose.

For X-Ray diffraction studies (XRD), the ideal stack would be formed from the substrate and a relatively thick metallic film in the range of 100 nm as seen in Figure 6.5 This structure allows for a better signal to noise ratio during measurements and excludes uncertainties and parasitic reflections from a multilayer structure. A capping layer is required as surface oxidation can introduce secondary phases within the alloy film. The capping layer is also necessary when post-annealing the samples in vacuum or a controlled atmosphere. Ru, Ta and Al were used as capping layers. Ta is preferred as it forms an amorphous layer but the high density of the material can be detrimental to XRD measurements and therefore a 2 nm thick capping layer was chosen. Aluminium has the advantage of the low atomic number and forms a stable oxide phase but the hygroscopic nature of the oxide can lead to deterioration of the films studied [146].

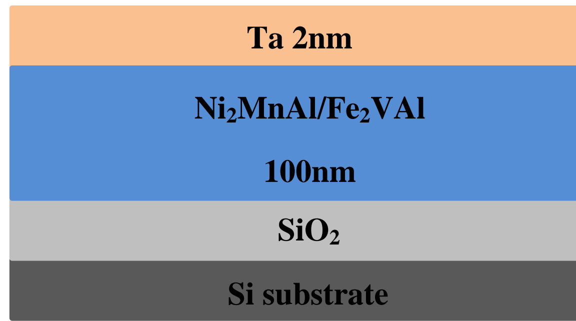

Figure 6.5: Schematic diagram of Heusler alloy sample structure for XRD analysis.

In order to promote crystallisation at low temperatures or in the as deposited state, a set of Cr and Ag seed layers was used. As shown by Sagar *et al.*, the lattice matched Ag seed layer improves the crystallisation of the Heusler alloy thin films. Structural studies on epitaxial samples have shown a small lattice mismatch of less than 5% between the two materials with the Heusler alloy unit cell offset by 45° and of the cube edges overlapping with the face diagonal of the Ag unit cell or MgO single crystal substrate as shown in Figure 6.6 [147]. The 3 nm thick Cr layer is deposited below the Ag layer in order to ensure adhesion to the substrate. A thicker Ag layer (30 nm) is required in order to prevent the island growth of the material and diffusion of the Cr atoms.

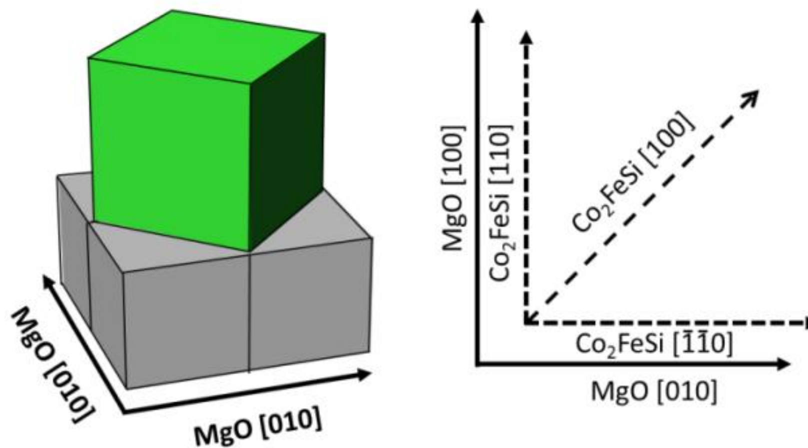

Figure 6.6: Schematic diagram of the relative position of a Heusler alloy unit cell in relation to a single crystal MgO substrate [40].

Both the thickness of the AF and F are crucial in order to maximise the exchange bias. Within the columnar growth approximation and considering the equation for the energy barrier $\Delta E = K\ V$, it becomes clear that the AF layer thickness and the anisotropy, K dictate the thermal stability and pinning strength. The same approximation limits the thickness of the F layer and therefore a 2 to 10 nm layer of

material deposited on top of the AF Heusler films. Exchange bias is inversly proportional to the thickness of the ferromagnetic layer. $Co_{0.6}Fe_{0.4}$ has a very large magnetic moment and was used in previous exchange bias measurements [83]. Co_2FeSi was also chosen for this study as it is one of the widely studied spin polarised ferromagnetic Heusler alloy [148] which allows for an almost perfect lattice match between the AF and F layers.

Lattice matching plays an important role in epitaxially grown Heusler alloys. A series of epitaxial and polycrystalline samples deposited via magnetron co-sputtering on MgO(001) and Si(001)/SiO_2 substrates were received from Tohoku University in Japan and Bielefeld University in Germany. The epitaxial samples use 10 to 100 nm of Ni_2MnAl and Ru_2MnGe as AF Heusler alloys [149]. A 2-3 nm thick layer of Fe, Co or Co_2FeSi were deposited as F layers. Ta and Al were chosen as capping layers.

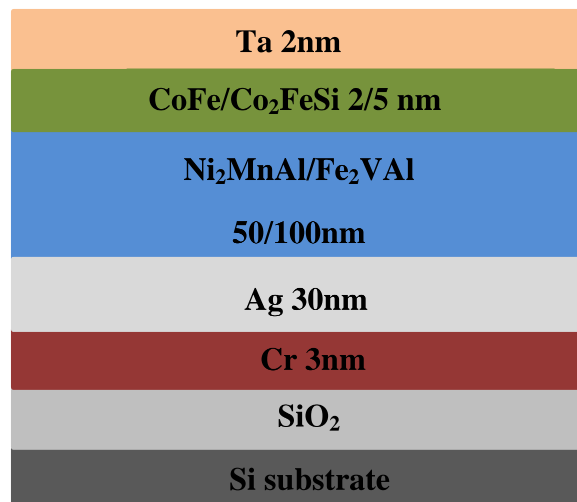

Figure 6.7: Schematic diagram of the exchange biased stack using Cr/Ag seed layers.

As exchange bias is partially an interface controlled effect, using AF/F bilayers such as Ni_2MnAl/CoFe or Ni_2MnAl/Co_2FeSi may limit the post-annealing temperatures and times due to interfacial mixing. This phenomenon is usually observed in magnetic measurements when the value of M_S drops, the value of H_C changes and the shape of the resulting loop is different. The probability of mixing is especially high when both the AF and F layers are Heusler alloys and six different elements gather at the interface. This increases the probability of secondary phase formation

or the crystallisation of a different Heusler structure provided the formation energy is favourable.

Polycrystalline MnN/CoFe systems were also studied. The samples were deposited via reactive magnetron sputtering in Bielefeld, Germany and the HiTUS system in York using a mixture of N_2 and Ar gasses as described in the previous chapter. For the samples grown by magnetron sputtering, a thermally oxidised Si substrate was used. A 10 nm Ta seed layer is necessary for the crystallisation of the tetragonal AF θ phase and also for texturing the material with the (002) direction out of plane. The minimum film thickness for the nitride is around 30 nm [150]. The large grain dimension is necessary due to the decreased AF anisotropy of the MnN when compared to a 5 nm thick IrMn film currently used in HDD read heads [83]. A 1.8 nm thin layer of $Co_{70}Fe_{30}$ was for the bilayer exchange bias system. A Ta/TaO_x capping layer was used to prevent the oxidation of the ferromagnet as seen in Figure 6.8.

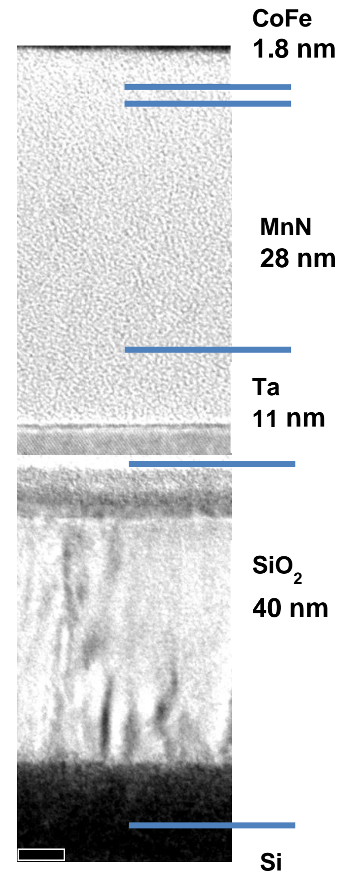

Figure 6.8: Cross sectional TEM image of the MnN/CoFe specimen.

6.3 Magnetic Characterisation

The nanometre scale spin electronic devices which include magnetic multilayer structures require precise magnetic characterisation tools. Ideally, the characterisation tool must be able to record the variation of the magnetisation of a thin film with respect to the applied field, time and temperature. The measurements also need to be consistent and reproducible. Magnetic characterisation can be performed using detection coils or Kerr effect based systems. The latter uses helicity of the light and the interaction with an atomic magnetic moment in order to plot the magnetisation as a function of the applied field. Open or closed coil systems are usually used for magnetisation measurements. Closed coil systems include AC and DC *B*-*H* loop tracers and are used for high frequency susceptibility measurements or low field hysteresis loops. For this work, open circuit magnetometers were used *i.e.*

an alternating gradient force magnetometer (AGFM) and a vibrating sample magnetometer (VSM).

6.3.1 Alternating Gradient Force Magnetometer

The alternating gradient force magnetometer is one of the most sensitive systems available for magnetisation measurements with a noise base as low as 2×10^{-8} emu in air and 10^{-11} emu when the system is in vacuum [151, 152]. The AGFM is the successor of the Reed magnetometer which used a static field gradient and the deflection of a thin wire to measure the state of magnetisation [153].

The Princeton Measurements Corporation (PMC) Micromag model 2900 shown in Figure 6.9 was used for fast and efficient magnetic characterisation of Heusler alloy thin films. Compared to previous instruments, the AGFM utilises some basic mechanical principles in order to enhance precision measurements. An alternating gradient field of 0.04 to 4 Oe/mm is superimposed over the static DC field generated by the main coils. For maximum mechanical energy transfer, the AC field gradient is tuned to the resonant frequency of the probe and sample assembly.

The transducer consists of the probe which uses a small piezoelectric silver coated lead-zirconate-titanate (PZT) bimorph attached to a thin quartz sample stage and two quartz rods (legs) in a geometry having a resonant frequency induced by the AC gradient field of 200 to 1000 Hz. The bimorph converts the mechanically induced stress caused by the sample movement in the gradient field into detectable voltage. The force induced on the piezoelectric element is given by:

$$F_i = m_i\left(\frac{dH_i}{d_i}\right) \tag{6.3}$$

where i is the arbitrary direction in space (i= x, y *and* z), m_i is the magnetic moment and dH_i/d_i is the field gradient measured along the direction chosen.

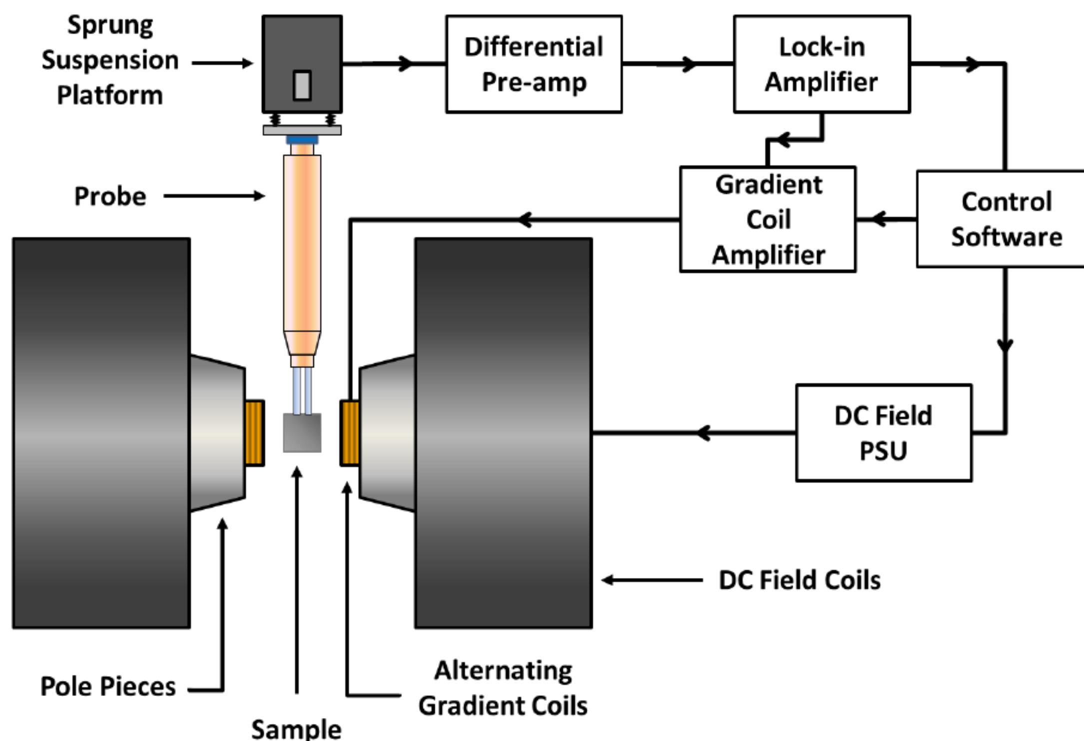

Figure 6.9: Schematic diagram of Micromag 2900 AGFM [40].

The sensitivity of the magnetometer is directly related to the properties of the probe assembly. As seen in Figure 6.9, the probe is held in place via a suspended platform and an outer brass jacket is used to protect the inner tubular structure. Both elements have a considerable mass and are used for inertial stabilisation of the probe. The resonant properties of the holder are dependent on the design, materials and dimensions of the plate and legs. When the system operates at resonance, a Q-factor ranging between 20 and 200 is calculated by the software [151]. The apparatus performs a calibration sequence where the field gradient is swept within the range of 100 to 1000 Hz and the resonant frequency is locked for the measurement.

The Micromag 2900 AGFM can perform a wide range of measurements including hysteresis loops, DC demagnetisation, isothermal remanence curves and also time-dependent magnetisation curves. The low impedance water cooled electromagnet produces a maximum field of 2.4 kOe when the pole spacing is 10 mm but more importantly has a high sweep rate and compact design. This allows for very fast hysteresis loop measurements typically measuring 500 points in 51 seconds for a ± 10 kOe applied field using an averaging time of 100 ms which makes the AGFM the perfect screening tool for magnetic properties.

One of the limiting factors associated with the AGFM is the weight of the sample which together with the quartz mounting plate should be kept at values lower than 100 mg. Heavy samples will have sufficient inertia so that the stress induced on the bimorph by the amplitude of oscillation is negligible. This consideration will also limit the dimensions of the samples measured. The increased sensitivity of the system requires a vibration free environment. Loud noises can affect the quality of the measurements. It is not common for the AGFM to have a temperature control mechanism as the addition of a cryostat induces mechanical noise which will be transferred to the sensing element. Finally, the coercivity values (H_c) may vary according to the strength of the field gradient and therefore careful setting of the magnetometer is required.

6.3.2 Vibrating Sample Magnetometer

The vibrating sample magnetometer (VSM) uses Faraday's induction law in order to measure the magnetisation of a body which is kept in a constant externally generated magnetic field. The detection system used for VSM is a set of coils positioned close to the sample which will record an induced electrical signal only when a time variation of the magnetic flux is detected. The total flux, ϕ_c passing through a coil of area A_c is described by:

$$\phi_c = (H + M)A_c \tag{6.4}$$

where H is the external applied magnetic field and M is the magnetisation of the sample. The induced electromotive force (emf) is:

$$emf = -N\frac{d\phi_c}{dt} \tag{6.5}$$

where N is the number of turns in the coil. Combining the previous equations:

$$\int emf\ dt = -N\ A_c\ M \tag{6.6}$$

Considering that H is constant for both the sample and the detection coil system, the only factor controlling the induced emf is the magnetisation$M$.

The magnetometer used for this study is an ADE model 10 vector VSM which has 2 pairs of detection coils placed in a perpendicular configuration. The detection system is integrated into an open circuit (flow) cryostat as shown in Figure 6.10 The paired detection elements allows for the system to be insensitive to signals arising from distanced dipoles. A number of detection coil configurations were reported with a common characteristic being the opposite direction of the windings which helps in adding the signal from the near magnetic dipoles (the sample) while subtracting any stray field induced emf [154].

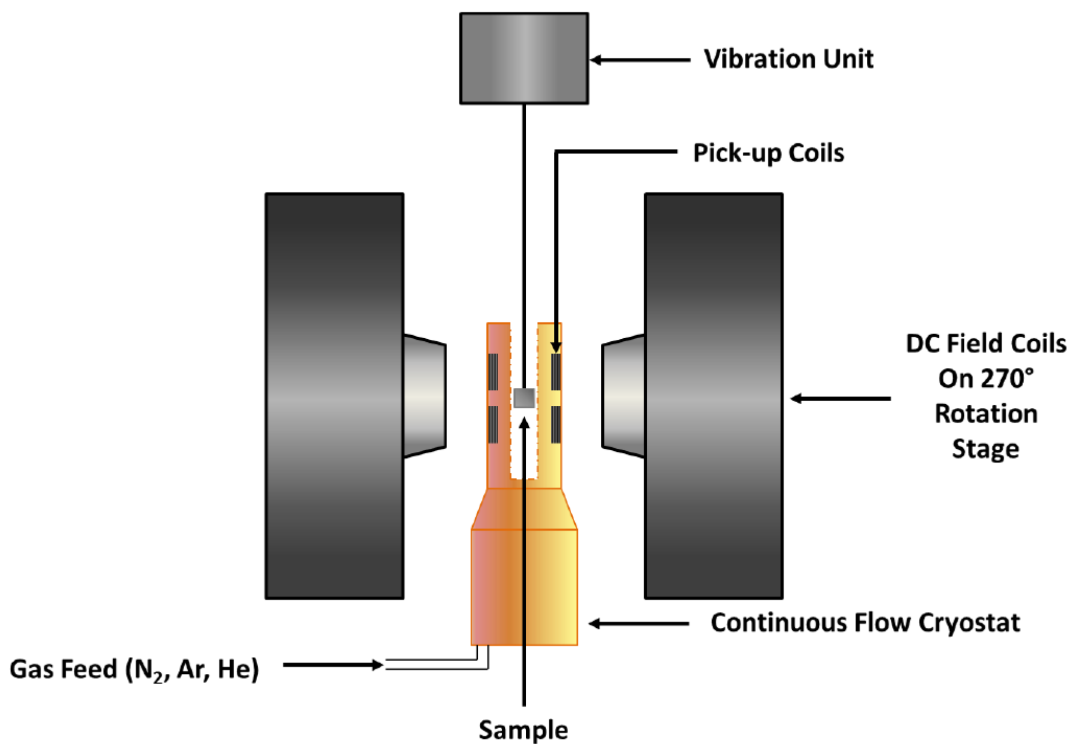

Figure 6.10: Schematic diagram of ADE model 10 vector VSM.

The resulting signal is channelled to a digital signal processor (DSP) lock-in-amplifier which is able to identify the waveform of the detected signal by comparing it to the signal sent to the vibration drive unit which can be a simplified and sturdy version of an audio speaker. The chosen frequency for the vibrating module is around 81 Hz. The lock-in-amplifier is able to filter out any noise from external sources and trace only the signal produced by the specimen.

The VSM is able to measure the values of magnetisation directly and accurately but it requires careful and consistent calibration when quantitative analysis is required. A consequence of the geometry of the machine is the necessity of aligning the sample

in between the detection coils in order to maximise the induced electrical signal and improve the signal to noise ratio (SNR). The calibration of the magnetic field strength is especially important for loop shift measurements and is performed for the 0 and 10 kOe points using zero field enclosure and a secondary standard gaussmeter.

The value of the magnetisation is calibrated using a sample of known magnetic moment. The material of choice for the calibration of both AGFM and VSM is palladium which is a Pauli paramagnet [155]. Pd has a perfectly linear magnetisation response in a field and high corrosion resistance therefore using the value of the magnetic susceptibility $\chi_{Pd} = 104.5$ μemu/Oe/formula weight and the mass of the calibration sample, an accurate value of the magnetisation for a given field can be determined. Two types of calibration sample were used in order to replicate the shape of the thin film through the deposition mask on the substrate: a round-edged square and a circle. The shape matching is designed to reduce the errors in calibration caused by demagnetising fields produced at the edges of the thin films.

The ADE model 10 VSM is equipped with a 20 kOe electromagnet with a pole piece spacing of 4 cm. The open flow cryostat has four pairs of detection coils for the in plane and perpendicular direction (x and y). The electromagnet assembly can rotate in the plane around the sample in order to perform anisotropy measurements. The cryostat uses a heat exchanger and a dewar of liquid nitrogen in order to cool the N_2 carrier gas hence the sample to a minimum temperature of 100 K. Nitrogen or argon are also used to create an inert atmosphere in the sample space when elevated temperatures are used during the field setting or annealing processes. The maximum temperature achievable in the VSM is 770 K.

Compared to the previously described AGFM, the VSM has a lower sensitivity of 10^{-6} emu. The addition of the cryostat increases the pole piece separation which reduces the maximum applied field. Using large electromagnets implies that the variation and stabilisation of the field is slower. As the oscillation frequency is set much lower than the resonant frequency of the AGFM measurements, the averaging time per point must also increase therefore the overall time required for a hysteresis loop measurement is usually between 20 and 40 minutes depending on the field range and step size.

The VSM is most definitely the first choice for precise and versatile magnetic measurements. Combining the measuring capabilities with a helium cryostat results in a complete system that can perform time, temperature and field direction dependent magnetisation measurements.

6.3.3 The York Protocol for Exchange Bias Measurements

The model 10 VSM can be used to measure the properties of antiferromagnetic (AF) materials in exchange bias systems by assessing a series of hysteresis loops from the exchange coupled ferromagnetic (F) layer in a controlled thermal activation process. Thermal activation measurements were used to determine the blocking temperature of granular and epitaxially grown AF thin films following a strict measurement sequence as shown schematically in Figure 6.11. The sequence is known as the York protocol [83] and the supporting theory was discussed in Chapter 5.

1. The AF thin film is set in a high enough magnetic field which saturates the neighbouring F layer (10-20 kOe) at temperature T_{set} for 90 minutes.
2. The sample is cooled down to the temperature of non-activation, T_{NA} which is determined by reversing the direction of the setting field, waiting for 30 minutes and measuring a loop.
3. A second hysteresis loop is measured to remove the training effect.
4. In the presence of a saturating applied field which opposes H_{EX}, the sample is heated to a thermal activation temperature, T_{ACT} for 30 minutes.
5. The sample is always cooled down to T_{NA} before hysteresis loop measurements are recorded.

Steps 4 and 5 are iterated with a constantly increasing value of T_{ACT} until the hysteresis loop shift switches from the initial value to the opposite sign final value passing through a point where the exchange bias is zero which corresponds to the blocking temperature, T_B of the AF material as shown in Figure 6.11.

The measurement procedure is derived from the York Model of exchange bias which describes the exchange coupling between polycrystalline AF and F thin films. The granular systems have a distribution of grain sizes as shown in Figure 6.11 where

only the portion between the critical grain volumes V_C and V_{set} contributes to magnetic pinning via exchange bias as discussed in Chapter 5.

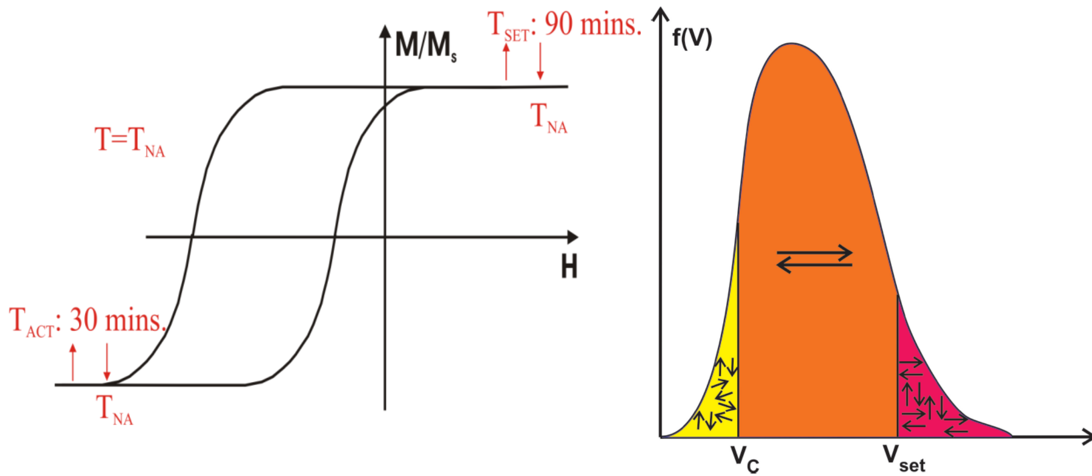

Figure 6.11. Schematic diagram of measurement steps of the York Protocol and representation of the grain size distribution function [83].

As T_{ACT} is increased, more AF grain will reverse leading to the point where equal number of grains are pinning the neighbouring F layer in opposite directions and the exchange bias vanishes. From the blocking temperature curve shown in Figure 6.12, the antiferromagnetic anisotropy constant K_{AF} is determined:

$$K_{AF}(< T_B >) = \frac{k_B < T_B > \ln(f_0 t_{SET})}{V_{med}} \tag{6.7}$$

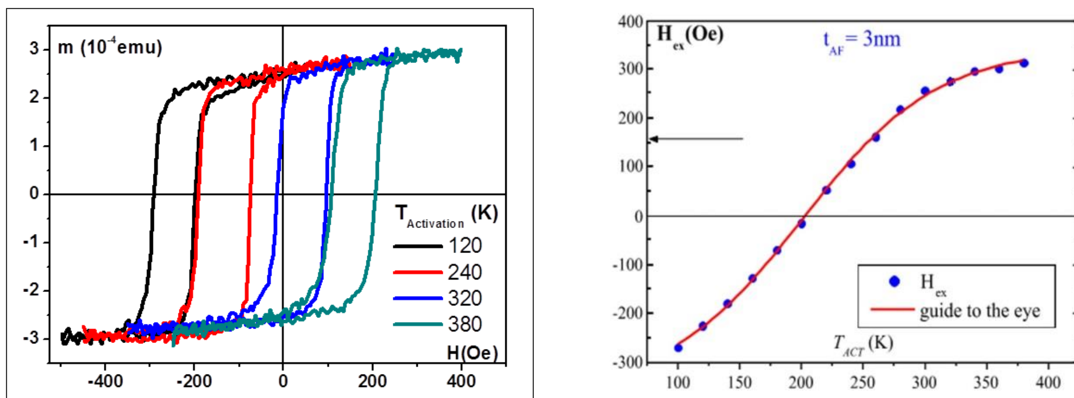

Figure 6.12: Hysteresis loops and blocking temperature graph used for determining K_{AF}.

7 Structural and Chemical Characterisation

The magnetic properties depend strongly on the crystallographic structure of alloys and compounds. Considering that most binary and ternary alloys have more than one allotropic state, structural characterisation is required in order to assess the phase formation and deposition and annealing conditions required for crystallisation. Structural studies are also beneficial when trying to understand the effects of sputtering parameters on the as-deposited state of a thin film. With magnetocrystalline anisotropy playing a significant role in the magnetisation process together with the distribution of grain sizes and orientations in granular systems, crystallographic studies are required in order to characterise and understand the magnetic response of the materials studied.

7.1 X-Ray Diffraction

X-ray diffraction (XRD) uses the Bragg condition for constructive interference in order to assess the degree of crystallisation and relative orientation of crystalline planes within a single element or alloy thin film. In order to observe the effect, the first requirement is for the incident radiation to have a suitable wavelength so diffraction onto atomic planes can occur. As the interplanar distances corresponding to various crystalline structures can vary drastically, a suitable wavelength of 0.154 nm was chosen and corresponds to the Copper (Cu) $K\alpha_1$ X-rays. The diffractometer used for the study is a Rigaku SmartLab equipped with a 9 kW radiation source and a Tungsten (W) filament.

$$n\lambda = 2d_x sin\theta \tag{7.1}$$

where n is a positive integer, λ is the wavelength of the incident wave, θ is the scattering angle and d_x is the interplanar spacing.

Compared to electron diffraction, XRD has some advantages due to the non-destructive character of the measurement and the samples do not require special preparation process. XRD can be performed in different external conditions with temperature controlled or compressive stages. The averaging capability is high as the incident beam can measure up to 20 mm laterally and depth profile studies are performed by modulating the incident beam angle [156].

There are two main geometries for diffraction measurements depending on the orientation of the crystalline planes relative to the surface of the substrate. The crystalline planes can be stacked parallel to the substrate along the *z* axis (growth direction) or perpendicular to the growth direction or substrate surface. The agreed nomenclature for the measurements arises from the direction of the incident radiation used to probe the atomic arrangement and therefore, “out of plane” measurements require large incident angles and the “in plane” measurements require very low incident angles probing crystalline planes perpendicular to the substrate surface as shown in Figure 7.1.

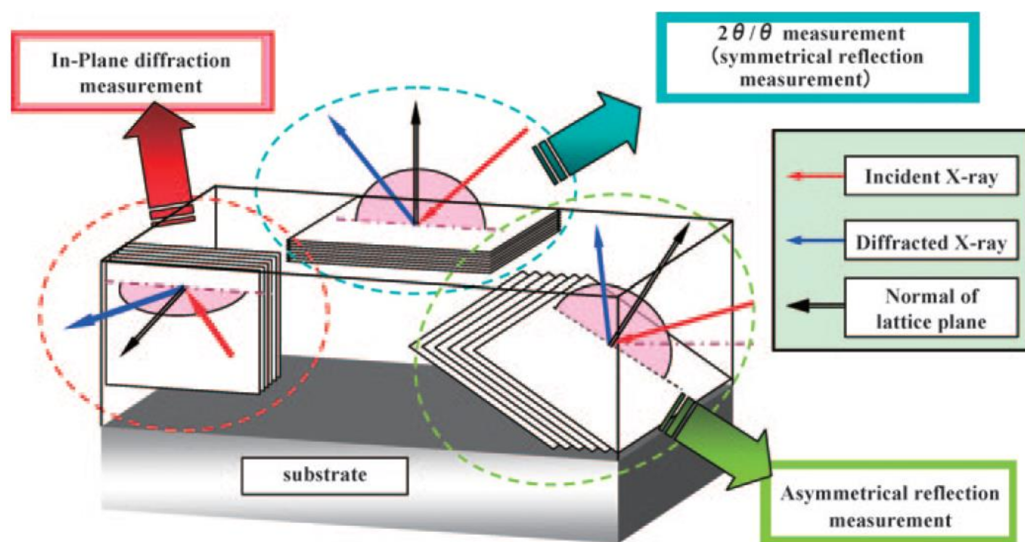

Figure 7.1: Schematic diagram of out of plane and in plane X-ray diffraction measurements [156].

The out of plane and in plane measurements are also called θ-2θ scans according to the degree of freedom of the X-ray generator, detector and sample stage used in the measurement.

The geometry of the system is very important in determining crystalline habits in a thin film. A parallel incident beam is more suitable for film structures while a converged geometry is used for powder samples. A double or quadruple reflection also called 2 bounce or 4 bounce single crystal Ge(220) or (440) monochromator can be used to suppress secondary radiations as Cu $K\alpha_2$, $K\beta$ and W for high resolution scans. $K\beta$ filters are also available and consist of a thin Nickel foil. The intensity of

the incident radiation drops by one or two orders of magnitude when using the monochromator but the spatial resolution of the measurement can increase by the same amount [157]. High resolution scans are required for highly crystalline or single crystal films when the diffraction peaks are either very close together or overlapping. In the case of epitaxial or highly textured polycrystalline films, high resolution scans are required in order to assess a very narrow distribution of crystalline plane directions using a rocking curve measurement or ω scan as seen in Figure 7.2.

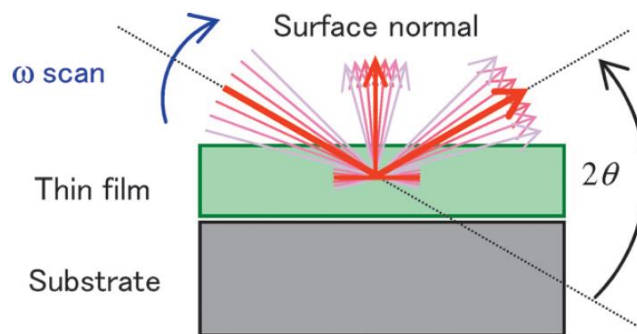

Figure 7.2: Schematic diagram of a rocking curve measurement[157].

The geometry of a rocking curve scan implies keeping the incident beam, θ and diffracted beam angles, 2θ the same while moving the sample orientation plane. If the sample stage is fixed, both the X-ray source and detector will move simultaneously changing the angle of the normal direction in the reflection. This measurement is used in estimating the distribution of crystalline orientation axis via the full with at half maximum (FWHM) of the diffraction peak broadening. As the measurement needs to be accurate to at least 0.1° or below, a suitable combination of source and a detector (analyser) is used. The resolution of the scintillation one dimensional detector (1D detector) is 0.01° but the available optics can limit the resolution of the scan to 0.5° when the monochromator is not used [158].

All the considerations made for the out of plane measurements also apply to in plane geometry. Some of the advantages of the low incident angle planar geometry are the diffraction arising from atomic planes perpendicular to the sample plane normal. Also a better signal can be acquired from ultra-thin films due to the increased interaction volume at grazing incidence. The low angle suppresses the background signal and substrate reflections. Using the incident beam angle modulation, a depth

profile study can be conducted on a multilayer structure. The penetration depth of an incident X-ray beam as a function of the incident angle can be estimated using:

$$t_x = \frac{4.61}{2\mu_x} sin\theta \tag{7.2}$$

where t_x is the penetration depth, θ is the incident beam angle and μ_x is the linear absorption coefficient of X-rays. According to the established nomenclature, the geometry is also called a $2\theta_\chi$ or $2\theta\chi/\varphi$ according to the degrees of freedom of the detector and sample stage where χ is the in plane rotation angle of the detector (2θ) and φ is the in plane rotation angle of the sample [159].

A direct application of in plane scans can be found in the pole figure measurement. So far, out of plane and in plane measurements were discussed and the outcome of the scans can reveal some information about preferred crystal orientations at 90° orientation: parallel and perpendicular to the substrate surface normal. The pole figure scan allows for the analysis of textural information averaged over a large area up to 20 mm^2 and under different external conditions as per requirements. The pole figure scans for the texture of a certain reflection by keeping the diffraction angle constant, tilting step by step in the 0-90° (α) interval and rotating the sample (β) [160].

A variation of the pole figure measurement is the in plane pole figure scan which performs the measurement using the in plane arm and a combination of source and detector positions to compensate for the tilting motion of the sample in the out of plane geometry. The method has some spatial constraints and reflections can only be detected for in plane angles of up to 90° [160]. However the sample does not require any fixing to the stage. The pole figure scan generates a 2D map of the scattering vector K_x in the polar coordinates: α and β as seen in Figure 7.3. If the polar plot has a central maximum and at least one ring, a fibre texture is identified. If the graph displays

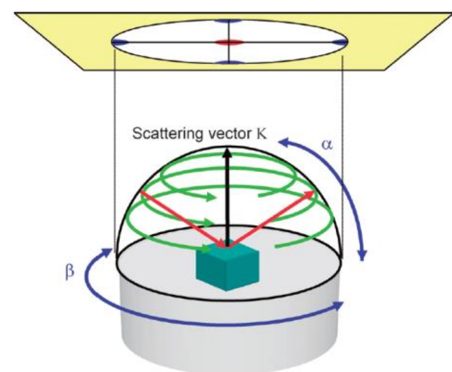

Figure 7.3: Schematic representation of in plane pole figure scan [160].

spots, the film is a single crystal. The values of the tilting angle α and rotation angle β determine the relative position of the preferential growth to the normal direction.

7.1.1 Scherrer Analysis

The samples studied in this work were mostly polycrystalline and therefore require careful analysis as the diffraction patterns usually contain broad peaks. The interpretation of the results is also difficult due to the coexistence of amorphous, highly textured polycrystalline layers and single crystal substrates.

As the majority of the materials used for data storage and volatile memories are not single crystals, defects such as lattice dislocations, lack of periodicity within the granular structure and stress/strain affect the quality of the diffraction measurements. A granular system can be considered a mosaic of small single crystal regions with different orientations which contribute to the Bragg reflection as shown in Figure 7.4. Kinematical diffraction theory is used to study imperfect or dispersed systems[161].

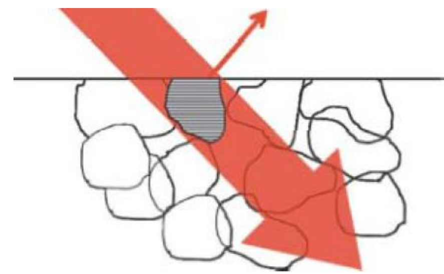

Figure 7.4: Representation of kinematical diffraction on a polycrystalline thin film [158].

Diffraction peak broadening arising from small grains is described by the Scherrer equation [161]:

$$D = \frac{C\lambda}{FWHM\ cos\theta} \tag{7.3}$$

where D is the particle or grain diameter, λ is the wavelength of the radiation, θ is the angle of the Bragg reflection and C is a constant close to unity.

The value of the constant C arises from mathematical considerations in deriving the equation and has a value of 0.94 [161]. Even if the equation is derived for a system containing cubic crystallites and the Gaussian function is used for fitting the diffraction peaks, the results reported for different crystalline symmetries and peak profiles show <10% error when comparing the X-ray diffraction measurement with

grain/particle size analysis [162, 163]. Due to the inverse proportionality between the lateral grain size and the cosine of the diffraction angle, a more pronounced broadening effect will arise at high angles.

When using the Scherrer equation, the instrumental diffraction peak broadening needs to be considered and it can fluctuate depending on the optics and filters used in the experiment.

7.2 Energy Dispersive Spectroscopy (EDS)

The ability to monitor stoichiometry within multiple element alloys is important when depositing Heusler or other alloys or compounds. A given alloy can have multiple crystalline phases according to the relative element composition therefore off-stoichiometric alloys can exhibit different magnetic characteristics. Controlling the composition is also beneficial when doping is required in order to improve existing properties such as pinning strength in the case of AF materials [139]. Fine control of the element composition within magnetic alloys is also required when theoretically predicted ground states of Heusler compounds are of interest for experimental studies.

As described in Section 6.1.2, the HiTUS deposition system is not able to perform co-deposition, therefore the composition of the target dictates the stoichiometry of the thin film unless doping occurs. Due to the demand for fast screening of the thin film compositions and also surface target composition, energy dispersive spectroscopy (EDS) was chosen for this study. The measurements were performed mainly in a scanning electron microscope (SEM): FEI Sirion S-FEG but also in transmission electron microscopes (TEM).

In order to understand the conditions and limitations of the compositional analysis, a brief description of the SEM is required. As shown in Figure 7.5, a scanning electron microscope has a defined architecture and components: an electron gun with controlled acceleration voltage, a series of electromagnetic lenses, deflectors and apertures designed to focus, collimate and control the position of the electron beam, the sample space and various detectors designed either for imaging or spectroscopy. This study is using the resulting X-rays from the interaction of the electron beam

with the bulk or thin film samples and therefore it is also called energy dispersive X-ray spectroscopy (EDX) [164].

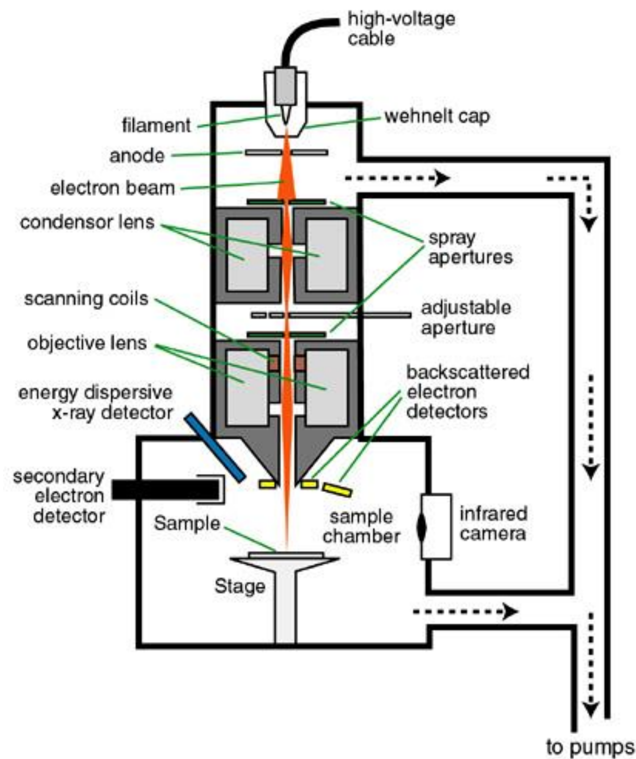

Figure 7.5: Schematic diagram of SEM [165].

The generation of X-rays for EDX arises from the interaction of highly energetic electrons with the sample. The mechanism is identical with the one used in the XRD source described however in this case, the generation of monochromatic radiation by irradiating a copper target (anode) is replaced by identifying different chemical elements which emit specific X-ray energies. Two basic types of X-rays are produced with the inelastic interaction between electrons and specimen: characteristic and background radiation. Characteristic X-rays arise from the ejection of an inner electronic shell (*e.g.* K shell) of a certain atom. The hole created by the interaction is then filled by an electron from an outer shell and the remaining energy is released to an X-ray quantum. The energy of the characteristic radiation depends on the atomic number as indicated by Moseley's law:

$$E_x = C_1(Z - C_2)^2 \tag{7.4}$$

where E_x is the energy of a given X-ray emission line, Z is the atomic number of the emitting element and C_1 and C_2 are constants. If the energy released is transferred within the electronic shells, an Auger electron is then ejected from the atom. The Auger electrons have low energy between 50 and 2500 eV and a mean free path of up to 2 nm [164]. Secondary and back scattered electrons are also emitted from the interaction as shown in Figure 7.6.

The continuum radiation or "bremsstrahlung" is the background signal and originates from the electron interacting with the atomic nucleus.

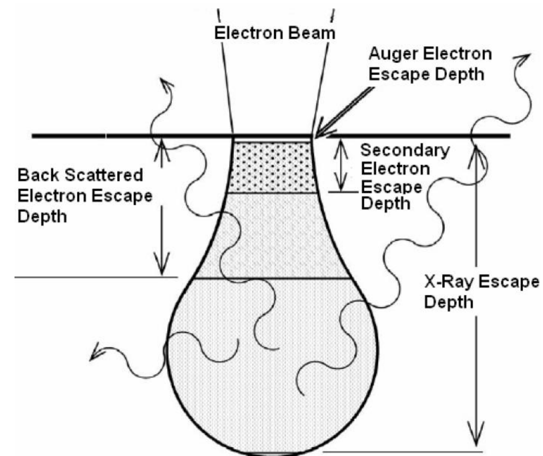

Figure 7.6: Schematic representation of the electron beam interaction in SEM [164].

The name of characteristic X-rays coincide with the electron shell in which the initial vacancy occurred and as with the XRD, due to the coexistence of electrons within multiple bonded orbitals, the $K\alpha$ radiation includes components of $K\alpha_1$ and $K\alpha_2$ X-rays with very close energies and they cannot be resolved with the EDX detector. Due to the high probability of electron transition from adjacent shells (L to K), the $K\alpha$ radiation will be an order of magnitude more intense than the $K\beta$ line although the latter transition will result in a higher energy quantum [164]. The excitation energy required for ionisation is marginally larger than the X-ray emission line and it is also called critical ionisation energy. A 1.5 to 3 times higher energy is used in practice in order to guarantee the X-ray emission. An "overvoltage" is necessary in order to improve the peak to background signal ratio which should be around 4000 counts or higher [164].

The EDX elemental analysis is somewhat limited in precision due to the large interaction volume of the electron beam and specimen in the SEM. Although the spatial resolution is not of interest for this study, the microscope operates to a micron rather than a nanometre precision scale and the spectroscopy data is only accurate to about 10% of the weight for specific elements. In order to minimise the errors of the measurement, a 2 nm Ru or Ta capping layer was used and the thickness of the

Heusler alloys was 100 nm. The data was also corrected using the Stratagem software package and calibrated using the results from chemical analysis performed by InterTek Ltd with a precision of one part per million (ppm).

7.3 Transmission Electron Microscopy (TEM)

Structural studies are of great importance in developing an understanding of the crystallisation process of alloys, different phase formation and the relationship between the growth processes and outcome. Thin film growth often relies on a number of techniques in order to obtain a certain alloy or compound. Moreover, the growth parameters are extensively used for inducing specific properties for the thin films such as magnetisation or transport characteristics. Due to the complexity of the thin film stacks which are required for spintronic applications; a suitable method of observation is required which is able to resolve structural characteristics at an atomic level.

Optical microscopes have been extensively developed and have reached resolutions within the micron scale but fundamentally, the performance of such microscopes is limited by the wavelength of the illuminating radiation as described by the Rayleigh criterion which gives the limit of the resolving power [166]:

$$\delta_{min} = \frac{0.61\lambda}{NA} \quad (7.5)$$

where δ_{min} is the smallest distance that can be resolved, λ is the wavelength of the incident radiation and NA is the numerical aperture of an optical system which can be considered for a single objective lens: $NA = n_r \, sin\Theta$ where n_r is the refractive index of the medium and Θ is the semi-angle of collection corresponding to the lens. With the current constraints, the resolution of an optical device is around the 200 nm limit and not sufficient for the required observation of structural characteristics in alloys or compounds.

The necessity for a controllable and suitable wavelength radiation beam together with the discovery of the wave-particle duality of electrons led to the development of the electron microscope [166]. The transmission electron microscope uses high energy electrons in the 100-300 keV range which are generated by an

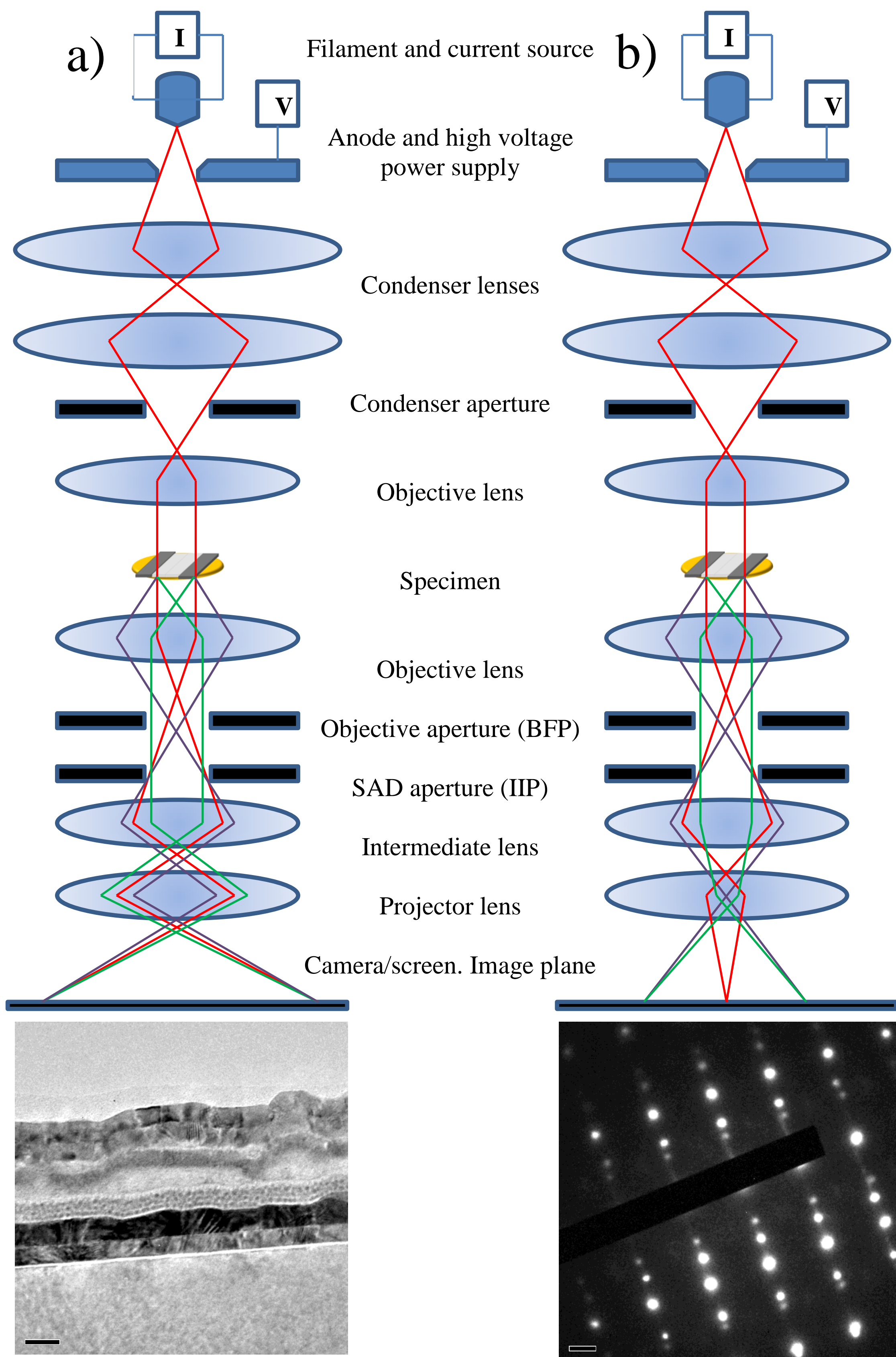

Figure 7.7: a) Schematic diagram of bright field (BF) TEM operation with image. b) Schematic diagram of diffraction mode operation with a diffraction pattern.

electron gun using either a thermoionic or field emission process [166]. The electrons go through an acceleration process where a high voltage is applied resulting in a radiation which for a typical 200 keV machine has a wavelength of 0.00251 nm.

With a short enough wavelength, the electron beam has another major advantage which is the interaction with a magnetic field given by the resulting Lorentz force used as the basis for manufacturing electron optics. As shown in Figure 7.7, a transmission electron microscope consists of a gun assembly, a series of apertures, electromagnetic lenses and a detector (camera) which acquires the image. The TEM can perform imaging and diffraction using two optical configurations given by the strength of the intermediate lens [166].

Diffraction patterns can be acquired to check for the crystalline structure of the specimens. The lattice constants of the observed structures can be estimated by measuring the distance between the central diffraction spot to the desired reflection. As the measurement is performed using an intensity histogram derived from the image, the precision of the measurement of the distance is around 0.2 nm. Using the equation:

$$d = \frac{\lambda_e \, L_c \sqrt{h^2 + k^2 + l^2}}{R} \tag{7.6}$$

where d is the interplanar distance, λ_e is the wavelength of the electron, L_c is the camera (focal) length, (h, k, l) are the Miller indices corresponding to a reflection and R is the distance between the primary diffraction spot and the chosen reflection.

Images can be acquired using a bright field (BF) or dark field (DF) contrast in a TEM. The transition from one to the other implies restricting the beam passing through the specimen to one of the diffracted spots rather than collecting the entire signal from the incident beam as shown in Figure 7.8. This results in an inversion of the contrast of the image when compared to BF.

Similar to the scanning electron microscope (SEM), the interaction of the electron beam with the specimen results in elastic and inelastic scattering. The incoherent low angle elastically scattered electrons provide the mass thickness contrast observed in

high resolution bright field imaging while the inelastic scattering provides information used for spectroscopy measurements such as EDX or electron energy loss spectroscopy (EELS). The TEM is therefore able to provide chemical analysis of the specimens studied.

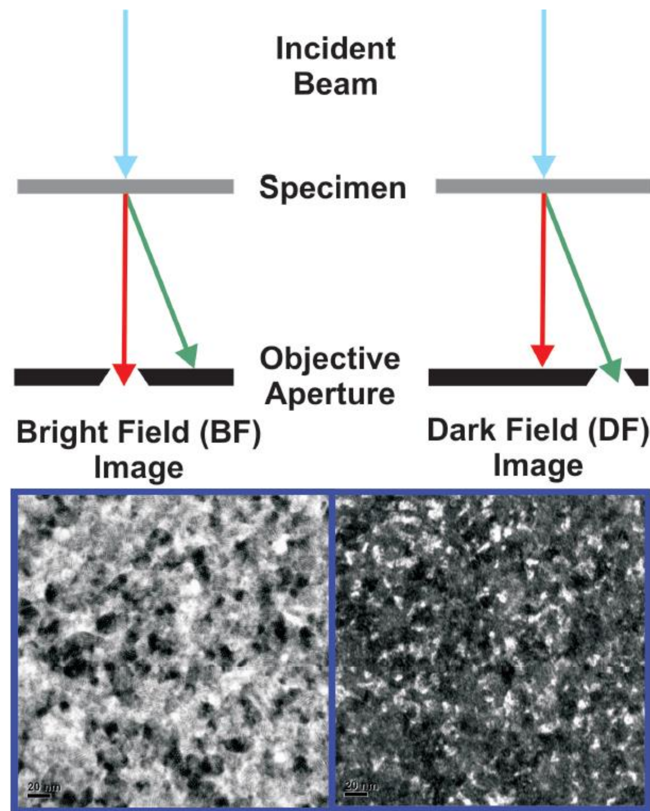

Figure 7.8: Bright field and dark field TEM images.

The resolution of an electron microscope is in theory higher than any interatomic distance however it is inherently limited by the imperfections in magnetic lenses also called aberrations. The defects arise from the non-uniformity of the magnetic field generated between the poles of an electron optical element but can be partially corrected using some additional multipole structures called aberration correctors (C_S correctors). Aberrations are accentuated by the instability of the power supplies and environmental factors surrounding the microscope: vibrations and thermal fluctuations. Ideally, the electron beam passing through the specimen needs to have a parallel geometry and constant phase in order to provide accurate interference contrast from the atomic planes. Two main types of aberrations can be identified: spherical and chromatic. As seen in Figure 7.9, the spherical aberration (C_3 or C_S) is a consequence of the radial non uniformity of the magnetic field within the lens.

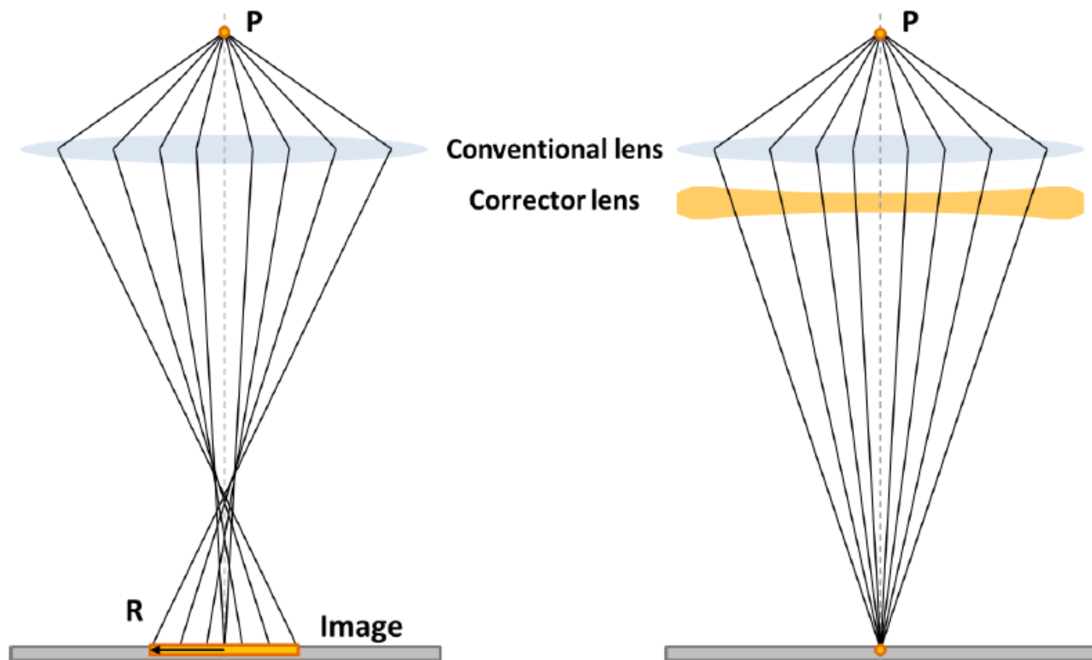

Figure 7.9: Schematic diagram of spherical aberration induced by a conventional electromagnetic lens and correction using a divergent multipole lens.

A large spread of electron energies will induce chromatic aberrations when passing through an optical element. This effect is not very important in the pre-specimen column region as the electron gun usually emits a small wavelength spectrum. The interaction with the specimen is more likely to spread the resulting beam energy due to the inelastic scattering events.

Another intrinsic imperfection of electron optics is astigmatism which leads to a distribution of focal lengths for the focusing system. This defect can be broken down into two-fold, three-fold and higher order (A_1, A_2, $A_{3...}$) geometries. The correction for astigmatism can be done manually for the two-fold geometry using an amorphous specimen such as the carbon film on a Cu grid.

Considering the imperfections which were described, the focal point of a perfect lens turns into a plane as the extremities of the lens act as regions of different convergence for monochromatic radiation. A similar situation is found for the wavelength distribution, chromatic aberrations and also for astigmatism. In the absence of an aberration corrector, small diameter apertures can be used to collimate the beam to the centre of the lens.

The objective lens is known to induce the most imperfections for the TEM. All aberrations are multiplied by the number of magnetic optical elements which is larger for the electron microscope due to the inexistence of a divergent magnetic lens which has to be replaced by a sum of two converging lenses [166].

7.3.1 Scanning Transmission Electron Microscope (STEM)

The scanning transmission electron microscope uses a small diameter beam as an electron probe which is scanned across the specimen in order to provide an image. The data is acquired on a pixel by pixel basis and one advantage of this technique is the possibility of controlling the position of the electron probe and therefore increased precision for chemical analysis (EDX) or diffraction measurements.

The resolution in STEM is limited only by the size of the probe which is determined by the condenser optics and characteristics of the electron gun. The addition of a set of scanning coils is required in order to control the position of the focused probe which is then passed through the objective lens and ultimately through the specimen as shown in Figure 7.10. The objective lens is therefore the most important piece of optics for STEM as it is for TEM operation.

An aberration corrector can be positioned before the specimen and allows for sharper focusing of the electron probe and increased intensity resulting in more defined contrast. The introduction of probe correctors allows for fine control of the probe diameter which can be less than 0.1 nm and therefore smaller than any interatomic distance [167]. The scanning geometry allows for all the optics to contribute only prior to the interaction with the sample which leaves room for greater flexibility in the imaging process. Low angle coherent scattered electrons are channelled towards a bright field (BF) detector while the incoherently high angle scattered electrons are collected using a High Angle Annular Dark Field (HAADF) detector. The HAADF detector is commonly used in STEM and gathers information which is highly sensitive to the atomic number. Combining this imaging technique with EELS results in an atomically resolved chemical map of the specimen. Due to the different and complementary shape of the detectors, they can be used simultaneously for imaging [168].

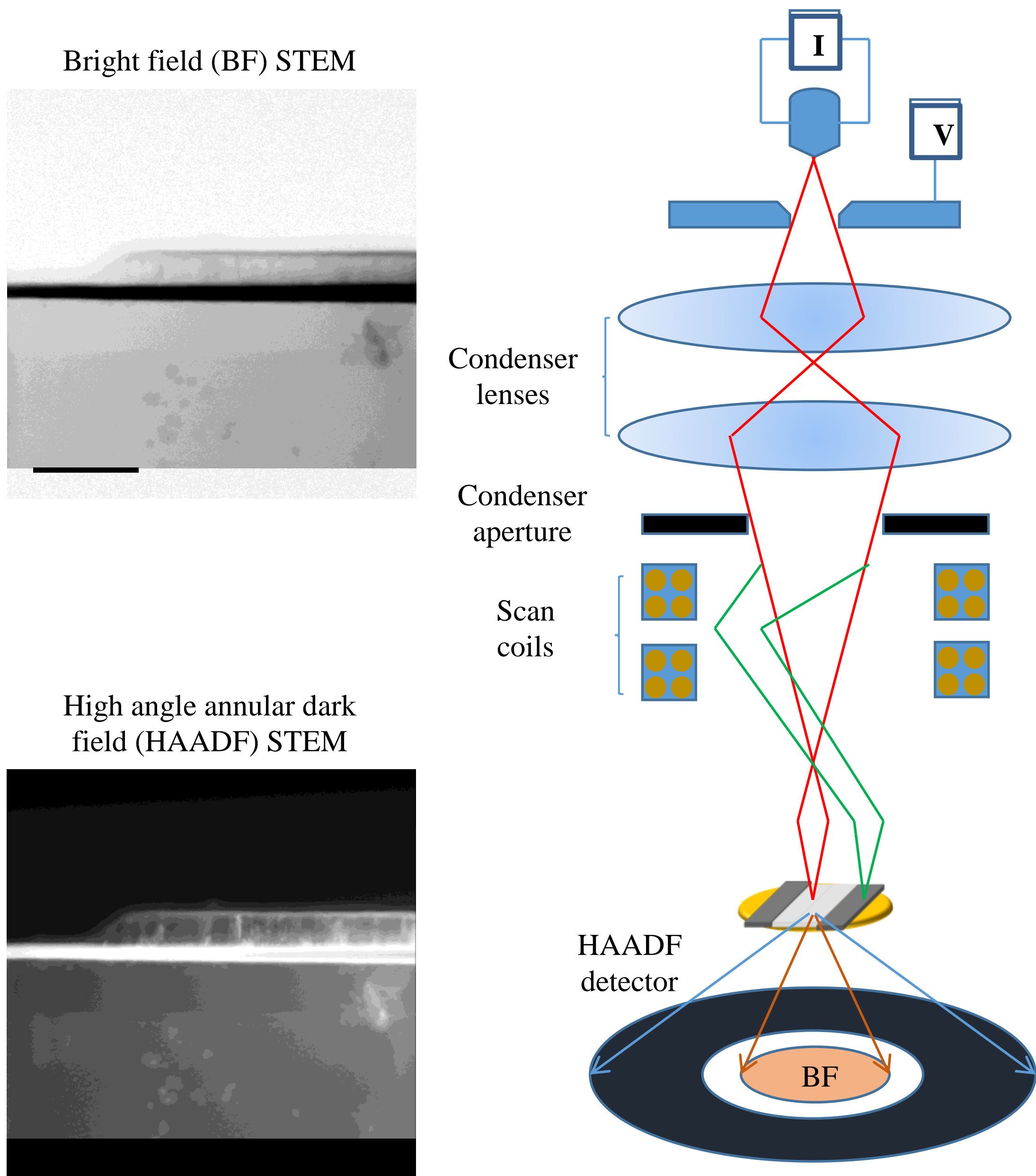

Figure 7.10: Schematic diagram of bright field (BF) and high angle annular dark field (HAADF) scanning tunnelling electron microscopy (STEM).

Transmission electron microscopes are necessary tools when detailed structural characterisation is required. With the addition of chemical analysis detectors and available atomic resolution, TEMs offer a complete package of structural measurements designed for nano and sub-nanometre features. Some of the disadvantages of electron microscopes include the high initial and maintenance cost of the equipment and surroundings, the limited sampling capability compared to an X-ray diffractometer but most importantly, the imaging intrinsic properties. The

TEM creates a two dimensional image as a projection of a 3D object which means that depending on the specimen, a sum of signals corresponding to a number of multilayers or differently oriented grains will be recorded. Careful sample preparation and analysis is required in order to single out the desired features.

7.3.2 Cross-sectional TEM

A specific technique is required for the characterisation of thin film multilayered structures in the electron microscope. Usually, the optimisation of thin film growth requires information about the thickness of the desired layer, roughness of the film and crystalline quality of the different alloys or compounds. For the epitaxial systems, the relation between the substrate and film structures may induce lattice matched growth. Strain or stress and resulting defects may also be induced during the deposition of thin film structures. For the polycrystalline films, the shape and size of the grains may be of interest together with the influence of any seed or buffer layers. For every stacked nano-system, the composition and intermixing of different layers has to be closely monitored.

A "top view" of a complex structure deposited on a conventional TEM grid will result in an addition of components with a strong bias towards the most crystalline layer. The inability to distinguish between signals leads to the preparation of a "side view" specimen where both the substrate and thin films are electron transparent and all the interfaces are clearly visible.

The most commonly used technique for cross sectional specimen preparation is the manual grinding and ion polishing method. Two pieces of sample are cut on a desired crystallographic axis of the substrate and glued together with the films facing each other. Two pieces of single crystal Si are added to each side of the structure in order to provide structural support. The Si piece also plays the role of a thickness marker for the advanced stage of grinding as Si becomes light transparent below the thickness of 50 μm. This is a key element for the preparation of samples deposited on light transparent substrates as sapphire or MgO. The samples are polished using a series of diamond lapping pads with different grit sizes ranging between 15 and 1 μm.

A Gatan precision ion polishing system (PIPS) is used for the last stage of sample preparation. Two focused argon ion guns thin down the middle region of the specimen at low angles (6-10°) until it becomes electron transparent at <100 nm as shown in Figure 7.11.

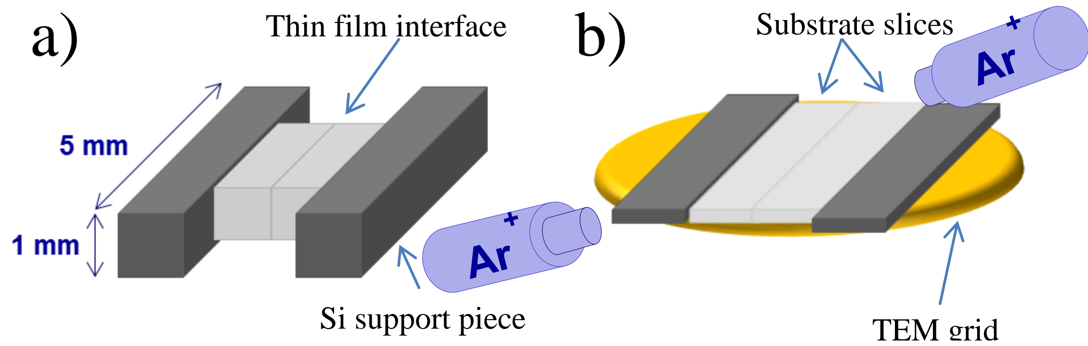

Figure 7.11: Schematic representation of a cross-sectional TEM a) specimen before thinning and b) during the ion polishing step.

Careful examination of the sample is required during the process as both the grinding and ion polishing steps can destroy the specimen or the area of interest which is the thin film interface. The precision polishing system mills both sides of the specimen using energetic Ar ions in order to remove excess material. The beam energy is then decreased to remove re-deposited material and smooth out the surface of the specimen which is required for high resolution (HR)-TEM/STEM analysis.

A focused ion beam (FIB) system can also be used for cross-sectional sample preparation. A scanning electron microscope (SEM) is used as the basis to which a micro-manipulator and a gallium ion gun are added. The ion gun can be used for cutting or material deposition depending on the energy of the beam (1 to 30 keV). The controlled deposition of material is made possible by the use of a liquid metal ion source (LMIS) which uses Ga as the process material due to properties such as low melting point and vapour pressure together with good conduction properties as shown in Figure 7.12 The ion beam is finely confined down to a spot size of around 5 nm and allows for fine mechanical control during the specimen preparation.

A heavy material *e.g.* gold or platinum is deposited on the surface of the sample in order to prevent ion beam damage to the thin film. The ion gun is then used to cut and shape a micron sized lamella which is separated and transferred onto a grid as shown in Figure 7.13. The specimen is attached to the manipulator and grid by using micron size welds made using LMIS. The sample is thinned down using the Ga ion gun to electron transparency. The FIB may also be used as a precision ion polishing system with low ion energy in order to remove any imperfections caused by the cutting and shaping process. A gentle mill or similar ion polishing step may be used in the final preparation.

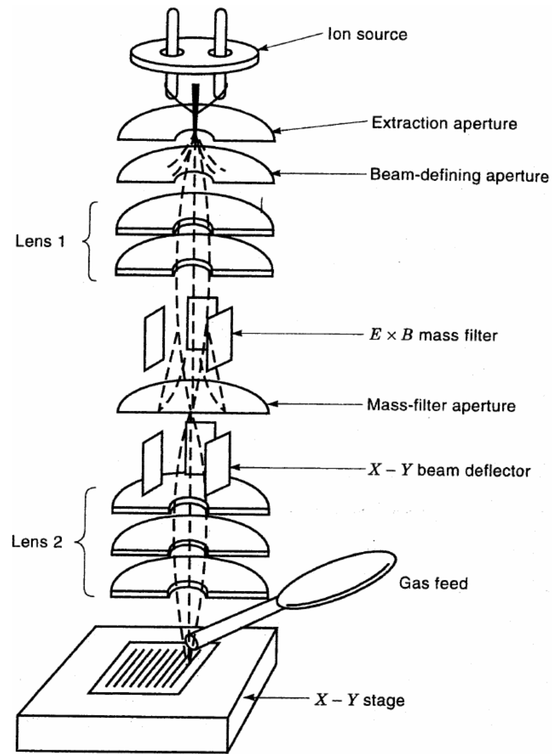

Figure 7.12: Schematic diagram of a liquid metal ion source (LMIS) in FIB [169].

Regardless of the process used for cross-sectional sample preparation, it is worth remembering that all the high energy interactions involved in the fabrication method may have an impact on the structure and chemical composition of the thin film specimen. A consequence of sustained high energy argon ion milling is the increase of specimen temperature which can cause phase transitions or intermixing in multilayer structures. A controlled temperature stage and low energy radiation can be used in order to minimise these effects. It is recommended that all the alloys or compounds undergoing preparation have stable crystalline phases. The fabrication method can be adapted for materials that are known to diffuse through multilayered structures.

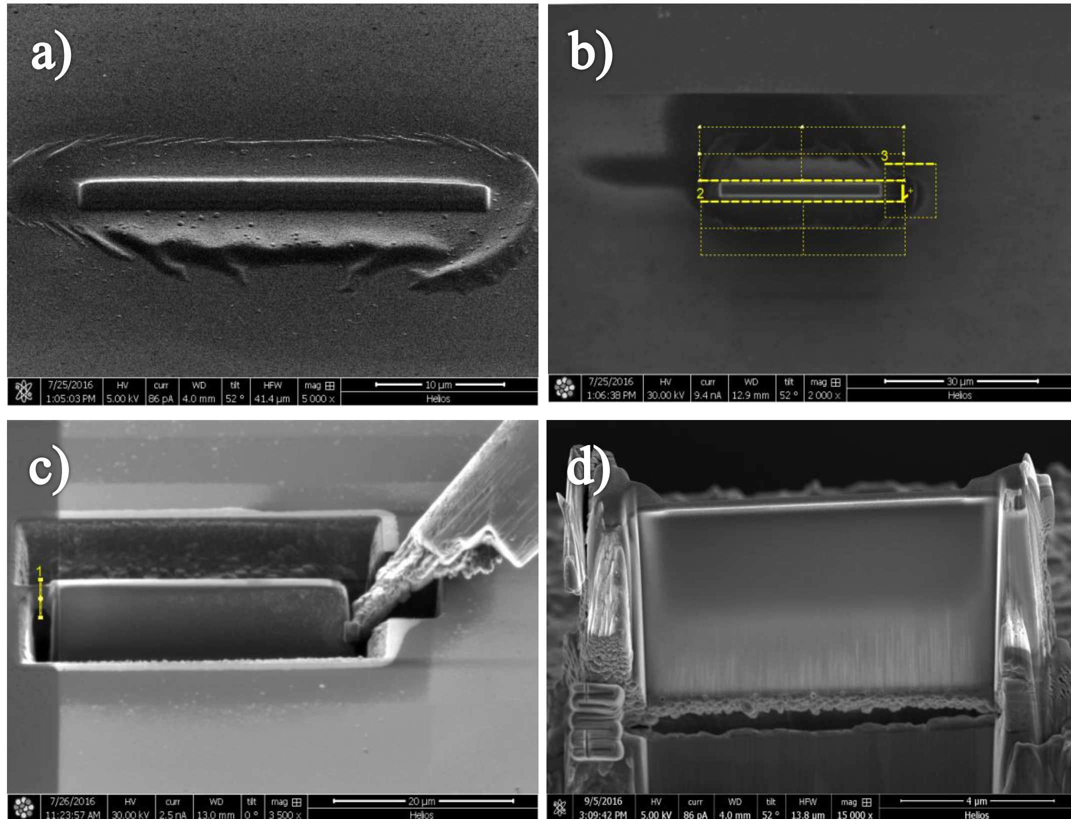

Figure 7.13: a) Strip of platinum deposited on top of the lamella. b) Cutting pattern set for the automatic FIB control. c) Separation of the lamella from the sample. d) End result after thinning the specimen.

For the imaging of a cross-sectional TEM specimen, the use of a double tilt holder is required. The tilting motion is used to align the chosen zone axis of the substrate with the direction of the electron beam. The fine alignment is done using the diffraction pattern obtained from the substrate which includes the set of Kikuchi lines. The centre of the line pattern is usually offset compared to the central diffraction spot. A simulation of an aligned (001) diffraction pattern from a single crystal MgO substrate is shown in Figure 7.14.

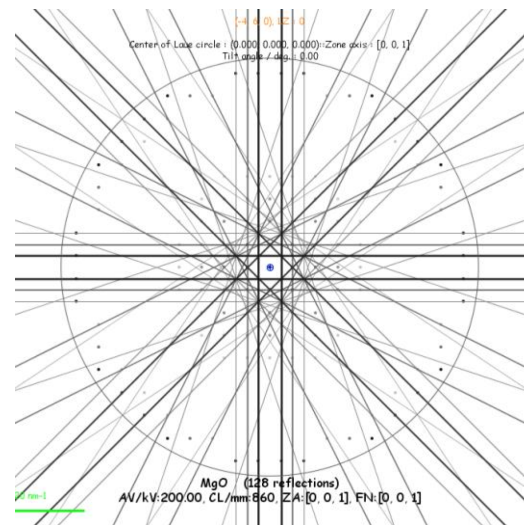

Figure 7.14: Diffraction pattern and Kikuchi lines corresponding to the MgO(001) zone axis.

8 Novel Antiferromagnets for Spintronic Devices

A suitable antiferromagnetic material which can be used in spintronic devices is required in order to replace IrMn. The search is focused on ternary Heusler alloys and compounds which were predicted or demonstrated experimentally to have stable AF ground state [21, 22, 58]. The following work presents the selection, synthesis and characterisation of alloys and compounds in the search for novel and cost effective antiferromagnetic materials.

8.1 Alloy Selection

The primary challenge when attempting to produce an antiferromagnetic material is choosing a number of suitable candidates which were shown or predicted to have the desired characteristics. For this work, full Heusler alloys (HA) were chosen as a starting point due to the large number of different compositions with tuneable magnetic properties and most importantly, the abundance of the elements forming the alloys.

As the lattice spacing and elemental composition have the most important role in determining the ground spin state in a unit cell, three Heusler alloys were initially selected for this study: Fe_2VAl, Ni_2MnAl and Cr_2MnSb as listed in Table 8.1.

Table 8.1: Properties of the selected Heusler alloys as reported in the literature.

Composition	Lattice constant (nm)	Neel Temperature (K)	Source
$Fe_{2.5}V_{0.5}Al$	0.576	Unknown	Theoretical calculation [58]
Ni_2MnAl	0.581 [170]	313 [170], 353 [60]	Theoretical calculation, MBE grown
Cr_2MnSb	0.620	342 [171]	Theoretical calculation

Fe_2VAl was predicted to have a metastable antiferromagnetic configuration [58] however it requires an off-stoichiometric elemental ratio and therefore precise control over the alloy composition is needed as discussed in Section 7.2.

Ni_2MnAl was shown and predicted to have an AF ground state and a Neel temperature of over 300 K which would be suitable for applications. Moreover, the alloy was also reported to have a stable AF phase experimentally when deposited in epitaxial form by MBE [21] as presented in Section 2.4.

The vast majority of Heusler alloys crystallise in a cubic structure and because of the symmetry of the atomic arrangement, the magnetocrystalline anisotropy is expected to be low. Doping and off-stoichiometric compositions may induce some level of distortion in the unit cell which could lead to an increase in anisotropy. The increased anisotropy leads to improved thermal stability of the magnetic pinning via exchange bias in applications such as in a HDD read head as discussed in Section 4.3.

Ideally, the new AF thin films should comply with industrial standards for deposition and device fabrication so post-annealing temperatures should be kept at values lower than 350°C. This is a specific requirement for the nanoelectronics industry and it is designed to minimise possible chemical decomposition or damage to the ultrathin magnetic films which stack up to create spin valves and magnetic tunnel junctions. The crystallisation process in Heusler alloys presents another challenge due to the degree of ordering of the unit cell. For full Heusler alloys with a X_2YZ generic structure, three different phases can be identified according to the degree of disorder of the atomic sites within the unit cell. The $L2_1$ phase is highly ordered and the atomic sites of the X, Y and Z elements are well defined and not interchangeable. The partially ordered *B*2 structure is characterised by the Y and Z elements randomly distributed on their atomic sites. The fully disordered *A*2 phase is characterised by the complete mixing of the X, Y and Z elements within the crystal lattice. It is predicted that the partially disordered *B*2 phase is antiferromagnetic for some alloys chosen as discussed in Section 4.3.

Measurements were conducted on a third Heusler alloy deposited by Bielefeld University: Ru_2MnGe. The ruthenium based alloy has to have a stable AF phase from theoretical calculations and experimental studies with a measured T_N of 353 K as discussed in Section 4.3.

A tetragonal structure compound was also studied in order to provide a reference for the cubic Heusler structures. MnN was reported to exhibit an AF ground state and has two tetragonal phases which are of interest for this work [172]. The work on MnN was conducted in collaboration with Bielefeld University.

8.2 Chemical Analysis of Polycrystalline Heusler Alloys

Due to the accuracy of the EDX data being no better than 5% it was considered unsuitable for this work. Therefore a set of calibration samples was analysed by InterTek Ltd for chemical composition analysis at ISO9001 standards. For the analysis Ni_2MnAl and Fe_2VAl samples were grown at a thickness of 100 nm on glass substrates at bias voltages of -300 V and -900 V. One of each sample was sent to InterTek and another from the same sputtering run was retained. This allowed for the EDX to be used as a comparator by measuring the spectra from the chemically analysed reference samples and comparing them to the samples being measured under the same beam conditions. At InterTek the samples were placed in separate sample tubes and digested using aqua regia (HCl: 15 ml, HNO_3: 5 ml), they were diluted to a final volume of 30 ml with demineralised water. Blank glass substrates were also analysed in the case of any unexpected contaminants being measured. The solutions were then analysed using inductively coupled plasma optical emission spectroscopy (ICP-OES).

Table 8.2: Results of the chemical analysis performed by InterTek.

Heusler Alloy X_2YZ	***Bias Voltage (V)***	***Composition (At ± 0.01%)***		
		X	***Y***	***Z***
Ni_2MnAl	***-900***	***53.32***	***26.29***	***22.17***
Ni_2MnAl	***-300***	***50.94***	***26.89***	***22.17***
Fe_2VAl	***-900***	***53.75***	***20.09***	***26.16***
Fe_2VAl	***-300***	***55.25***	***16.53***	***28.22***

8.3 Structural Characterisation of Polycrystalline Fe_2VAl

Fe_2VAl was deposited using the HiTUS system as described in Section 6.2. Si/SiO_2 substrates with dimensions of 16x16 mm^2 were used. During sputtering, the process gas (Ar) pressure was kept constant at 1.86 mTorr and the bias voltage (V_B) was varied from -300 to -1000V in order to control the sputtering rate and grain size of the material [145]. The thickness of the Heusler alloy film was kept constant at 100 nm for the initial crystallisation studies in order to provide an increased signal from X-ray diffraction measurements as discussed in Section 6.2. A capping layer of 2 to 5 nm of Ta or Al was used in order to prevent oxidation. The films were post-annealed in a vacuum furnace at a base pressure lower than $5x10^{-8}$ mTorr for up to 9 hours.

The 9 kW Rigaku SmartLab X-ray diffractometer described in Section 7.1 was used for the analysis of the crystalline quality of the thin films. Two main types of scans were used for the characterisation of the Heusler films: the out of plane (θ-2θ) scan and the in plane ($2\theta\chi/\varphi$).

As shown in Figure 8.1, Fe_2VAl crystallises at 500°C with the appearance of the characteristic (220) Heusler peak at 44.4°. The absence of the (200) peak at 31° indicates that the alloy structure probably crystallises in the fully disordered *A*2 rather than the partially ordered *B*2 phase. The intensity of the (200) reflection is expected to be less than 10% when compared to the (220) peak [32]. For polycrystalline thin films where the intensity of the diffraction peaks is diminished, the (200) reflection may not be visible.

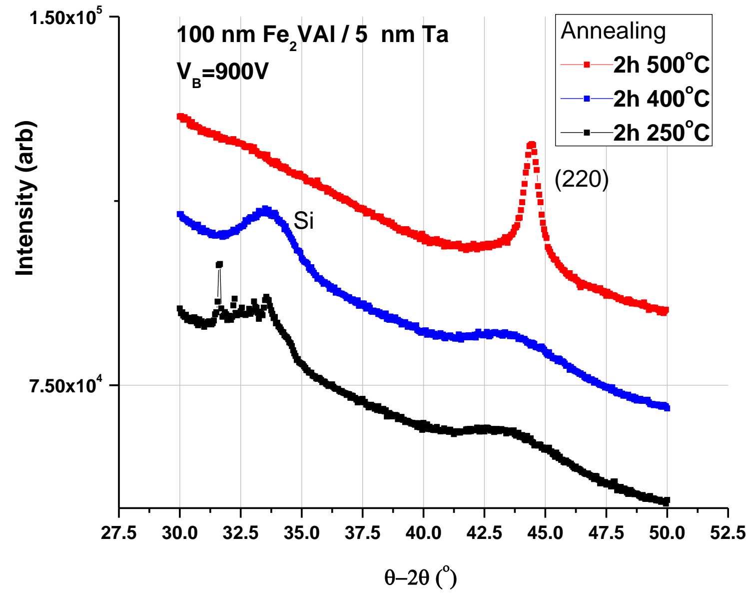

Figure 8.1: XRD spectra for Fe_2VAl annealed at elevating temperatures.

The broad diffraction peaks corresponding to Fe_2VAl in the as deposited state may originate from the DC sputtering process which is expected to produce a thin film with nanocrystalline texture and a grain size of less than 5 nm estimated by means of Scherrer analysis from the XRD pattern. The crystallisation threshold temperature found to be 500°C where the formation of (12±1) nm diameter grains is observed.

In order to quantify the XRD results, the following formula was used to calculate the quality (Q) factors for the optimisation of the deposition and annealing conditions as shown in Figure 8.2 and Table 8.2.

$$Q\ factor = \frac{Intensity(cps * \text{deg})}{FWHM(deg)} \tag{8.1}$$

The (220) Heusler peak was used throughout the experiment in order to quantify the degree of crystallisation after post annealing.

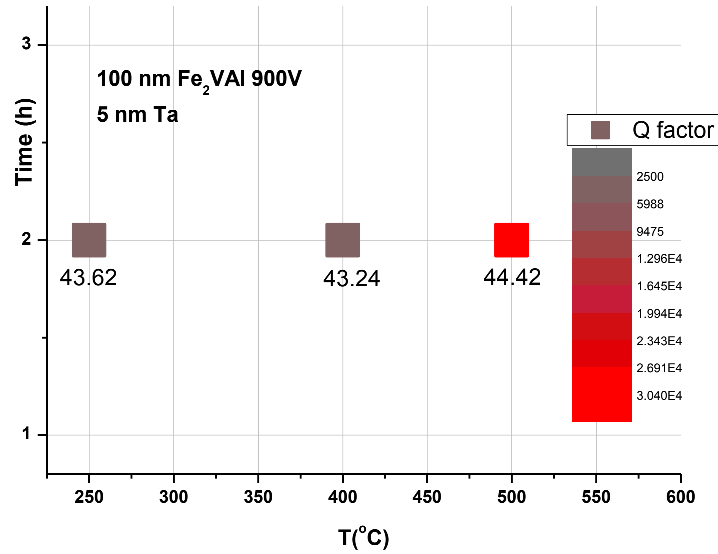

Figure 8.2: Q factor graph for Fe_2VAl annealed at elevating temperatures. The positions of the (220) Heusler peaks are recorded below data points.

Table 8.3: Q factor and lattice constant calculation for Fe_2VAl deposited at -900V and post-annealed.

Annealing		***Q***	***Lattice Constant (±0.01Å)***
Time (hours)	***Temperature (°C)***		
2	***250***	***2541***	***N/A***
2	***400***	***3855***	***N/A***
2	***500***	***30319***	***5.76***

As shown in Figure 8.2 and Table 8.3, the crystallisation of Fe_2VAl is subject to a threshold annealing temperature and for the films deposited at V_B =-900V, 500°C is the minimum temperature for the formation of the Heusler alloy phase.

The variation of the applied bias voltage on the target during sputtering affects the deposition rate and hence the grain size of the polycrystalline films. In the case of Fe_2VAl, crystallisation is observed in the as deposited state when a decreased

sputtering rate corresponding to a bias voltage of -300V is used. At V_B = -600V, crystallisation is not observed as shown in Figure 8.3.

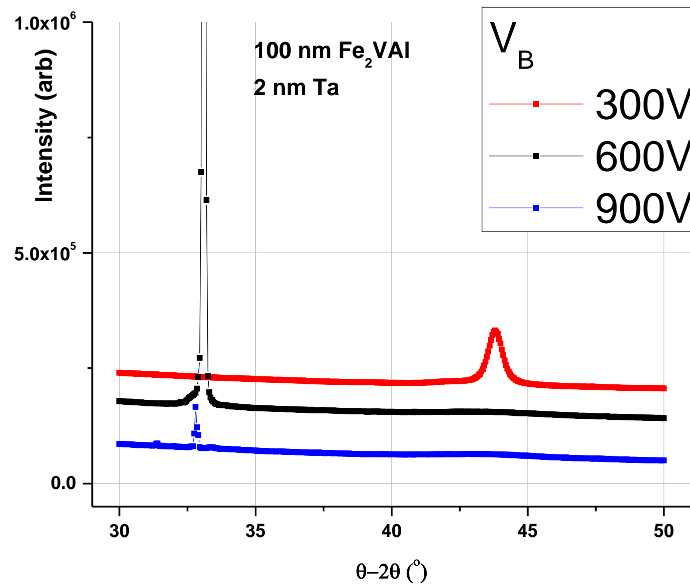

Figure 8.3: X-ray diffraction pattern of Fe_2VAl deposited increasing values of V_B.

As shown in Figure 8.4, both the (220) at 44.4° and (400) at 64° characteristic Heusler diffraction peaks are visible. The (111) superlattice reflection is not visible meaning that the alloy crystallises in the partially disordered *B*2 phase. Scherrer analysis was performed for the (220) Heusler peak resulting in an average grain size of (17.8 ± 0.7) nm. Decreasing the bias voltage from -900 to -300V resulted in the reduction of deposition rate from 0.06 to 0.03 nm/s and 50% increase of the average grain size. These changes can be the result of increased atomic mobility at the surface of the substrate and enough delay to facilitate layer by layer deposition kinetics [173].

Structural studies showed that Fe_2VAl crystallises in either the *A*2 or the desired *B*2 structure which are identified by the presence of the (110) and (100) family of reflections. The crystallisation temperature for the rapidly deposited alloy are high at 500°C while slow deposition results in a more ordered structure and larger grain size.

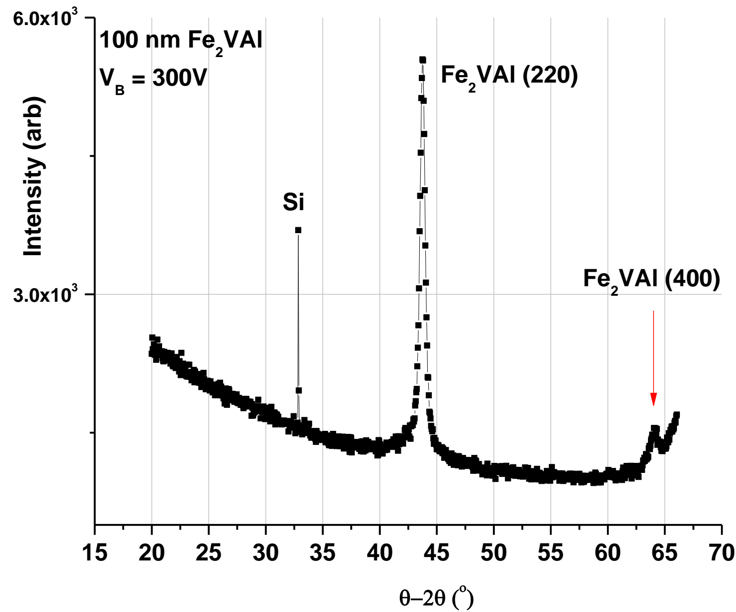

Figure 8.4: X-ray diffraction pattern of Fe_2VAl deposited at -300V.

8.4 Magnetic Characterisation of Polycrystalline Fe_2VAl

The Fe_2VAl thin films deposited on 5x5 mm^2 Si/SiO_2 substrates were measured using the Micromag 2900 AGFM described in Section 6.3.1. The measurements were performed at room temperature in the plane of the film. As seen in Figure 8.5, the Fe_2VAl thin film which was deposited at -900V and post annealed at 500°C shows a ferromagnetic hysteresis loop. The origin of ferromagnetism can be associated with the formation of a mixture of crystalline phases as discussed in Section 2.4 for Ni_2MnAl [21]. The partially disordered *B*2 phase may be combined with the highly ordered $L2_1$ structure which is expected to form a ferromagnetic structure.

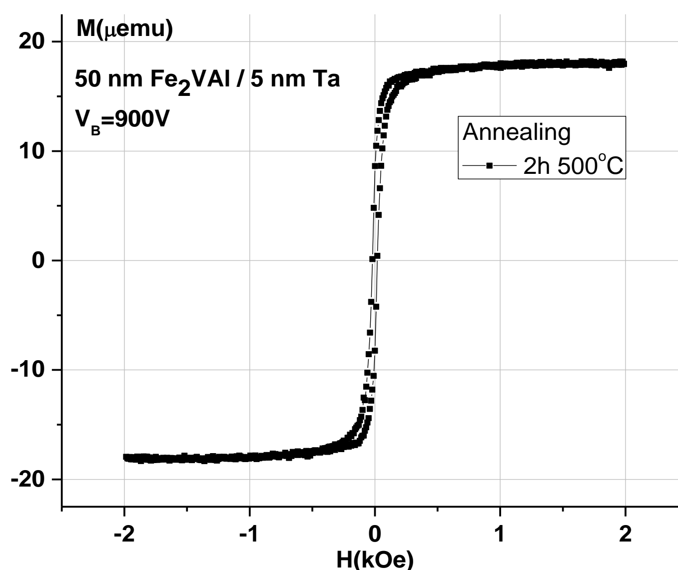

Figure 8.5: Hysteresis loop for the post annealed Fe_2VAl.

The films deposited using a decreased bias voltage of -300V show good initial crystallisation although as shown in Figure 8.5, Fe_2VAl exhibits weak ferromagnetism in the as deposited state. Post-annealing experiments confirm the tendency of the alloy to crystallise into a large grain ferromagnetic structure. With the increase of the annealing temperature, an increase by up to a factor 8 of the net magnetic moment is observed. The shape of the hysteresis loops confirms the transition from a small grain system where the reversal mechanism is driven by rotation of the magnetic moment in small grains to a dominating rapid domain wall movement process for the large grain crystalline films as shown in Figures 8.5 and 8.6.

The structural and magnetic studies conducted on Fe_2VAl show that the 2:1:1 stoichiometry of the alloy forms a ferromagnetic rather than the AF phase. Another study was conducted using the 3:1:1 target stoichiometry together with dopants in order to bring the composition of the thin films to the predicted AF 2.5:0.5:1. The precise elemental ratio is difficult to obtain but the overall trend of the experiment is the formation of the ferromagnetic phase of the Fe_2VAl Heusler alloy.

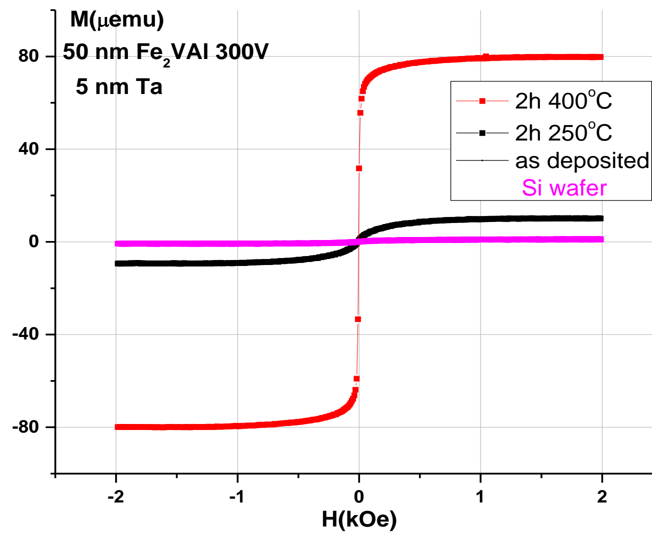

Figure 8.6: Hysteresis loops for post annealed Fe_2VAl deposited at -300V.

8.5 Structural Characterisation of Polycrystalline Ni_2MnAl

Ni_2MnAl was deposited using the HiTUS system in a similar manner used for Fe_2VAl. Structural characterisation using XRD was performed in order to determine the most suitable post-annealing conditions for the formation of partially disordered *B*2 Heusler phase to exhibit antiferromagnetism. As shown in Figure 8.7, the initial formation of the *A*2 fully disordered crystal structure is visible for the as deposited samples at both high deposition (V_B = -900V) and low deposition rate (V_B = -300V). The only characteristic Heusler reflection for the as deposited Ni_2MnAl is (220) and no (200) peak is observed. Using Scherrer analysis, the crystallite size for the as deposited Ni_2MnAl is estimated to be below 6 nm.

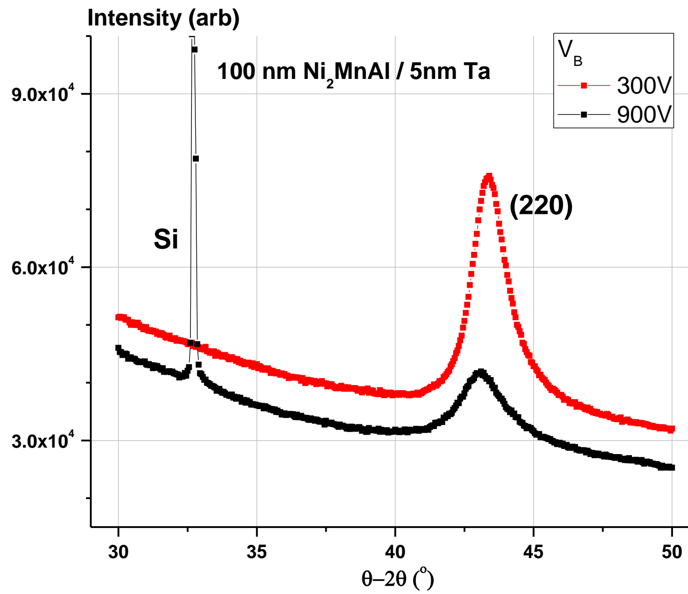

Figure 8.7: X-ray diffraction pattern for Ni_2MnAl deposited at V_B= -300 and -900V.

The as deposited crystalline structure of Ni_2MnAl does not satisfy the conditions for the *B*2 partially disordered antiferromagnetic phase formation. Post-annealing experiments have shown that the alloy crystallises at 400°C. This temperature exceeds the threshold set by industrial applications and therefore a set of seed layers were chosen in order to facilitate the *B*2 Ni_2MnAl phase formation at lower temperatures.

Previous work conducted by Sagar *et al.* [147] showed that using a lattice matched seed layer thin film improves the crystallisation of ferromagnetic Heusler alloys at low post-annealing temperatures. For Ni_2MnAl, chromium and silver were used as a buffer and seed layer respectively. A 3 nm thick Cr buffer layer is used to smooth out the surface of the substrate and prevent island growth of Ag. As shown in Figure 8.8, the optimum thickness of the Ag seed layer is 30 nm as reported for Co_2FeSi [147]. This is observed in the XRD pattern as the characteristic (220) Heusler reflection appears when the 30 nm thick Ag seed layer is used.

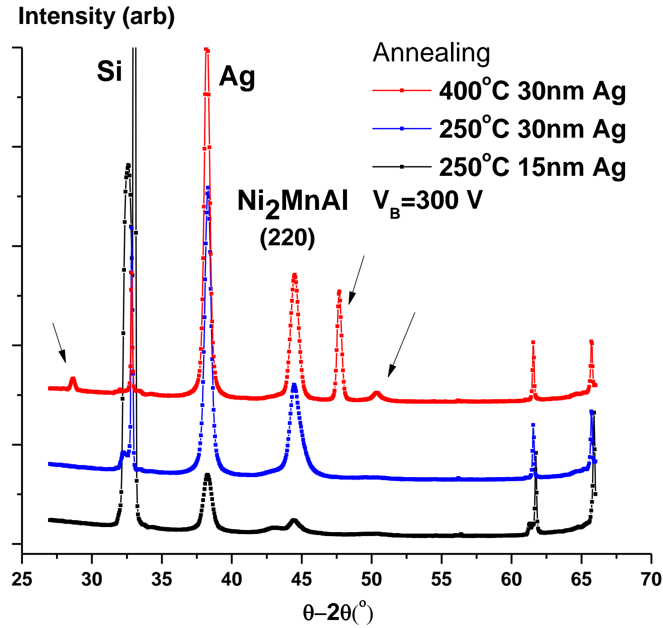

Figure 8.8: X-ray diffraction pattern of Ni_2MnAl deposited on Cr/Ag seed layers.

The XRD studies show that Ni_2MnAl crystallises at a temperature of 250°C when the Cr/Ag seed layers are used. Some formation of the Heusler structure is visible when using a seed layer which is 15 nm thick. Using Scherrer analysis, the grain size is estimated at less than 6 nm. When annealed at more than 250°C, the Ni_2MnAl Heusler alloy starts to segregate as shown by the sample annealed at 400°C where unknown secondary phase reflections are seen in the XRD profile (arrows in Figure 8.8). The grain size reaches a value of 9.5 nm when the 30 nm thick Ag seed layer is used and continues to increase for the sample annealed at 400°C where the median grain diameter is calculated at 13.4 nm.

As shown in Figure 8.9 and Table 8.4, the crystallisation of the *B*2 phase of Ni_2MnAl is subjected to a minimum thickness of the Ag seed layer used. This is observed by a sharp increase of the Q factor by a factor 20 corresponding to the characteristic Ni_2MnAl(220) reflection. A marginal decrease of the lattice constant is observed when increasing the annealing temperature to 400°C corresponding to the relaxation of the unit cell caused by the lattice mismatch with the Ag seed layer.

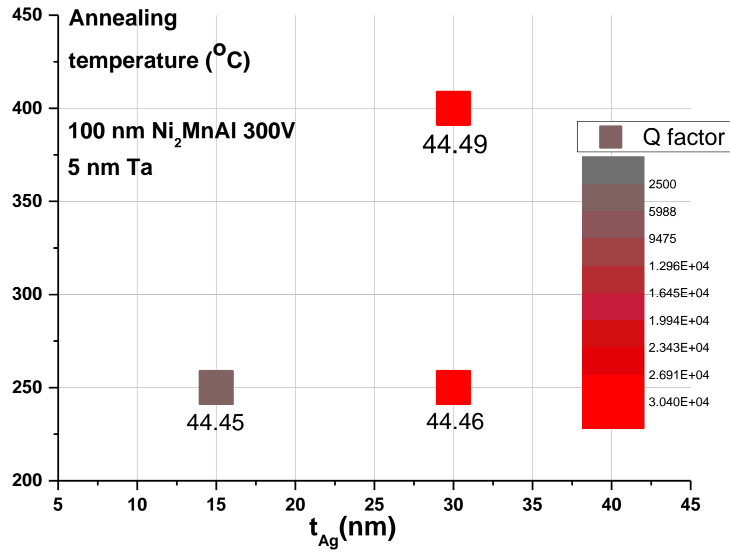

Figure 8.9: Q factor graph for Ni_2MnAl deposited on Cr/Ag seed layer. The positions of the (220) Heusler peaks are recorded below data points.

Table 8.4: Q factor and lattice constant calculation for Ni_2MnAl deposited at -300V on a Cr/Ag seed layer and post-annealed.

Thickness of Ag seed layer(nm)	***Annealing temperature(•C)***	***Q***	***Lattice Constant (±0.01Å)***
15	***250***	***2837***	***N/A***
30	***250***	***61524***	***5.79***
30	***400***	***68932***	***5.77***

The use of a lattice matched seed and buffer layer combination can decrease the crystallisation temperature of a Heusler alloys by as much as 50% as seen in the case of Ni_2MnAl. Optimisation of the thickness, deposition parameters and annealing conditions are needed in order to maximise the effects of lattice matched seed layers

8.6 Magnetic Characterisation of Polycrystalline Ni_2MnAl

The magnetic characterisation of Ni_2MnAl was performed using the Micromag 2900 AGFM and the ADE model 10 vector VSM described in Section 6.3.2. The thickness of the Heusler alloy thin films was decreased by a factor two or four compared to the structural characterisation samples. After the initial sample screening where a 100 nm thick layer of Ni_2MnAl was deposited on Si/SiO_2 substrates, multilayered structures were deposited in order to test the antiferromagnetic properties of the alloy. As discussed in the previous section, a combination of buffer and seed layer (Cr/Ag) is used in order to decrease the crystallisation temperature of the partially disordered *B*2 antiferromagnetic Heusler alloy phase. A thin ferromagnetic film (3 to 10 nm) was deposited on top of Ni_2MnAl for exchange bias (EB) measurements.

The ferromagnetic (F) materials chosen for the exchange bias measurements are $Co_{0.6}Fe_{0.4}$ and Co_2FeSi. The CoFe alloy is a commonly used high magnetisation ferromagnet which allows for decreasing the thickness of the thin film while keeping the values of the magnetisation detectable. Co_2FeSi is a well-known ferromagnetic Heusler alloy that was previously shown to couple well to AF materials such as IrMn [148]. Moreover, the ferromagnetic Heusler alloy allows in theory for lattice matched coupling between the AF and F thin films as they both have similar size unit cells.

The exchange bias samples were field set at 225°C for 90 minutes in a field of 10 kOe in order to achieve the saturation of the ferromagnet according to the York protocol discussed in Section 6.3.3. The samples were field cooled to 100 K in order to reduce thermal fluctuations in the low anisotropy antiferromagnetic cubic systems.

Figure 8.10 shows the result of field cooling for a 25 nm Ni_2MnAl/10 nm Co_2FeSi bilayer system when the Ni_2MnAl and F layer are deposited directly onto the substrate using a high deposition rate (V_B= -900V). The sample was measured for two states of crystallisation set via post-annealing.

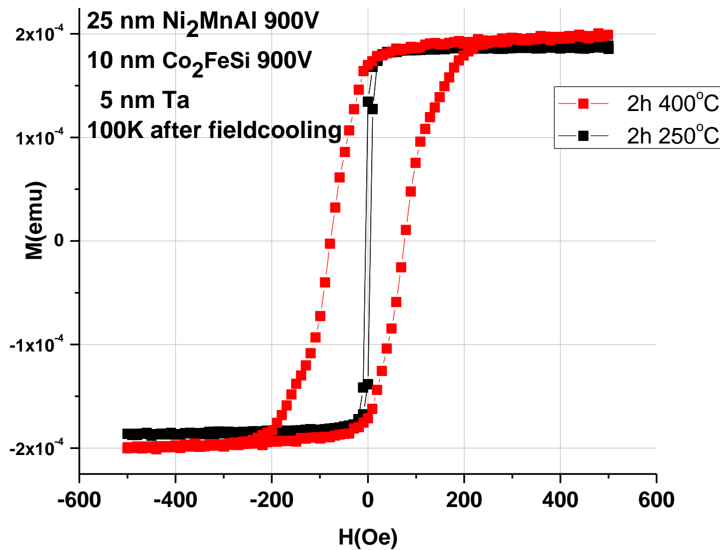

Figure 8.10: Hysteresis loop of the post-annealed Ni_2MnAl/Co_2FeSi bilayer.

As shown in Figure 8.10, no loop shift is visible but an increase in the coercive field (H_c) is observed. The increase in H_c coincides with the crystallisation point of the antiferromagnetic Ni_2MnAl and despite the null value of the exchange bias field, the coercivity increase may be a sign of low anisotropy AF coupling. The same trend is visible throughout the measurements and marked by a large increase of H_c when the ferromagnetic layer is replaced with CoFe as shown in Figure 8.11.

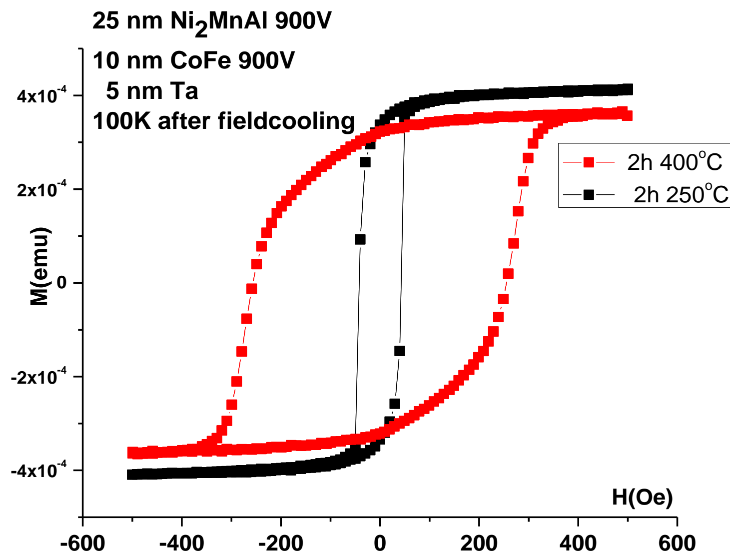

Figure 8.11: Hysteresis loop of the post-annealed Ni_2MnAl/CoFe bilayer.

The magnetisation reversal mechanism suffers some changes with the crystallisation of the partially disordered *B*2 antiferromagnetic phase of Ni_2MnAl. Both the CoFe and Co_2FeSi ferromagnetic layers exhibit quick magnetisation reversal via domain wall motion prior to coupling to the AF Heusler alloy. The weak anisotropic exchange interaction increases the torque required for the magnetisation switching by rotation of the magnetic moment in the granular films.

As the pinning strength of thin film antiferromagnetic materials is inversely proportional with the thickness of the neighbouring ferromagnetic layer, the thickness of the F layer was reduced to 3 nm. Thinner ferromagnetic layers can also be deposited but the overall magnetisation value may drop below the noise base of the magnetometer. Figure 8.12 shows the effect of decreasing the thickness of the ferromagnetic Co_2FeSi layer. When the ferromagnetic Heusler alloy is deposited on a similar Heusler structure, the magnetic anisotropy switches from the in plane to the out of plane direction. The change in anisotropy is observed for thin ferromagnetic Heusler alloys thin films and is usually attributed to strain induced by the interface with the underlayer.

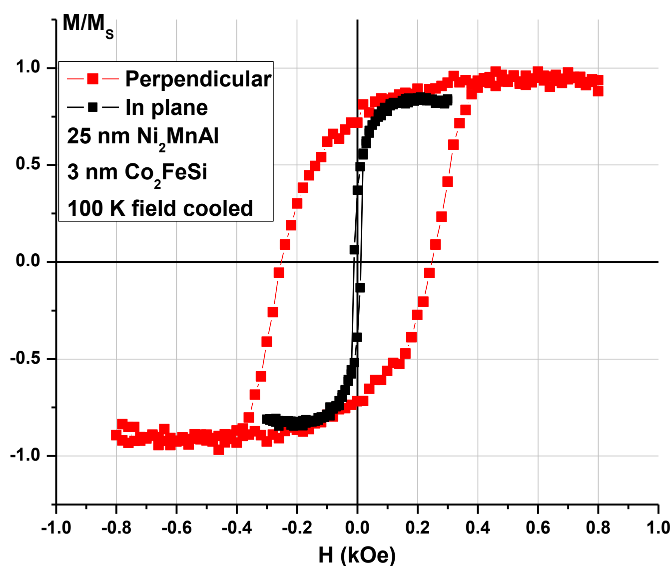

Figure 8.12: Hysteresis loop for the Ni_2MnAl/Co_2FeSi bilayer deposited on Cr/Ag seed layer and annealed at 250°C.

Similar to the in plane case, no loop shift is observed but the sudden large in the value of H_c is associated with the crystallisation of the AF Ni_2MnAl which may arise

from low anisotropic exchange coupling. The induced perpendicular anisotropy of the Co_2FeSi may be useful for current perpendicular to the plane (CPP) spin valves systems due to the intrinsic large spin polarisation properties of the ferromagnetic Heusler alloy. In an ideal case, a complete CPP GMR or TMR stack would be constructed using Heusler alloys exclusively. An epitaxial magnetic tunnel junction would allow for coherent electron tunnelling between the Heusler alloy layers hence increasing the TMR ratio.

8.7 Structural Characterisation of Epitaxial Ni_2MnAl

Figure 8.13 shows the simulated and indexed diffraction patterns for the Ni_2MnAl *L*2_1 crystalline phase. The *L*2_1 phase exhibits the highest ordering parameter for the Heusler structure and all three different atoms occupy specific positions in the unit cell therefore the simulated electron diffraction pattern shows all possible diffraction spots. The simulations, and identification of the diffraction spots were performed using the JEMS software [174]

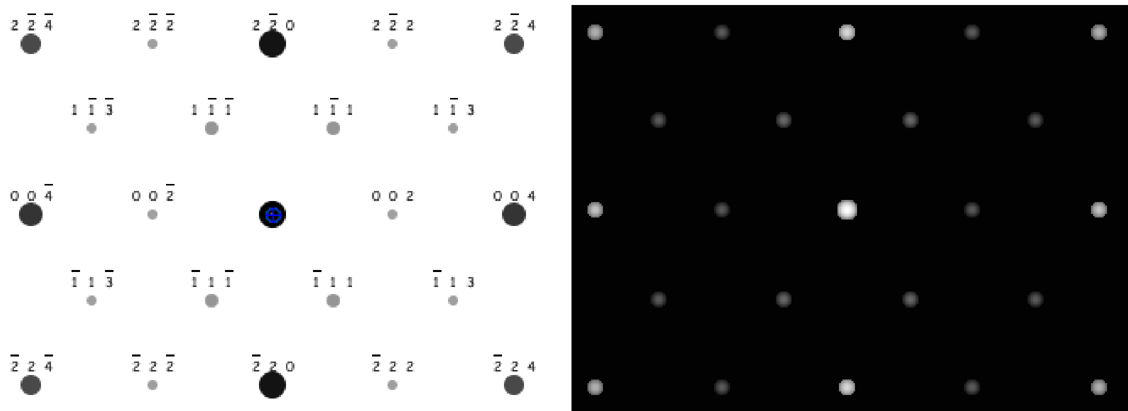

Figure 8.13: X-ray diffraction pattern for epitaxial Ni_2MnAl/Fe bilayer deposited on MgO(001) at elevating temperatures [175].

The epitaxial Ni_2MnAl/Fe bilayer samples were deposited by Tohoku University on single crystal MgO(001) substrates using magnetron sputtering. The bilayer structures were deposited at temperatures ranging from RT to 600°C. As seen in

Figure 8.14, the interfaces of the bilayer structure cannot be resolved atomically due to increased surface roughness.

As shown in Figure 8.14, the substrate interface has a roughness of about 1 nm and epitaxial growth is confirmed. The diffraction pattern matches the (110) zone axis of the Heusler alloy and the expected (220), (200) and (400) electron diffraction spots are visible. A superlattice reflection is also present and matches the (222) crystalline planes of the Heusler alloy. No higher or lower order diffraction spots corresponding to the Heusler structure are visible. No characteristic (111) superlattice reflection is visible which means that Ni_2MnAl crystallises in the partially ordered *B*2 phase. Using Equation 7.6, the lattice parameter was calculated at (0.56 ± 0.05) nm. The orientation of the zone axis of Ni_2MnAl relative to the MgO(001) cutting direction confirms the 45° offset of the structures at the interface as reported in [175]. A diffraction pattern corresponding to the MgO substrate is shown in Figure 8.15.

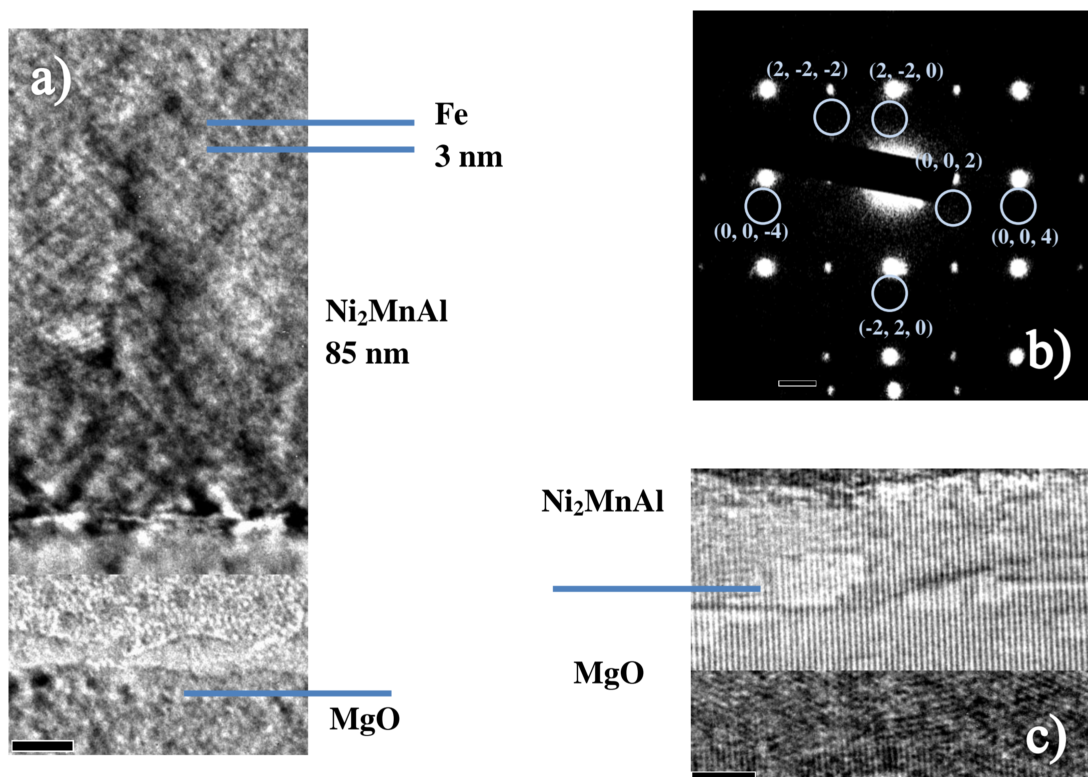

Figure 8.14: a) Cross sectional TEM image and b) corresponding diffraction pattern for epitaxial Ni_2MnAl layer deposited at RT c) MgO (001) substrate/ Ni_2MnAl interface.

Epitaxial Ni_2MnAl/Fe samples deposited at high temperatures were also analysed using cross-sectional TEM. As shown in Figure 8.14, and in particular at the sharp lower interface, in can be confirmed that the growth of the Heusler alloy film deposited on MgO(001) at 600°C was epitaxial.

The diffraction pattern shown in Figure 8.16b) includes both the patterns from the substrate and the film patterns. A disadvantage of acquiring such patterns is that diffraction spots may overlap. In this case, the difference between the position of the MgO(002) family of diffraction spots and the Ni_2MnAl(220) set of peaks is only 0.1 nm. Similar to Ni_2MnAl deposited, only the (222) family of reflections is visible besides the (220) and the (200) set of spots. A third very faint set of diffraction spots is also visible. This set of reflections is not complete and may be an artefact of resputtering at the top interface caused by the Ar ion milling process. The HR-TEM image allows for direct measurement of the lattice constant of Ni_2MnAl which has the value of (0.561±0.01) nm.

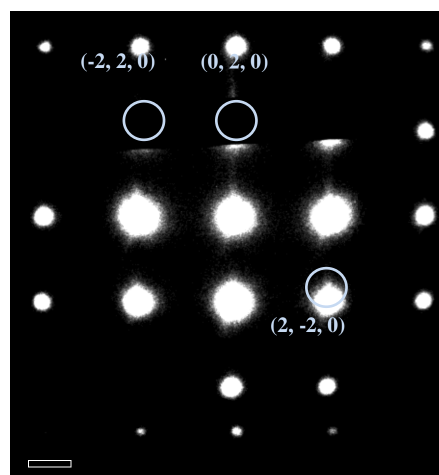

Figure 8.15: Diffraction pattern of MgO (001) substrate.

Epitaxial Ni_2MnAl was reported to have a stable AF phase but as it is the case with other Heusler alloy cubic structures, the AF configuration of the material is thermally unstable due to the reduced value of the magnetocrystalline anisotropy. Exchange bias is therefore observed at temperatures of 10 K [175]. TEM studies show a number of crystalline defects within the structure of the AF film including some grain boundaries. The diffraction pattern analysis shows that there is no noticeable difference between the state of crystallisation of Ni_2MnAl deposited at RT or 600°C. It is obvious that the film deposited at high temperature has a smoother interface with the MgO substrate but the propagation of this effect towards the top interface is unknown. The epitaxial growth of the AF Heusler alloy Ni_2MnAl on MgO(001) is confirmed.

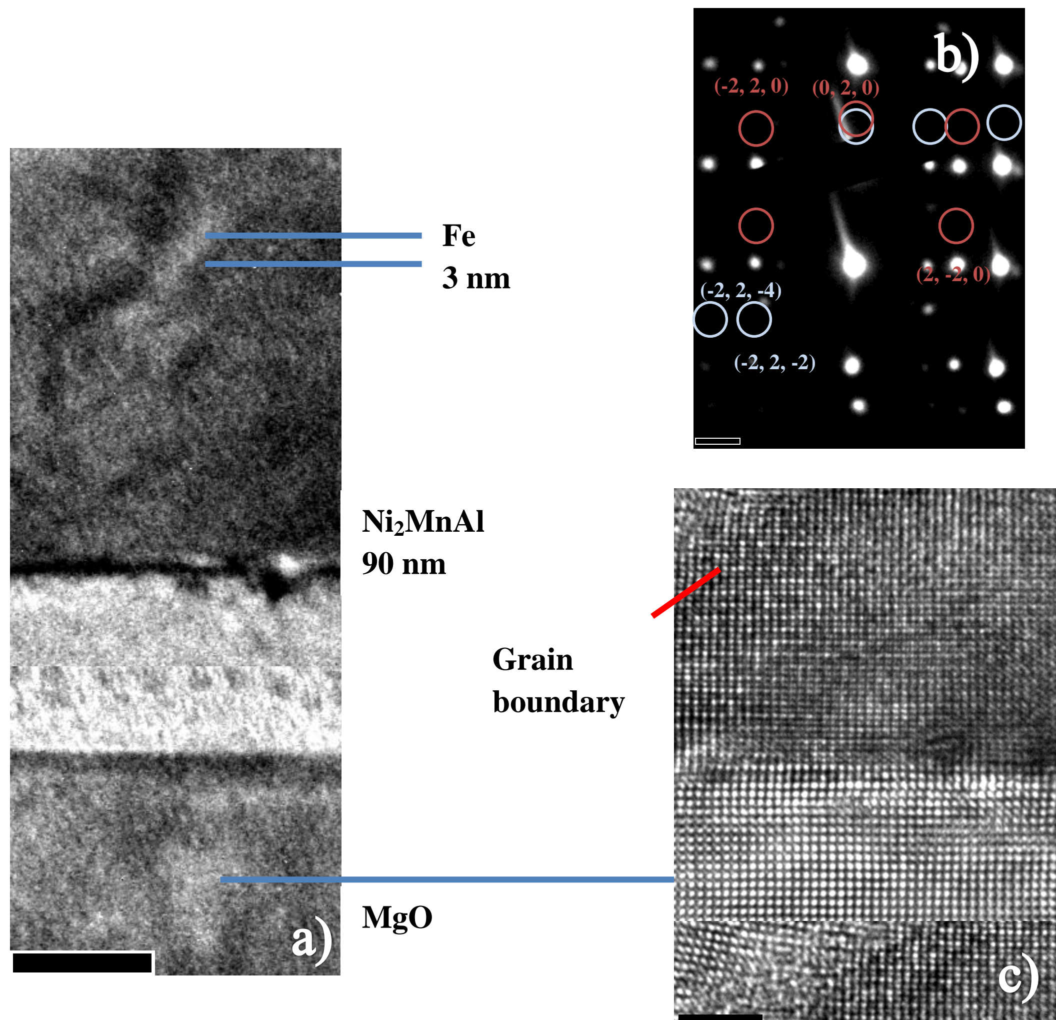

Figure 8.16: a) Cross sectional TEM image and b) diffraction pattern of the $MgO/Ni_2MnAl/Fe$ bilayer deposited at 600°C where orange circles belong to MgO diffraction spots c) HR-TEM image of the substrate interface.

X-ray diffraction studies reported by Tsuchiya *et al.* [175] shown in Figure 8.17 confirm the crystallisation of the antiferromagnetic *B*2 Heusler alloy phase of Ni_2MnAl deposited on a heated MgO(001) substrate. The (002) and (004) characteristic reflections are seen for the complete range of substrate temperatures which spans from RT to 600°C. No superlattice (111) reflection corresponding to the fully ordered ferromagnetic $L2_1$ phase is observed as shown in Figure 8.18. The four fold symmetry is confirmed for the (220) peak while no set of reflections is observed for the (111) planes. The maximum value of H_{EX} reported for this system is 55 Oe at 10 K for the AF Ni_2MnAl deposited at RT.

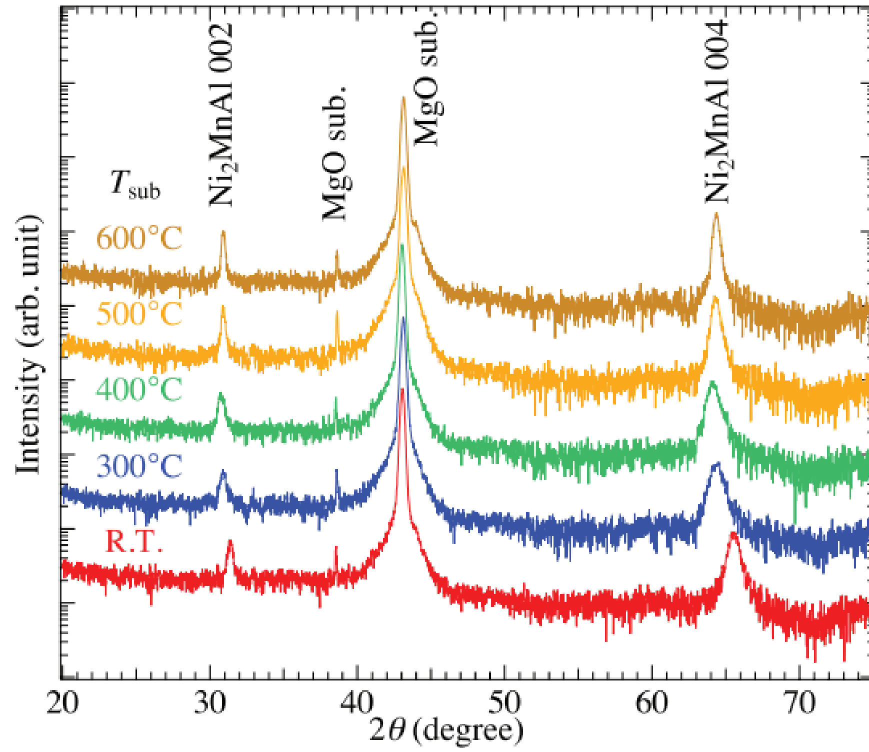

Figure 8.17: X-ray diffraction pattern for epitaxial Ni_2MnAl/Fe bilayer deposited on MgO(001) at elevating temperatures [175].

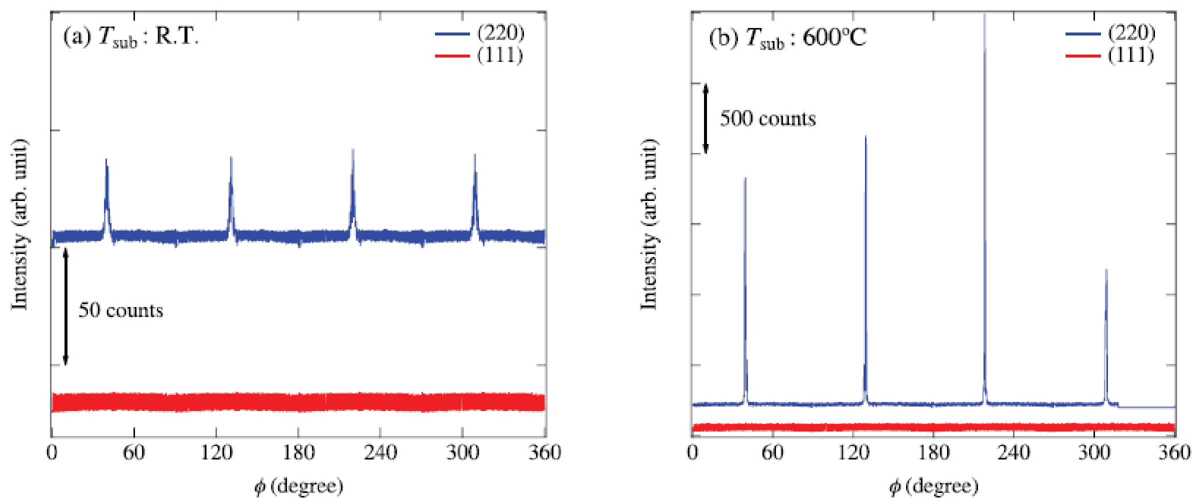

Figure 8.18: Rotational (φ) XRD scans for epitaxial Ni_2MnAl deposited at a) RT and b) 600°C respectively [175].

8.8 Magnetic Characterisation of Epitaxial Ni_2MnAl

The epitaxial Ni_2MnAl was shown to have a stable AF phase and induce a hysteresis loop shift when coupled to a F layer. The work published by Tsuchiya *et al.* [175] confirms the low temperatures required for the thermal stability of the AF phase due to the decreased magnetocrystalline anisotropy of Ni_2MnAl. The epitaxial AF Ni_2MnAl deposited at RT requires a low temperature of 10 K in order to induce the loop shift of the neighbouring Fe layer. The value of the induced exchange bias after field cooling is a maximum of 55 Oe at 10 K with a calculated value of the exchange coupling energy of 0.003 erg/cm^2. The blocking temperature of epitaxial Ni_2MnAl is found to be below 100 K as shown in Figure 8.19. The exchange bias decreases as the substrate temperature is raised up to 600°C. The large grain epitaxial structure relies on domain wall movement for the magnetisation reversal process which is an intrinsically non anisotropic process.

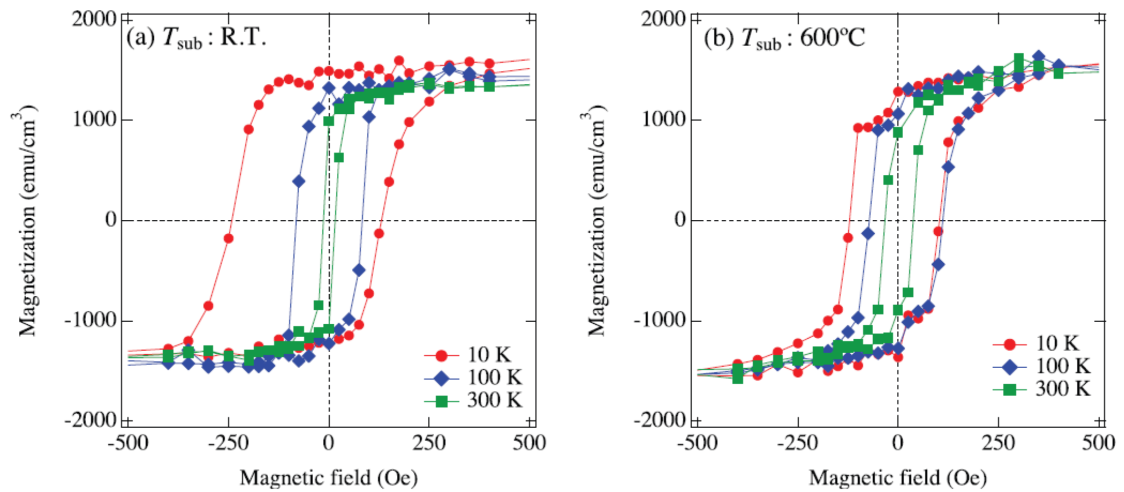

Figure 8.19: Hysteresis loops for the Ni_2MnAl/Fe bilayers measured at 10, 30 and 100 K. The Ni_2MnAl films were deposited at a) RT and b) 600°C [175].

Although small grain polycrystalline Ni_2MnAl is expected to show an increase in antiferromagnetic anisotropy (K_{AF}), if the blocking temperature (T_B) is lower than 300 K, the alloy is unsuitable for RT device applications therefore a solution for increasing K_{AF} is required.

8.9 Structural, Magnetic and Electric Characterisation of Ru_2MnGe

8.9.1 Epitaxially Deposited Ru_2MnGe

The antiferromagnetic Ru_2MnGe Heusler alloy was deposited by the Centre for Spinelectronic Materials and Devices at Bielefeld University in Germany via magnetron co-sputtering on heated MgO substrates. Epitaxial Ru_2MnGe/Fe bilayers were deposited on MgO(001) single crystal substrates in order to induce lattice matched growth of the Heusler alloy. A 2 nm thick iron layer was used for exchange bias measurements and a 2 nm magnesium oxide capping layer was deposited to prevent oxidation of the bilayer structure. Figure 8.20 shows cross sectional bright field TEM images of the Ru_2MnGe/Fe structure deposited on MgO(001).

As shown in Figure 8.20, the lattice matched growth of the Heusler alloy on the MgO substrate is confirmed. The high degree of ordering protrudes through the Ru_2MnGe to the top MgO capping layer. The iron layer is expected to be 1.5-2 nm thick but due to the similar Z value of the two materials, the difference in contrast is expected to be minimal. A number of crystalline defects are observed along the Heusler alloy structure but the long range ordering of the material is not affected. The structural studies performed using the electron microscope and X-ray diffraction by Balluff *et al.* [149] confirms the crystallisation of the Heusler *B*2 phase using an optimum substrate temperature of 500°C. Rocking curve measurements on both (002) and (004) Heusler alloy characteristic reflections show a value of the full width at half maximum (FWHM) of less than 0.03° which arises from characteristic instrument broadening as shown in Figure 8.21.

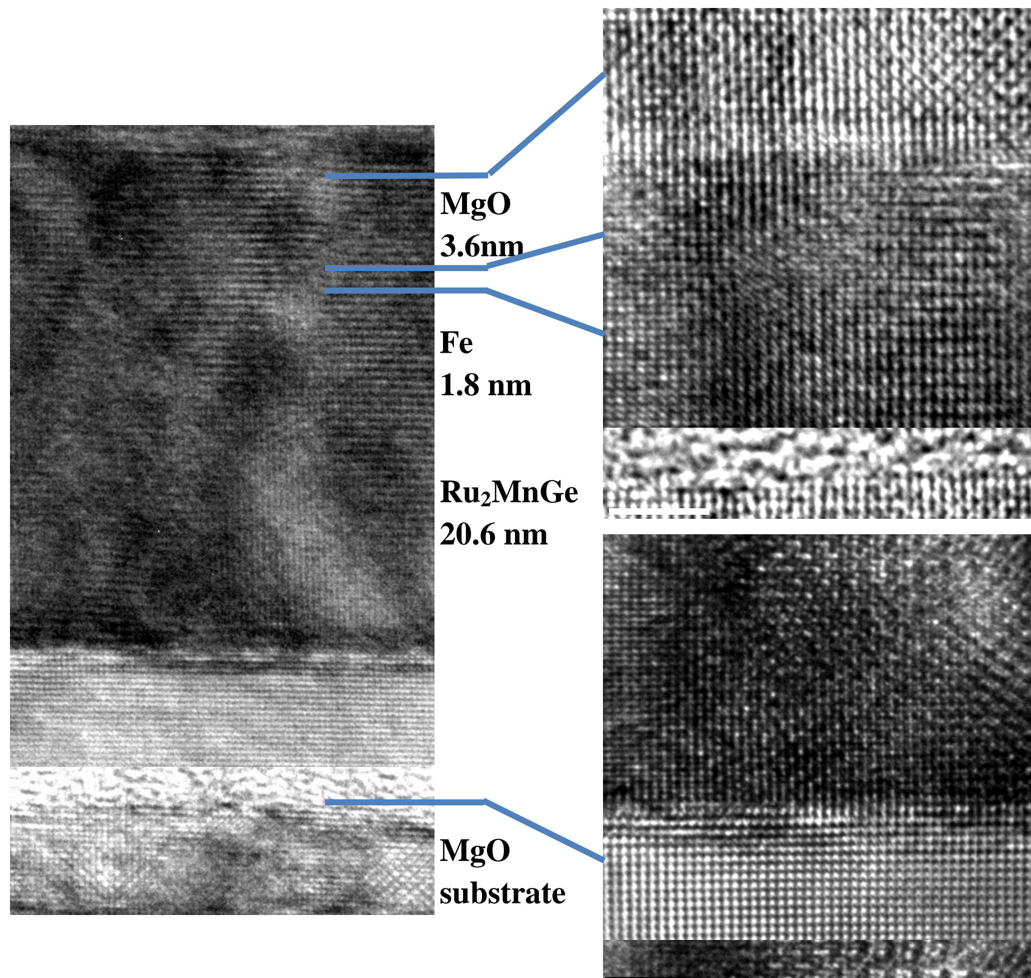

Figure 8.20: Cross-sectional TEM image of the epitaxially deposited Ru_2MnGe(110)/Fe bilayer on a MgO(001) substrate.

AF films that are grown epitaxially in the form of a single crystal or having large grains are known to have an AF domain structure [139]. This AF domain structure arises because of the domain patterns in any adjacent ferromagnets which can be transferred into the AFs via exchange coupling.

The nature of such an AF domain structure and its behaviour is generally not known and there exists a significant controversy as to the actual behaviour. However, previous work conducted in York has shown that whatever the true nature of AF domains and their behaviour, they can be well represented by a simple domain wall pinning model [176]. In this model AF domain walls become strongly pinned at defects or inclusions in the large grain or single crystal sample. For example in the case of a large grain (D>25 nm) the domain walls will become irreversibly pinned at

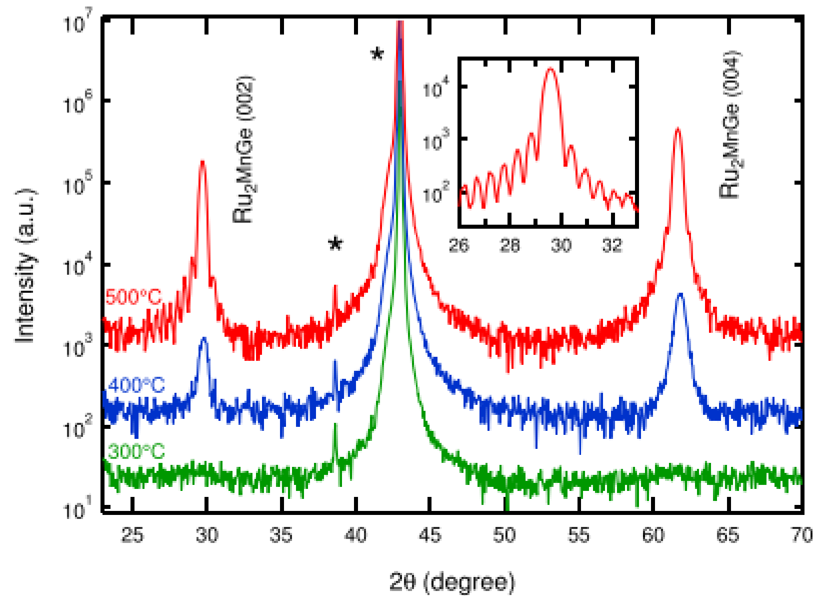

Figure 8.21: X-ray diffraction pattern for epitaxial Ru_2MnGe [149].

grain boundaries because of the absence of intergranular coupling in a large grain AF system. However relatively minor defects such as inclusions, even down to the atomic scale, will tend to pin domain walls because of the absence of magnetostatic energy in the AF layer itself. For example it was shown that introducing a relatively low level of impurity such as Cu atoms into a conventional AF can more than double the resulting exchange bias due to the pinning of the domain walls and, where the pins are sufficiently strong, effectively breaking up the magnetic domains in the large grains into smaller magnetic domains which, when they become sufficiently small, can become thermally unstable such that at high levels of impurity doping the exchange bias then falls [176]. Similar behaviour is observed when ion bombardment is used to induce defects into single crystal AF films [177].

The York protocol was used to characterise the antiferromagnetic properties of the epitaxial Ru_2MnGe films. The measurements were performed at low temperatures as the Ru_2MnGe Heusler alloy is expected to have low anisotropy due to the cubic symmetry and the (001) orientation is hence thermally unstable AF configuration. Figure 8.22 shows the results of the hysteresis loop and blocking temperature graph for the epitaxial Ru_2MnGe/Fe bilayer deposited on MgO(001).

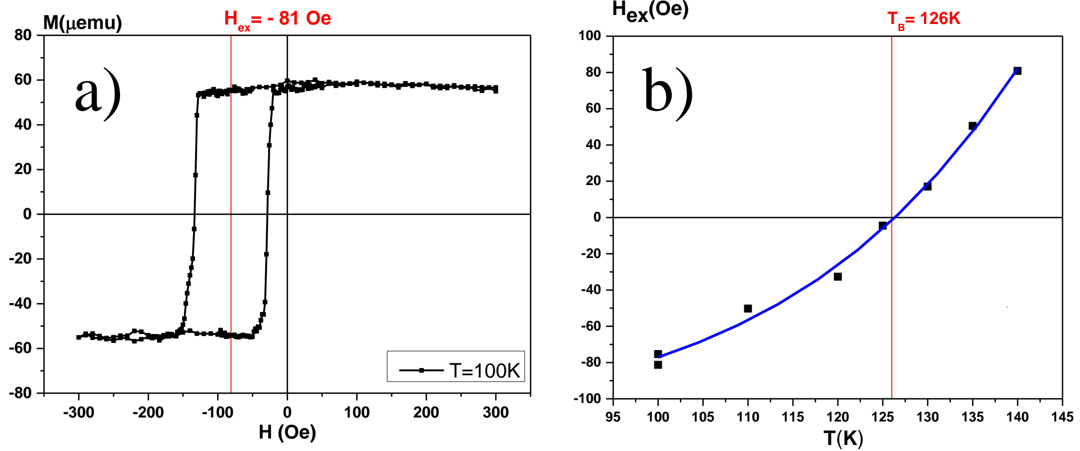

Figure 8.22: a) Hysteresis loop and b) blocking temperature graphs for the epitaxial Ru_2MnGe/Fe exchange bias bilayer deposited on MgO.

Figure 8.22a) shows the standard exchange bias as measured for a sample of Ru_2MnGe and iron. This is a result for an epitaxially grown film which is determined to have a large grain size (D>50 nm). Hence the reversal mechanism and thus the anisotropy in the AF layer is manifest via strong domain wall pinning. In this case the film was not doped deliberately with any inclusions so as to induce stronger domain wall pinning and presumably therefore the pinning sites occurred at natural defects in the large grains and at the grain boundaries within the film.

Examination of the hysteresis loop shows that the reversal in the F layer nucleates quickly followed by rapid domain wall motion until just past the coercivity where a slight rounding of the loop occurs due to the presence of a few strong domain wall pins in the AF layer.

The value of the loop shift of 81 Oe is modest particularly considering that the measurement temperature in this case is 100 K. At room temperature this sample does not exhibit exchange bias.

Figures 8.23 shows polar plots of the coercivity and remanence of the loop as a function of the angle of the applied field relative to the sample of Ru_2MnGe measured at room temperature. It is interesting to note, particularly for the H_c data, that a significant anisotropy exists in this material. Of course the coercivity has its origin in domain wall pinning but nonetheless the marked variation indicates that the effect of aligning the antiferromagnet remains conspicuous even at an elevated temperature where the AF has in principle relaxed. Nonetheless this data and particularly that shown in Figure 8.23 shows that this material is anisotropic.

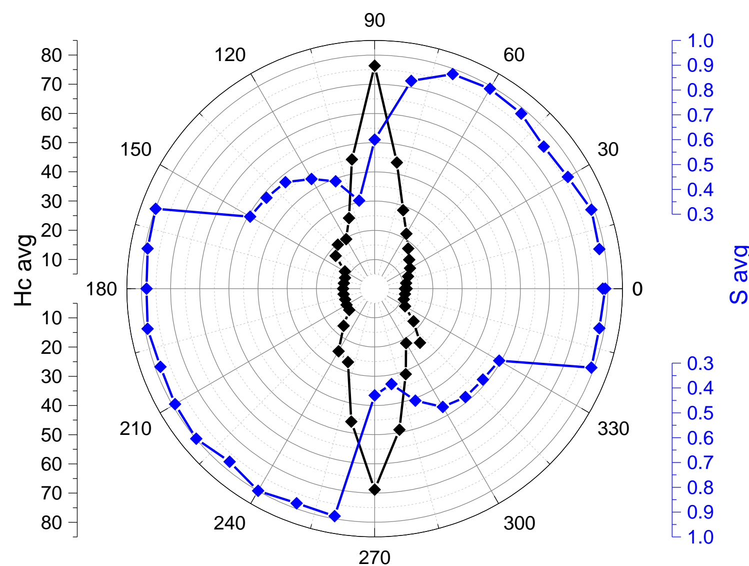

Figure 8.23: Polar plot of the coercivity (black) and squareness (blue) for Ru_2MnGe/Fe.

As discussed previously it should be possible to increase the level of exchange bias exhibited by this material via the use of doping *e.g.* with Cu. This should give a system that may be thermally stable up to room temperature. However it is unlikely that a system such as this would exhibit a significant exchange bias at room temperature and particularly up to 373K which is the specified operating temperature of most spintronic devices due to its small anisotropy induced by the cubic nature. Hence the objective must be to find similar Heusler alloys exhibiting sheet antiferromagnetism and thereby displaying a higher anisotropy.

8.9.2 Integration of Epitaxial Ru_2MnGe in Spintronic Devices

As discussed previously in Section 8.9.1, Ru_2MnGe has proven to have a stable antiferromagnetic phase with a measured blocking temperature of almost 130 K. Thin film magnetic tunnel junction (MTJ) devices were prepared by the Center for Spinelectronic Materials and Devices, Bielefeld University Germany using DC and RF magnetron co-sputtering together with electron beam evaporation. The Heusler alloy layers were deposited using Ar process gas at a pressure of 2.3×10^{-3} mbar. The base pressure of the sputtering system is lower than 10^{-8} mbar. The MgO single crystal substrate ($a_{MgO} \times \sqrt{2} = 5.957$ Å) is known to have a 0.5% lattice mismatch when compared to bulk Ru_2MnGe ($a_{Ru2MnGe} = 5.985$ Å) [178].

Figure 8.24 shows cross sectional TEM images of the MTJ multilayer structure.

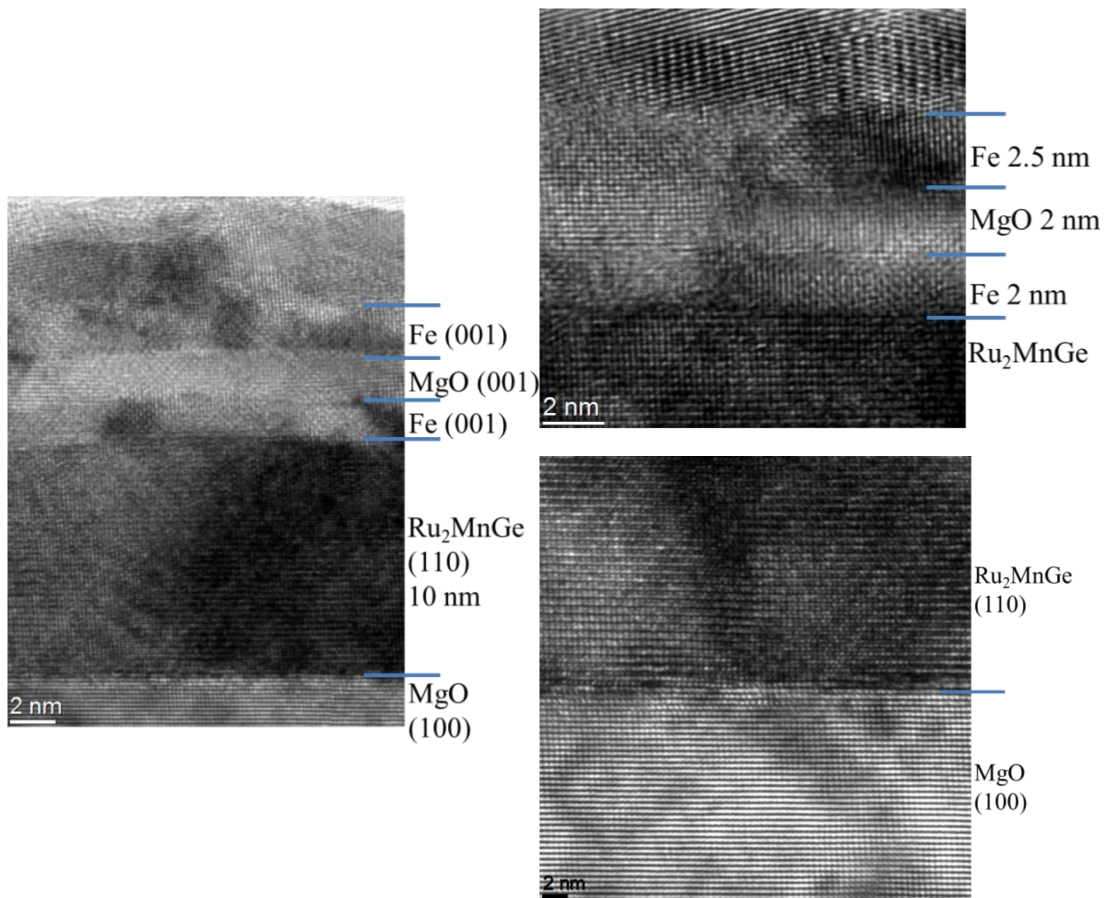

Figure 8.24: Cross sectional TEM image and TMR curve for $Ru_2MnGe/Fe/MgO/Fe$ MTJ [178].

As shown in Figure 8.24 a 2 nm thick MgO tunnel barrier was deposited between two epitaxially grown Fe electrodes with the bottom Fe layer coupled to a 10 nm thick epitaxial Ru_2MnGe layer. The AF layer was deposited at a substrate temperature of 500°C and then annealed in situ for one hour at the same temperature. The Fe/MgO/Fe stack was deposited at RT. The images show the high crystalline quality of the epitaxial multilayer structure dictated by the excellent lattice matching between the substrate and the AF Heusler layer. All the interfaces are sharp and atomically flat which is beneficial for coherent tunnelling of electrons across the insulating barrier. No grain boundaries are observed across the observable width of the TEM specimen.

In order to observe the tunnelling magnetoresistance of the Ru_2MnGe based structure, the samples were patterned in a standard UV lithography system combined with Ar ion etching. Square MTJ cells measuring 7.5 x 7.5 µm were patterned. The samples were bonded to chip carriers using Au wire and cooled down in a closed He cryostat in an applied magnetic field of 4T below the blocking temperature of the AF layer. A constant voltage of 10 mV was applied across the MTJ while an external magnetic field is swept in a parallel configuration. Figure 8.25 shows the magnetoresistance measurements where the TMR = $(R_{ap}-R_p)/R_p$ is plotted against the magnetic field.

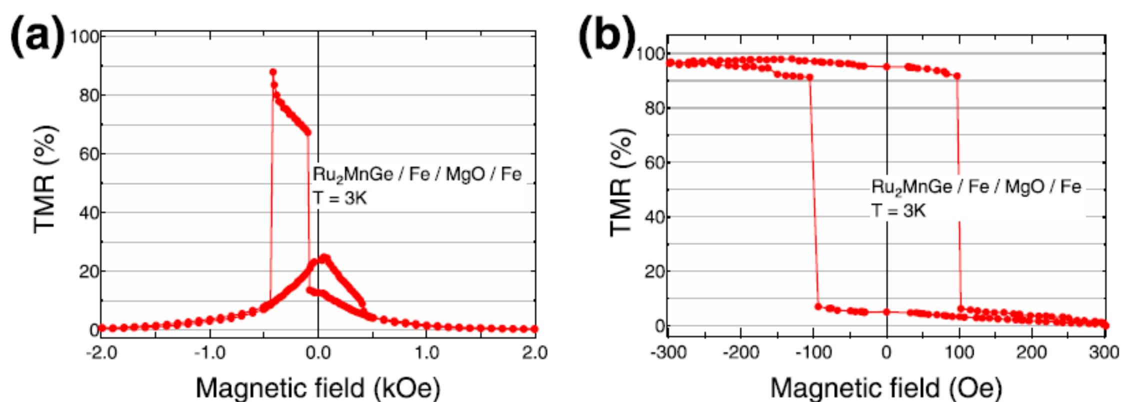

Figure 8.25: TMR curve for Ru_2MnGe/Fe/MgO/Fe MTJ at 3 K: a) majour loop showing the switching of the whole stack b) minor loop showing only the switching of the free ferromagnetic Fe layer [178].

As shown in Figure 8.25 a), asymmetric switching is observed and caused by the shift induced in the hysteresis loop of the pinned Fe layer. The switching mechanism is affected by the quality of the lithographically prepared devices. A reduction in the lateral size of the devices is expected to improve the TMR ratio by achieving single domain switching as a result of reducing possible defects induced by the patterning process. Figure 8.25 b) shows an almost perfect switching of the free layer and a resulting TMR ratio of almost 100% at 3 K.

The tunnel junctions were post annealed at temperatures of up to 400°C in a vacuum furnace at a pressure of 10^{-7} mbar before patterning. The TMR values were then measured at RT (300 K) and the results are shown in Figure 8.26.

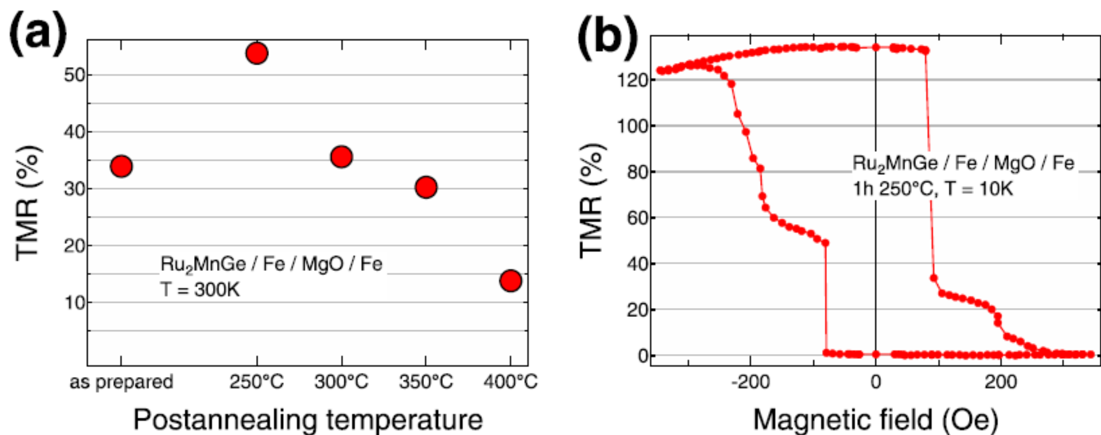

Figure 8.26: a) TMR ration measured at 300 K for post annealed Ru_2MnGe based MTJ stacks. b) Low temperature multi-domain switching behaviour of the free Fe layer of an MTJ annealed at 250°C [178].

As shown in Figure 8.26 a), the maximum value of the TMR ratio recorded at RT for the Ru_2MnGe based MTJs is over 50%. The optimum post annealing temperature is 250°C. Figure 8.26 b) shows the multi domain switching behaviour of the post annealed free Fe electrode when measured at 10 K. The maximum value of the TMR ratio becomes 135%.

8.9.3 Polycrystalline Ru_2MnGe

The antiferromagnetic Ru_2MnGe Heusler alloy was deposited via magnetron co-sputtering on Si/SiO_2 substrates using magnetron co-sputtering and post-annealed using rapid thermal annealing (RTA) in order to induce the crystallisation of the $L2_1$ AF crystalline phase. Again a 2 nm thick Fe layer was used for exchange bias measurements as in the case of the epitaxial system described previously. The polycrystalline Ru_2MnGe/Fe bilayer is reported to have a lower blocking temperature with a value of less than 100 K [149] compared to $\langle T_B \rangle = 126$ K for the epitaxial system discussed previously. Cross-sectional TEM studies and 3D local electrode atom probe tomography studies (3D LEAP) were performed in order to determine the origin of the unexpected decreased thermal stability of the polycrystalline AF configuration of the alloy.

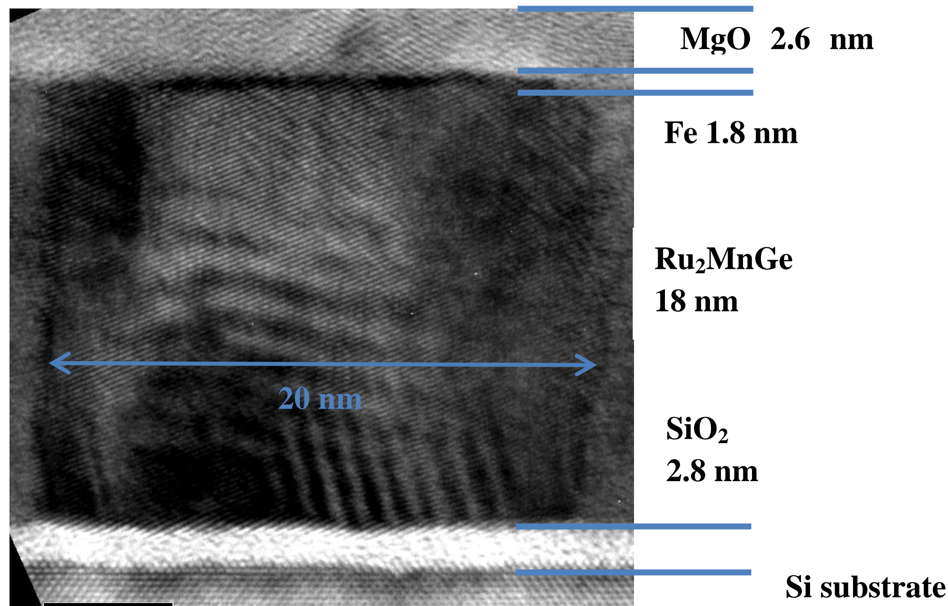

Figure 8.27: Cross-sectional TEM image of the polycrystalline Ru_2MnGe/Fe bilayer.

As shown in Figure 8.27, the polycrystalline Ru_2MnGe shows a granular structure with long range ordering over lateral distances of up to 20 nm. A pronounced contrast is also visible in the bright field image due to the main element composing the alloy, ruthenium which has almost twice the atomic mass of the conventional transition metals. Figure 8.21 shows a high resolution aberration corrected TEM image of the Ru_2MnGe/Fe bilayer.

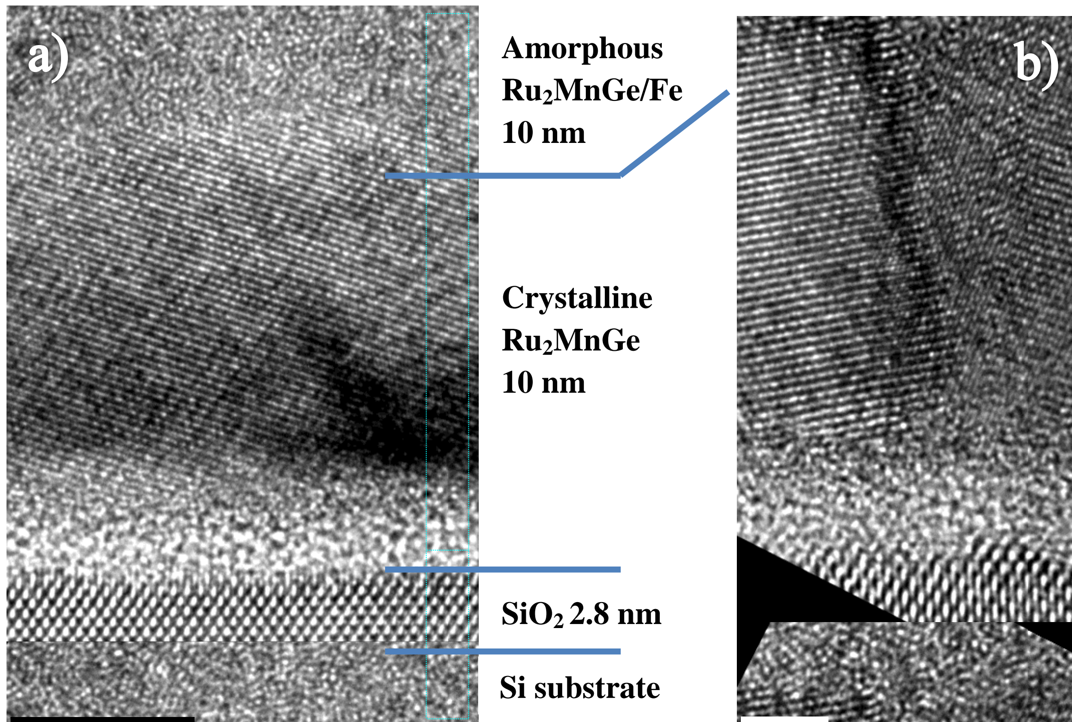

Figure 8.28: a) HR-TEM image of the polycrystalline Ru_2MnGe/Fe bilayer. b) Grain boundary in polycrystalline Ru_2MnGe.

As seen in Figure 8.28, the bottom half of the 20 nm thick polycrystalline Ru_2MnGe film has good crystallisation and the grain size is in the 15 to 20 nm range but the top half of the Heusler alloy film and the ferromagnetic layer exhibit almost no clear order so the material is borderline amorphous. As the interface to the Fe layer is not visible it is believed that Fe is mixed into the Heusler alloy AF layer. This may account for the inferior thermal stability of the polycrystalline Ru_2MnGe compared to the epitaxial film.

In order to confirm the hypothesis of intermixing occurring at the Ru_2MnGe/Fe interface, an elemental mapped three dimensional (3D) reconstruction of the Ru_2MnGe/Fe bilayer was performed by means of atom probe tomography (APT) in the International Research Center for Nuclear Material Science at Tohoku University, Oarai, Japan. The specimens consist of FIB-fabricated nanopillars and needles which are gradually evaporated in a controlled manner using high intensity short voltage pulses and/or high power laser pulses. A planar detector which faces the sample records the chemical composition and coordinates of the ejected atoms. A

3D chemical map of the sample is therefore created. Figure 8.29 shows the final stages of FIB preparation of samples for APT measurements.

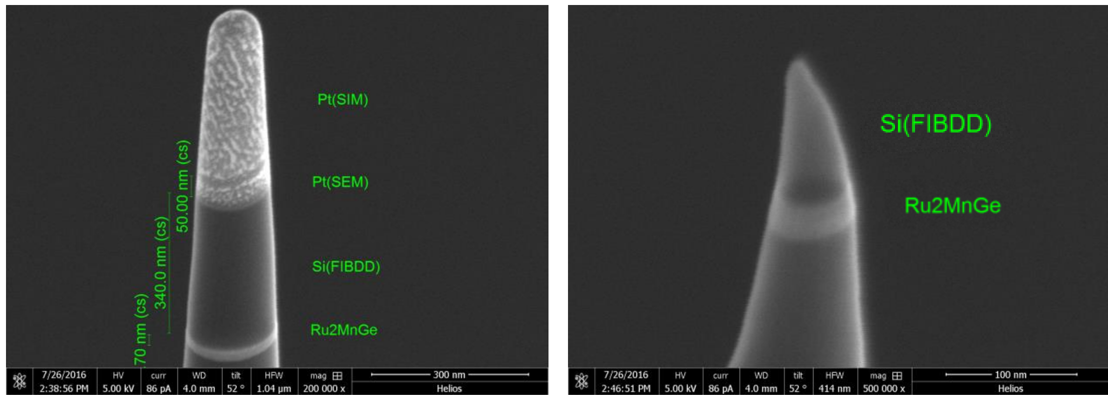

Figure 8.29: SEM images of a nanopillar specimen for 3D APT measurements.

As shown in Figure 8.22, the specimen preparation using the focused ion beam is similar to the process used for cross-sectional TEM samples described in Section 7.3.2. A noticeable difference between the processes is the deposition of a silicon and heavy metal layer on the thin film structure. The heavy metal protection layer helps in shielding the area of interest from unwanted ion beam damage.

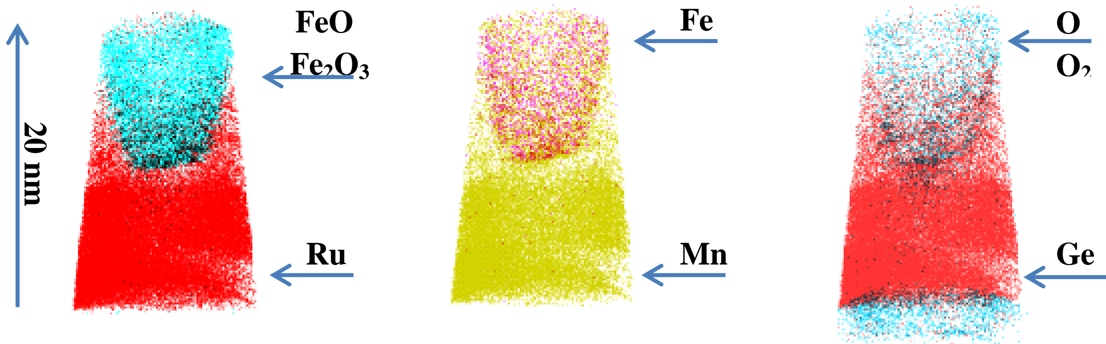

Figure 8.30: Elemental mapping for the polycrystalline Ru_2MnGe/Fe bilayer.

As shown in Figure 8.30, the APT measurements confirm the occurrence of significant intermixing of the ferromagnetic Fe layer into the polycrystalline Ru_2MnGe. The chemical composition of the Heusler alloy is stable for the lower half of the thin film which coincides with the crystalline phase observed in the HR-TEM images in Figure 8.28. Examining the chemical composition of the mixed interface reveals the formation of oxides throughout the top half of the bilayer exchange bias system. The origin of the oxidation process is not understood however, the rapid thermal annealing process used to crystallise the structure and the preparation

process required for the atom probe tomography and cross-sectional TEM measurements may induce some chemical changes to the bilayer structure. As the magnetic pinning effect requires a sharp interface between the F and AF thin films, the pronounced oxidation and mixing of the two layers decreases the strength of coupling between the layers and also the vertical grain size of the polycrystalline Heusler alloy film. Decreasing the thickness of a granular AF thin film causes the energy barrier for reversal of the antiferromagnetic grain to drop by a factor 8 as $\Delta E = K_{AF}V$ and therefore the thermal stability is seriously affected.

Polycrystalline Ru_2MnGe has shown a stable AF phase and was reported to have a blocking temperature of less than 100 K and a rapid decrease of values of H_{EX} with the increase of temperature [149]. HR-TEM and 3D APT measurements have shown the origin of the decreased thermal stability and pinning strength of the polycrystalline AF Heusler alloy when compared to the epitaxial Ru_2MnGe/Fe system due to the mixed interface and partial oxidation.

9 Structural and Magnetic Properties of Polycrystalline MnN

The interest in MnN arises from the possibility of crystallisation of two tetragonal phases out of the total of four possible configurations of the unit cell with the remaining two phases having cubic symmetry [179] as shown in Figure 9.1.

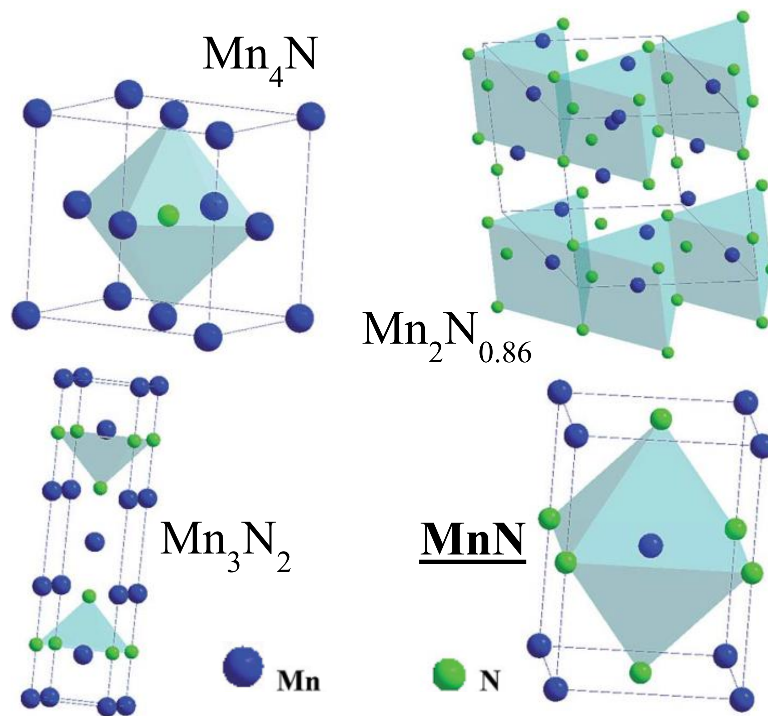

Figure 9.1: Representation of unit cells corresponding to different phases and stoichiometries of MnN.

It is expected that any tetragonal distortion would increase the antiferromagnetic anisotropy of the material. Theoretical studies predict the equiatomic composition of MnN has the lowest formation energy and for this work, in thin film form, a small tetragonal distortion is measured with $c/a \approx 1.04$ where $a \approx 4.10$ Å [150]. The 1:1 stoichiometric MnN crystalline structure is known as the θ phase or θ-MnN.

9.1 Polycrystalline MnN Deposited via Reactive Magnetron Sputtering

Polycrystalline MnN compound was deposited by the Centre for Spinelectronic Materials and Devices in Bielefeld Germany via reactive magnetron sputtering on thermally oxidised silicon substrates. The process gas used for the deposition is a mixture of 50:50 $Ar:N_2$ and in order to promote the crystallisation of the MnN equiatomic phase, post-annealing in vacuum is required. More details related to the experimental procedure can be found in the work published by Meinert *et al.* [150].

The interest in MnN arises from the possibility of crystallisation of two tetragonal phases out of the total of four possible configurations of the unit cell with the remaining two phases having cubic symmetry [179]. It is expected that any tetragonal distortion would increase the antiferromagnetic anisotropy of the material. Theoretical studies predict the equiatomic composition of MnN has the lowest formation energy and for this work, in thin film form, a small tetragonal distortion is reported with $c/a \approx 1.04$ where $a \approx 0.41$ nm [150]. The 1:1 stoichiometric MnN crystalline structure is known as the θ phase or θ-MnN.

Figure 9.2 shows the X-ray diffraction pattern of a MnN/CoFe bilayer deposited on a 10 nm thick Ta seed layer and capped with Ta and TaO_x. The spectrum shows only the (002) and (004) reflections corresponding to θ-MnN. The 1.8 nm thick CoFe layer allows for increased pinning strength in exchange bias measurements but no signal is observed from the F layer in the out of plane XRD spectrum. The broad (004) reflection shows the polycrystalline nature of the MnN AF layer. Moreover the film is expected to have a strong (001) texture and good crystallisation as no secondary phase formation is observed.

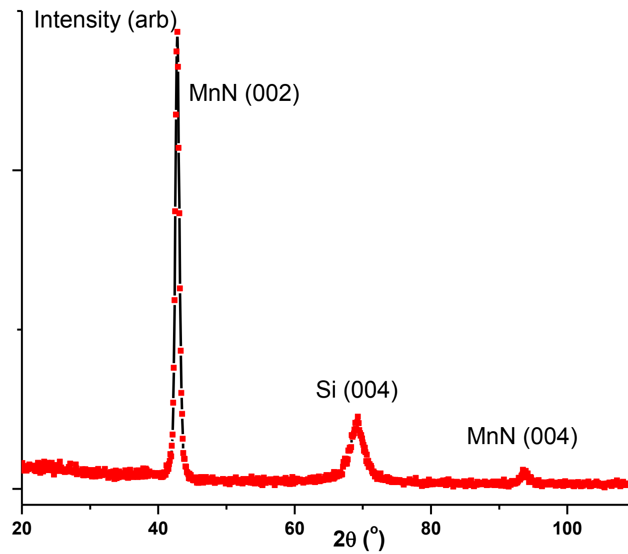

Figure 9.2: X-ray diffraction pattern for the Ta/MnN/CoFe stack.

Cross-sectional TEM studies have been conducted in order to gain an insight into the structure of Ta/MnN/CoFe multilayer system. As shown in Figure 9.3, the columnar granular growth of polycrystalline antiferromagnetic MnN is confirmed. The images show well defined and textured grains with lateral dimensions in the range of 10 to 20 nm. In order for the θ-MnN AF to crystallise, the 10 nm Ta seed layer is necessary and although the Ta layer does not show a defined crystalline structure, some intermixing can be observed at the interface between the seed and AF layer. The mixed interface shows the origin of crystallisation of the MnN thin film. From the TEM images, a 1 to 2 nm thick mixed and crystalline layer is observed between the two materials. A plausible hypothesis is that during the post annealing process where the stack is heated to 300°C, nitrogen may diffuse into the Ta seed layer forming TaN which may become the basis for the crystallisation of the antiferromagnet. Meinert *et al.* [150] reported the successful crystallisation of the AF phase of MnN only in the presence of a Ta underlayer.

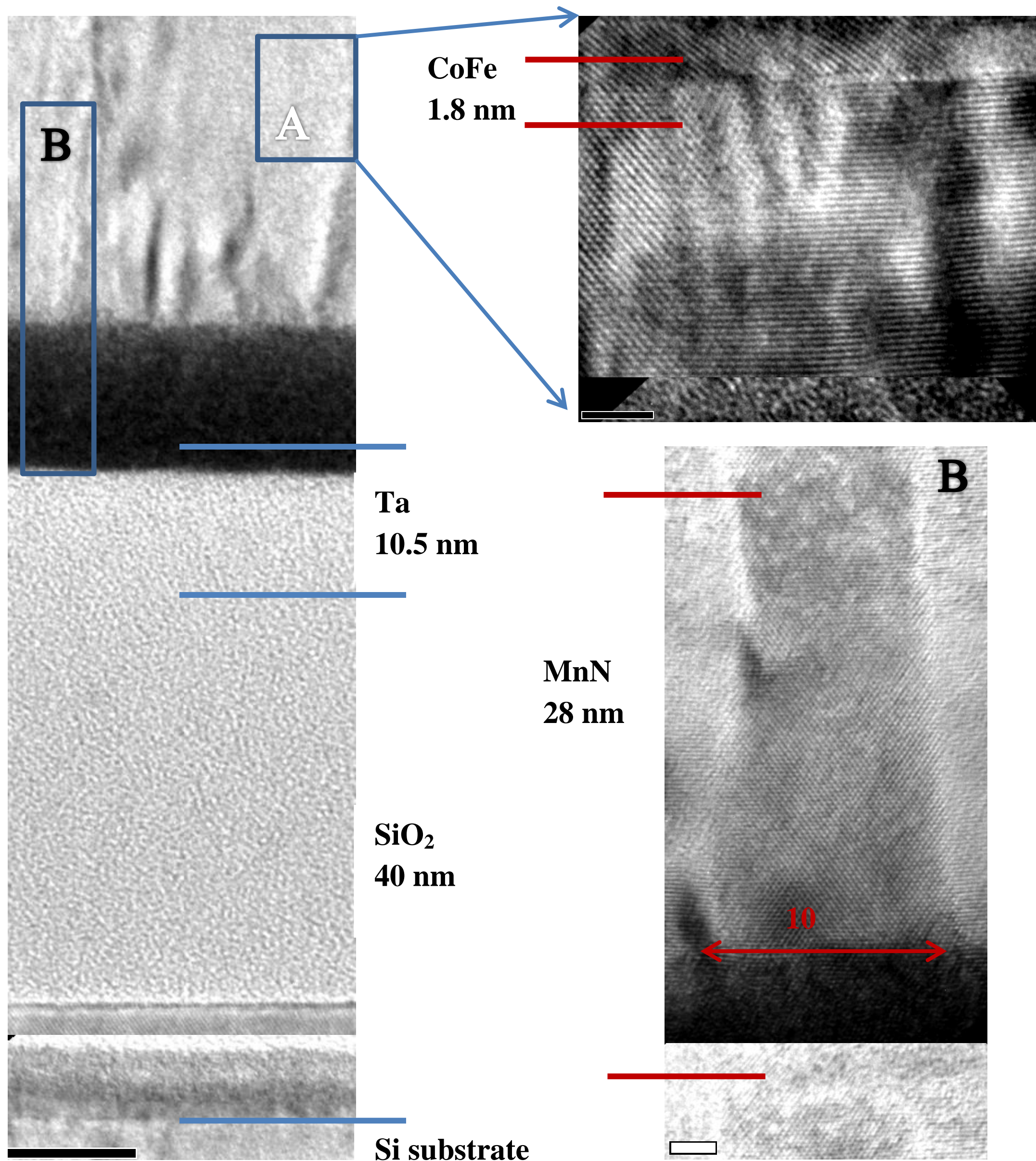

Figure 9.3: Cross-sectional TEM images of the polycrystalline Ta/MnN/CoFe stack.

TEM images show a sharp interface between the AF and the ferromagnetic CoFe layers which is expected to enhance the exchange coupling. A closer look at this interface shows an atomically sharp transition from the AF to the F layer and in places, epitaxial type growth is observed. The 1.8 nm thick CoFe layer shows a highly ordered crystalline structure and no mixing along the magnetically coupled interface. The polycrystalline MnN/CoFe system deposited by magnetron sputtering can be used as a reference for the quality of the exchange bias interface. The hysteresis loop seen in Figure 9.4 confirms the strong exchange coupling of the θ-MnN and CoFe.

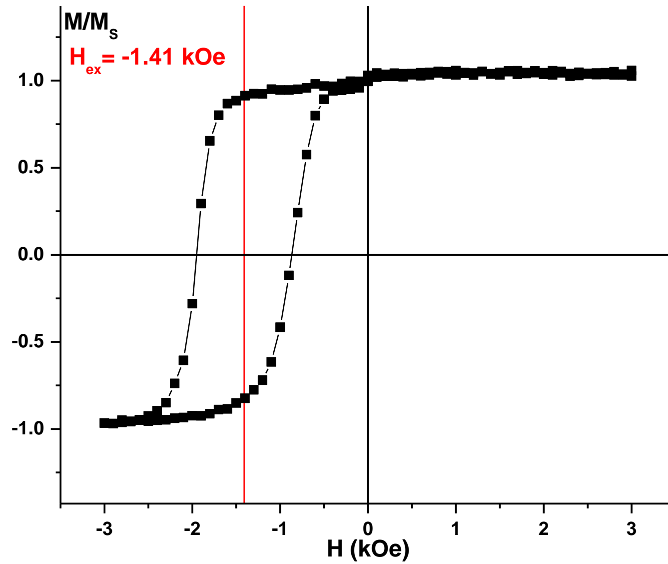

Figure 9.4: Exchange bias hysteresis loop for MnN/CoFe at room temperature.

As shown in Figure 9.4, an exchange bias field (H_{EX}) of over 1.4 kOe is induced by the MnN AF layer when set in a field of 10 kOe at a temperature of 225°C for 90 minutes following the York protocol. The sample was found to be thermally stable at RT by reversing the applied field for 30 minutes and measuring the resulting hysteresis loop. A negligible training effect was removed by running a second loop after the field setting process. Figure 9.5 shows the controlled thermal activation process as part of the York protocol for exchange bias measurements which is used to determine the antiferromagnetic anisotropy constant (K_{AF}) of θ-MnN.

As shown in Figure 9.5, the median blocking temperature of the antiferromagnetic MnN is $<T_B>$ =388K (114.8°C) which makes the material suitable for some applications. The maximum value for T_B was reported by Meinert *et al.* to be 160°C when the thickness of the AF layer is increased to 50 nm. This value is lower for MnN when compared to IrMn (222°C) or PtMn (283°C) [150]. Using Scherrer analysis and the data from the X-ray diffraction pattern in Figure 9.1, the mean grain size of the film was calculated $D_{mean} \approx$ 14 nm. By using the York Model of Exchange bias and the fitting parameters of the blocking temperature distribution, the antiferromagnetic anisotropy constant for θ-MnN is determined to be $K_{AF} = 5.1\text{x}10^5$ ergs/cm^3. This value is almost two orders of magnitude lower than K_{AF} for IrMn.

MnN also requires a minimum AF film thickness of about 30 nm which equates to considerably larger grains being required for the thermal stability of the compound. Although MnN has potential for usage in spintronic devices as a pinning layer, the increased minimum thickness of the AF layer does not allow for implementation in applications such as HDD read heads and MRAM cells where the increased storage density and etching limitations only allow an AF layer maximum thickness of 10 nm.

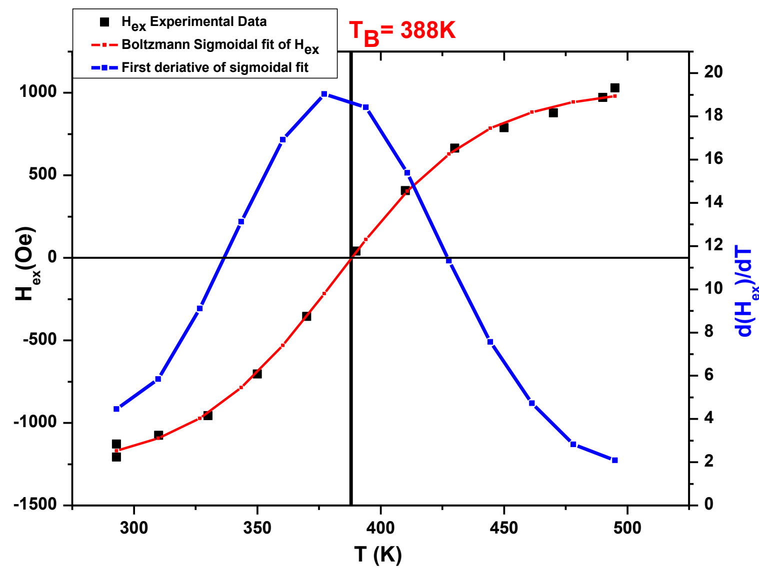

Figure 9.5: Blocking temperature measurement of the AF polycrystalline θ- MnN.

9.2 Polycrystalline MnN Deposited via Reactive HiTUS Sputtering

MnN was also deposited using the HiTUS system and a mixture of 50:50 Ar:N_2 sputtering gas. The structure of the stack is similar to the sample deposited via magnetron sputtering: Si/SiO_2 substrate/Ta seed layer (10 nm)/MnN (30 nm)/CoFe (2 nm)/Ta (2 nm). A number of seed layers were investigated for the growth of the AF θ-MnN: Al, Ru, Pt, Ag and Ti. The materials were chosen in order to match the lattice parameter of the MnN. Following initial experiments, none of the materials used to replace the Ta seed layer have shown improvement of the thermal stability or crystallisation of the AF MnN compound. The AF MnN was then deposited on a 10 nm Ta seed layer. Post-annealing experiments revealed some chemical instability in the structure deposited via HiTUS as shown in Figure 9.6.

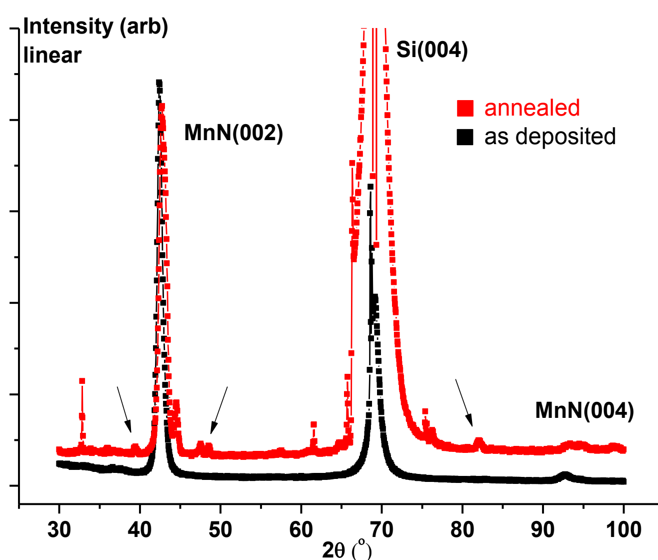

Figure 9.6: XRD spectrum for Ta/MnN/CoFe deposited via HiTUS at -900V.

The AF MnN shows some crystallisation in the as deposited state. Post-annealing the structure at 200°C causes some segregation and formation of secondary compounds seen as additional reflections in the XRD spectrum shown in Figure 9.6. The XRD measurement shows a number of reflections which are not characteristic of the AF θ phase of MnN. Both nitrogen desorption and oxidation of the structure may play a role in the formation of secondary compounds.

Grain size analysis was performed on the specimens deposited via HiTUS. Bright field electron microscopy images were taken using a carbon coated copper TEM grid as support for the thin film stack. Using an equivalent circle method and a Zeiss particle size analyser, a grain size distribution plot was generated as shown in Figure 9.7. More than 500 grains were measured in order to insure good statistics.

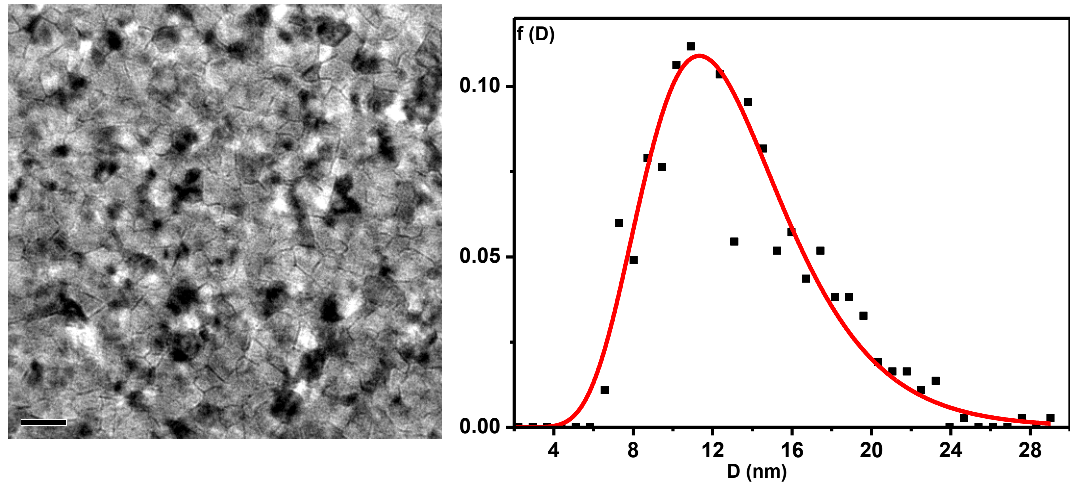

Figure 9.7: BF TEM image and grain size distribution for polycrystalline MnN deposited at V_B = -900V.

The grain size distribution was fitted with a log normal distribution function. The mean grain diameter for the MnN/CoFe polycrystalline system is (12±0.5) nm.

For the AF MnN deposited via HiTUS, the temperature of no thermal activation (T_{NA}) was found to be below room temperature. The controlled thermal activation of the polycrystalline system was performed in accordance to the York protocol and the maximum value for the loop shift (H_{EX}) was observed when the measurement temperature was decreased to 100 K. Figure 9.8 shows the hysteresis loop and thermal activation process for the sample deposited on a Ta seed layer.

As shown in Figure 9.8, the maximum value of H_{EX} is 1.2 kOe at a low temperature of 100K. This result proves that the antiferromagnetic MnN can be easily deposited using the HiTUS system but the thermal stability of the granular AF layer is decreased compared to the material deposited via magnetron sputtering. Comparing the values of the coercive fields corresponding to the systems deposited by HiTUS and magnetron sputtering (Figure 9.4), an increase by a factor 3 is recorded for the thermally unstable AF configuration. The coercivity is also not fully shifted in the

loop shown which may be a sign of thermally active MnN grains which cannot be set at 100K. The anisotropy constant of the AF layer was calculated at 3.1×10^5 ergs/cm^3 which is lower than the value found for the sample deposited by magnetron sputtering (5.1×10^5 ergs/cm^3). The marginal decrease of K_{AF} is attributed to the 15% decrease of the mean grain size on the film deposited via HiTUS and the chemical instability of the compound when post-annealed to increase the crystalline quality of the film.

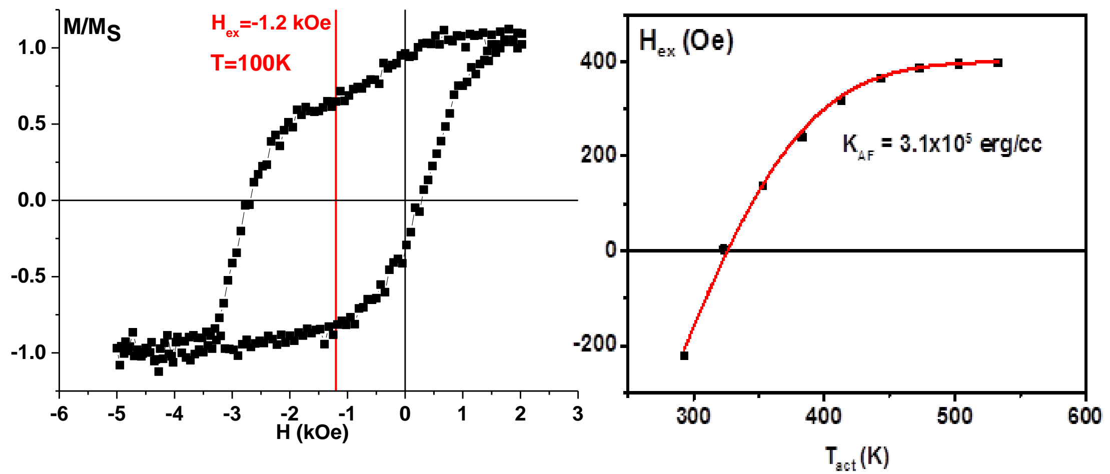

Figure 9.7: York protocol measurements for θ-MnN deposited via HiTUS.

Despite the difference in thermal stability of the two AF MnN/CoFe bilayer samples, the possibility of depositing the new AF material using the HiTUS represents a new potential direction for studying antiferromagnetic compounds. The results presented in this work are intended as a proof of concept. A systematic study of deposition parameters is required in order to optimise the sputtering and annealing conditions for the MnN AF compound deposited via reactive HiTUS.

10 Conclusions and Future Work

10.1 Conclusions

This work is an investigation on antiferromagnetic properties of different alloys and compounds which may replace the commonly used IrMn and PtMn. The AF alloys are used in spintronic devices such as hard disk drive (HDD) read heads and magnetic random access memory (MRAM). For both cases, due to the scarce nature of iridium and platinum and the constantly increasing price of rare metals (especially Ir), a suitable and cost effective replacement is required.

The $IrMn_3$ AF alloy has some distinctive properties which make it the ideal material for usage in nanoelectronic devices. IrMn has outstanding corrosion resistance and can be easily deposited using conventional sputtering techniques. Moreover, the AF alloy does not require post-annealing for crystallisation. IrMn is also known to have one of the highest values of antiferromagnetic anisotropy hence it has superior thermal stability of the AF configuration and induces strong magnetic pinning at the interface with a ferromagnetic (F) layer. Another advantage of the Ir alloy is the decreased minimum required thickness for exchange bias applications (5 to 10 nm) which reduces the overall dimension of a spin valve structure for the nanodevice patterning step.

10.1.1 Polycrystalline Heusler Alloys

This work was focused on the investigation of Heusler alloys which were predicted or reported to have stable AF phases. Among thousands of Heusler alloys and compounds, a number of candidates such as Ni_2MnAl, Fe_2VAl and Ru_2MnGe were chosen for this study.

The main concern when using ternary full-Heusler alloys is the formation of three different crystal phases of the cubic structure depending on the degree of atomic ordering in the unit cell. For the majority of the compositions, the partially ordered *B*2 phase is predicted to induce antiferromagnetism. As shown for Ni_2MnAl and Fe_2VAl prepared using the HiTUS system, the as deposited polycrystalline thin films usually exhibit little or no crystallisation. The XRD analysis reveals the structural properties of the thin films which match the disordered *A*2 phase therefore post-

annealing is required. The partially disordered *B*2 phase is identified by the presence of both the (220) and (200) X-ray diffraction peaks in Ni_2MnAl while the fully disordered *A*2 phase is identified by the appearance of the (220) reflection exclusively in both Ni_2MnAl and Fe_2VAl. The fully ordered $L2_1$ Heusler phase is not identified as the additional (111) superlattice reflection is not observed in the XRD spectrum.

From the experimental point of view, it may difficult to quantify the ratio of the material which crystallises in a certain phase. The crystallographic analysis performed on polycrystalline thin films can be less accurate due to broadening of XRD reflections and low intensity of superlatice peaks. When attempting to induce crystallisation of the intermediate *B*2 Heusler phase via annealing, the formation of the fully ordered $L2_1$ phase may lead to substantial changes in the magnetic characteristics of the Heusler alloy. For both Fe_2VAl and Ni_2MnAl deposited via HiTUS, post-annealing experiments show the transformation of the materials from non-magnetic to ferromagnetic when the post-annealing temperature and the resulting crystalline ordering are increased. For the as-deposited polycrystalline thin films, a crystallisation temperature of 400°C is found for the formation of the *B*2 antiferromagnetic phase. Further increase of the annealing temperature may cause the formation of the highly ordered ferromagnetic phase. The high crystallisation temperature is detrimental for annealing exchange bias bilayer structures. If the ferromagnetic Co_2FeSi Heusler alloy is coupled to Ni_2MnAl, the exchange bias interface includes six different elements which may form a secondary ternary or binary compound. This is usually observed when the saturation magnetisation of samples decreases.

In order to decrease the crystallisation temperature of Heusler alloys, a combination of buffer and seed layers was used. For this work, chromium was used as an adhesion layer deposited on the Si/SiO_2 substrate and a 30 nm thick silver seed layer was used for the growth of Ni_2MnAl. The result is a significant decrease of the crystallisation temperature which becomes 250°C.

Exchange bias measurements performed at 100 K using polycrystalline antiferromagnetic Ni_2MnAl do not show a loop shift but rather a sizeable increase of coercivity is observed. This coincides with the crystallisation of the *B*2 Heusler

phase which may be indicative of low anisotropy exchange coupling where the AF grains are not thermally stable at 100 K. The poor thermal stability of the AF configuration renders the polycrystalline unsuitable for usage in spintronic devices which operate at room temperature.

Polycrystalline Ru_2MnGe was deposited via magnetron sputtering at RT and post annealed using rapid thermal annealing which helps with the crystallisation of the AF $L2_1$ phase. The material requires temperatures lower than 100 K for the thermal stability of the AF configuration. TEM and APT studies have shown that the top half of the 20 nm thick AF Heusler film is oxidised including the exchange bias interface. The origin of the oxidation is unknown.

10.1.2 Epitaxial Heusler Alloys

When depositing epitaxial Ni_2MnAl and Ru_2MnGe via magnetron co-sputtering on heated substrates and annealing the films *in situ* after deposition, the degree of crystallisation hence the phase can be easily controlled.

A 100 nm thick epitaxial Ni_2MnAl was shown to have a stable AF phase and induce exchange bias in a thin neighbouring Fe layer at temperatures lower than100 K. The lack of thermal stability of the AF configuration renders the material unsuitable for use in spintronic applications.

Improved thermal stability of the AF phase in Heusler alloys is observed for epitaxial Ru_2MnGe thin films deposited via magnetron co-sputtering when using a heated substrate, *in-situ* and post annealing. The crystallisation of the AF Ru_2MnGe occurs at 500°C when the fully ordered $L2_1$ AF phase forms. Thermal activation measurements using the York protocol show a blocking temperature of 126 K for epitaxial Ru_2MnGe.

For epitaxial Ni_2MnAl and Ru_2MnGe used in exchange bias systems, the magnetisation reversal mechanism is driven by rapid domain wall motion and the lack of strong domain wall pinning sites contributes to relatively low anisotropic exchange coupling. In the case of Ru_2MnGe, the increased blocking temperature may arise from a slight deformation of the unit cell which is measured as a result of compressive strain induced by the substrate interface.

Epitaxial Ru_2MnGe was succesfuly integrated as an AF layer in magnetic tunnel junctions which show TMR values of up to 135% at low temperatures of 3 and 10 K. Room temperature values of TMR reach 55% for the Ru_2MnGe/Fe/MgO/Fe multilayers which were post annealed at 250°C. The magnetisation reversal mechanism for the patterned specimens after post annealing is dominated by domain wall pinning. This may be a consequence of inducing defects in the multilayer structure via the fabrication steps.

These studies have shown that stable antiferromagnetic phases can be found in epitaxial full Heusler alloys. Exchange bias is observed when using antiferromagnetic alloys such as Ni_2MnAl and Ru_2MnGe but the thermal stability of the AF thin films is inferior when compared to IrMn. Although both Heusler alloys and IrMn crystallise in a cubic structure, the sizeable difference between the antiferromagnetic anisotropy of the two types of materials arises from the crystalline orientation of the compensated spins in the AF unit cell. The large anisotropy of IrMn is induced only when the alloy has a strong (111) out of plane texture becoming a sheet antiferromagnet along the most anisotropic direction of a cubic system. As the cubic symmetry does not allow for enhanced magnetocrystalline anisotropy, thermal instability of the AF configuration is expected for full-Heusler alloys with (110) and (100) texture.

10.1.3 The Tetragonal AF Compound MnN

As demonstrated for cubic systems such as full-Heusler alloys, the antiferromagnetic phases show inferior thermal stability due to the lack of intrinsic magnetocrystalline anisotropy. The next step was to study a naturally anisotropic AF compound such as MnN. For this work, one of the four phases of the compound was deposited using reactive magnetron and HiTUS sputtering. The AF θ-MnN shows a slight tetragonal distortion with a c/a ratio of 1.04 which is enough to considerably increase the magnetocrystalline anisotropy and antiferromagnetic anisotropy constant. This increases considerably the thermal stability of the polycrystalline compound.

The crystallisation of the sought equiatomic θ phase requires the use of a Ta seed layer and post-annealing. Cross-sectional TEM studies confirm the formation of a columnar structure in the MnN/CoFe polycrystalline bilayers with a mixed interface

between MnN and Ta seed layer which is considered responsible for the formation of the stable AF phase.

Polycrystalline MnN/CoFe bilayers deposited via magnetron sputtering show a large value of exchange bias of 1.4 kOe after field cooling while from York protocol measurements, the blocking temperature is determined to be 388 K. These parameters are sufficient for meeting the requirements for strong magnetic pinning as required in spintronic applications. There is however a drawback when considering the overall thickness of the antiferromagnet and seed layer system. MnN requires a minimum thickness of 30 nm for thermal stability and a 10 nm thick Ta seed layer for crystallisation. These dimensions are about a factor four larger than what the industry uses currently and due to limitations concerning the lateral bit size in a hard disk drive and defects induced via patterning in devices such as MRAM cells, the overall thickness of the AF layer needs to be reduced. The electrical resistance of MnN thin films may also be an issue when trying to integrate the compound in GMR and TMR devices resulting in a large resistance area product.

In conclusion, this work described the process of synthesising and characterisation of novel antiferromagnetic thin films with applications in spintronic devices. Although antiferromagnetism can be relatively easily identified, engineering a suitable and cost effective AF thin film is non-trivial.

10.2 Future Work

In order to successfully deposit antiferromagnetic Heusler alloy thin films, precise control of the stoichiometry is required. Although doping experiments were conducted for this work, quantification of the results has proven difficult. Magnetron co-sputtering is likely to be the most efficient way of controlling the composition of thin films and also deposit off-stoichiometric compositions when required. When measuring the chemical composition of thin films using energy dispersive X-ray spectroscopy, the penetration depth of the electron beam exceeds the thickness of the film. The results are therefore dominated by the signal coming from the substrate and the error in determining the atomic ratio of an alloy or compound is large. A more surface sensitive technique such as X-ray fluorescence (XRF) or X-ray

photoemission spectroscopy (XPS) may be more suitable for chemical analysis of ternary Heusler alloys.

The growth and post-annealing of polycrystalline exchange biases multilayer structures deposited via HiTUS such as Cr/Ag/Ni_2MnAl/Co_2FeSi may benefit if a heated substrate stage is used. This would allow for intermediary annealing or high temperature deposition steps. As exchange bias interfaces need to be sharp, the post-annealing step could be avoided. Moreover, when the AF Heusler alloys can be deposited at elevated temperatures to promote crystallisation, the ferromagnetic layer can be deposited at room temperature hence minimising the mixing at the exchange coupled interface.

Deposition using a heated substrate was used for epitaxial Ni_2MnAl and Ru_2MnGe resulting in highly crystalline epitaxial structures which exhibit stable antiferromagnetism at low temperatures. In order to increase the anisotropy of large grain epitaxial thin films, doping or induced defects were shown to act as strong domain wall pinning sites acting on the reversal mechanism in the antiferromagnet. Doping a small percentage (1-2%) of insoluble metal such as Cu into the epitaxial structures may result in an increase of the thermal stability of the epitaxial AF alloys. There is however a limit to the amount of doping which increases the number of pinning sites which is reached when the interstitial atoms or vacancies break the long range symmetry of the material affecting the antiferromagnetic structure.

Another method of improving the antiferromagnetic anisotropy of cubic systems is by inducing a tetragonal distortion of the unit cell using dopants or strain induced via the substrate or seed layer interface.

For the anisotropic tetragonal AF MnN, an extensive investigation of substrates, seed layers, deposition conditions and dopants may result in decreasing the overall thickness of the material needed while still maintaining thermal stability. In order to test the conductivity of the anisotropic MnN, GMR and TMR structures could be deposited on Si/SiO_2. The material is expected to induce strong magnetic pinning at room temperature.

List of symbols

$<T_B>$	*Median blocking temperature*
A_1, A_2, A_3	*Astigmatism orders in electromagnetic lens*
A2	*Fully disordered Heusler structure*
A_c	*Area of the coil*
A_{ex}	*Exchange stiffness constant*
Ar^+	*Argon ion*
$\boldsymbol{B}$	*Magnetic flux*
B2	*Partially disordered Heusler structure*
C	*Generic constant*
C_S	*Aberrations in electromagnetic lens*
D	*Particle or crystalline grain diameter*
d	*Interplanar spacing*
d_e	*Distance between electrons*
d_{ele}	*Distance between electrodes*
D_T	*Magnetic domain thickness*
e	*Base of natural logarithm*
E_{ex}	*Exchange energy*
E_F	*Fermi level (energy)*
E_K	*Anisotropy energy*
E_{ms}	*Magnetostatic energy*
E_T	*Total energy*
E_x	*X-ray energy*
E_Z	*Zeeman energy*
f_0	*Oscillation attempt frequency of magnetic moment*
H^*	*Exchange field from ferromagnet*
h, k, l	*Miller indices*
H_C	*Coercive field*
H_D	*Demagnetising field*
H_{EX}	*Exchange bias field*
H_K	*Anisotropy field*
H_K^*	*Pseud- anisotropy field in antiferromagnets*

$\boldsymbol{H}_m$	*Molecular field vector*
H_n	*Normalised field*
I	*Electrical current*
I_0	*Photoelectric current*
J_c	*Write current density*
J_{ex}	*Exchange integral*
K	*Anisotropy constant*
K, L, M	*Electronic shells*
K_{AF}	*Antiferromagnetic anisotropy constant*
k_B	*Boltzmann constant*
K_U	*Uniaxial anisotropy*
K_x	*Scattering vector in X-ray diffraction*
$L2_1$	*Completely ordered full Heusler structure*
L_c	*Camera focal length (TEM)*
m	*Magnetic moment*
$\boldsymbol{M}$	*Magnetisation vector*
m_e	*Mass of the electron*
M_n	*Normalised magnetisation*
M_S	*Saturation magnetisation*
m_{uc}	*Magnetic moment of a unit cell*
N	*Number of turns for a coil*
N_2^+	*Nitrogen ion*
$N_{majority}$	*Number of electrons in the majority spin channel*
$N_{minority}$	*Number of electrons in the minority spin channel*
n_r	*Refractive index*
N_V	*Number of valence electrons per unit cell*
N_{Vat}	*Number of valence electrons for individual atoms*
P_{AF}	*Saturation value of antiferromagnetic ordering*
P_F	*Spin polarisation parameter*
q_e	*Charge of the electron*
R	*Electrical resistance*
$R\uparrow$	*Resistance of the up spin channel*
$R\downarrow$	*Resistance of the down spin channel*

r_a	*Atomic radius*
R_{AP}	*Resistance for antiparallel configuration in GMR*
r_c	*Critical radius for single domain particle*
R_d	*Distance between diffraction spots*
r_d	*Radius of the d electronic shell*
R_L	*Larmour rotation radius*
R_{nn}	*Nearest neighbour atomic distance*
R_P	*Resistance for parallel configuration in GMR*
$S(H)$	*Magnetic viscosity coefficient*
S_i, S_j	*Spin angular momentum*
T	*Temperature*
t	*time*
T_{ACT}	*Activation temperature*
t_{ACT}	*Activation time*
t_{AF}	*Thickness of antiferromagnetic film*
T_B	*Blocking temperature*
T_C	*Curie temperature*
T_{ms}	*Measurement temperature*
t_{ms}	*Measurement time*
T_N	*Néel temperature*
T_{NA}	*Temperature of non-activation*
T_{SET}	*Setting temperature*
t_{SET}	*Setting temperature*
t_x	*Penetration depth of X-rays*
V	*Volume of particle (grain)*
V_{ACT}	*Activation volume*
V_B	*Bias voltage*
V_C	*Critical grain volume for thermal stability*
v_e	*Velocity of the electron*
V_{med}	*Median grain volume*
V_{SET}	*Critical grain volume for field setting*
Z	*Atomic number*
α	*Sample tilt angle*

α_d	*Spin damping parameter*
α_T	*First Townsend ionisation coefficient*
β	*Sample rotation angle*
γ_m	*Molecular field coefficient*
ΔE	*Energy barrier to reversal*
ΔE_C	*Critical activation energy*
δ_{min}	*Minimum distance resolved in TEM*
ΔR	*Resistance difference*
θ	*Incident angle of X-rays*
Θ	*Semiangle of collection for electromagnetic lens*
λ	*Wavelength*
λ_e	*Wavelength of electrons*
μ_B	*Bohr magneton*
μ_x	*Linear absorption coefficient of X-rays*
τ	*Magnetisation decay time*
φ	*Sample rotation angle (XRD)*
φ_c	*Total flux passing through a coil*
ϕ_{ij}	*Angle between neighbouring spins*
χ	*Magnetic susceptibility*
χ_x	*In plane X-ray detector angle*
ω	*Rocking curve angle (XRD)*
ω_L	*Larmour rotation frequency*

List of abbreviations

AC	*Alternating current*
AES	*Auger electron spectroscopy*
AF	*Antiferromagnet(ic)*
AGFM	*Alternating gradient force magnetometer*
AMR	*Anisotropic magnetoresistance*
APT	*Atom probe tomography*
bcc	*Body centred cubic*
BF	*Bright field TEM image*
BL	*Bit line*
CIP	*Current in plane configuration*
CMOS	*Complementary metal-oxide-semiconductor transistor*
CPP	*Current perpendicular to plane configuration*
CVD	*Chemical Vapour Deposition*
DC	*Direct Current*
DF	*Dark field (TEM)*
DOS	*Density of states*
DSP	*Digital signal processing*
EDS	*Energy dispersive spectroscopy*
EDX	*Energy Dispersive X-ray spectroscopy*
EELS	*Electron energy loss spectroscopy*
emf	*Electromotive force*
F	*Ferromagnet(ic)*
f.u.	*Formula unit*
FIB	*Focused ion beam*
FWHM	*Full width at half maximum*
GMR	*Giant magnetoresistance*
HA(s)	*Heusler alloy(s)*
HAADF	*High angle annular dark field (TEM)*
HDD(s)	*Hard disk drive(s)*
HiTUS	*High Target Utilisation Sputtering*
HR	*High resolution*
iMTJ	*In plane magnetised MTJ*

iPVD	*Ionised physical vapour deposition*
LEAP	*Local electrode atom probe tomography*
LMIS	*Liquid metal ion source*
MBE	*Molecular beam epitaxy*
MR	*Magnetoresistance*
MRAM	*Magnetic random access memory*
MTJ	*Magnetic tunnel junction*
NA	*Numerical aperture*
PLD	*Pulsed laser deposition*
pMTJ	*Perpendicular magnetised MTJ*
PVD	*Physical Vapour Deposition*
RA	*Resistance area product*
RC	*Resistor capacitor circuit*
RF	*Radio frequency*
RKKY	*Indirect exchange coupling*
RTA	*Rapid thermal annealing*
SAF	*Synthetic antiferromagnet*
SEM	*Scanning electron microscope*
SNR	*Signal to noise ratio*
STEM	*Scanning tunnelling electron microscopy*
STT	*Spin transfer torque*
TEM	*Transmission electron microscope*
TMR	*Tunnelling magnetoresistance*
UHV	*Ultra-high vacuum*
VSM	*Vibrating sample magnetometer*
WL	*Word line*
CGR	*Compound growth rate*
PRML	*Partial-response maximum-likelihood*
AFC	*Antiferromagnetically coupled*
PRM	*Perpendicular recording media*
TFC	*Thermal flying-height control (HDD read head)*
LDPC	*Low-density parity-check (error correcting)*
SMR	*Shingled magnetic recording*

MAMR	*Microwave assisted magnetic recording*
TAR	*Thermally-assisted recording*
BPR	*Bit patterned recording*
TDMR	*Two dimensional magnetic recording*

References

[1] G. Binasch, P. Grünberg, F. Saurenbach, and W. Zinn, "Enhanced magnetoresistance in layered magnetic structures with antiferromagnetic interlayer exchange," *Physical Review B,* vol. 39, no. 7, pp. 4828-4830, 03/01/ 1989.

[2] M. N. Baibich *et al.*, "Giant Magnetoresistance of (001)Fe/(001)Cr Magnetic Superlattices," *Physical Review Letters,* vol. 61, no. 21, pp. 2472-2475, 11/21/ 1988.

[3] J. R. Childress and R. E. Fontana, "Magnetic recording read head sensor technology," *Comptes Rendus Physique,* vol. 6, no. 9, pp. 997-1012, 2005/11/01 2005.

[4] S. Mao, "Message From the Conference Chair," *IEEE Transactions on Magnetics,* vol. 42, no. 2, pp. 91-91, 2006.

[5] S. Yuasa and D. D. Djayaprawira, "Giant tunnel magnetoresistance in magnetic tunnel junctions with a crystalline MgO(0 0 1) barrier," *Journal of Physics D: Applied Physics,* vol. 40, no. 21, p. R337, 2007.

[6] J. C. Slonczewski, "Current-driven excitation of magnetic multilayers," *Journal of Magnetism and Magnetic Materials,* vol. 159, no. 1, pp. L1-L7, 1996/06/01 1996.

[7] L. Berger, "Emission of spin waves by a magnetic multilayer traversed by a current," *Physical Review B,* vol. 54, no. 13, pp. 9353-9358, 10/01/ 1996.

[8] S.-W. Chung. (2016). *4Gbit Density STT-MRAM using Perpendicular MTJ Realized with Compact Cell Structure*. Available: http://ieee-iedm.org/session-27-memory-technology-mram/

[9] K. L. Wang, J. G. Alzate, and P. K. Amiri, "Low-power non-volatile spintronic memory: STT-RAM and beyond," *Journal of Physics D: Applied Physics,* vol. 46, no. 7, p. 074003, 2013.

[10] N. P. Aley *et al.*, "Texture Effects in IrMn/CoFe Exchange Bias Systems," *IEEE Transactions on Magnetics,* vol. 44, no. 11, pp. 2820-2823, 2008.

[11] "26 - Cobalt, Rhodium and Iridium," in *Chemistry of the Elements (Second Edition)*Oxford: Butterworth-Heinemann, 1997, pp. 1113-1143.

[12] H. Renner *et al.*, "Platinum Group Metals and Compounds," in *Ullmann's Encyclopedia of Industrial Chemistry*: Wiley-VCH Verlag GmbH & Co. KGaA, 2000.

[13] (24.02.2017). *Iridium Demand*. Available: http://www.platinum.matthey.com/documents/market-data-tables/iridium/pdf-2005-to-2013-.pdf

[14] J. R. Handley, "Increasing Applications for Iridium," *Platinum Metals Rev.,* vol. 30, no. 1, p. 12, 1986.

[15] M. Graff, B. Kempf, and J. Breme, "Iridium Alloy for Spark Plug Electrodes," in *Materials for Transportation Technology*: Wiley-VCH Verlag GmbH & Co. KGaA, 2005, pp. 1-8.

[16] X. Yang, D. Neher, D. Hertel, and T. K. Däubler, "Highly Efficient Single-Layer Polymer Electrophosphorescent Devices," *Advanced Materials,* vol. 16, no. 2, pp. 161-166, 2004.

[17] (24.02.2017). *Current Iridium Prices*. Available: https://www.quandl.com/collections/markets/rare-metals

[18] (2002). *Rare Earth Elements—Critical Resources for High Technology*. Available: https://pubs.usgs.gov/fs/2002/fs087-02/fs087-02.pdf

[19] C. X. Ji *et al.*, "An investigation of phase transformation behavior in sputter-deposited PtMn thin films," *JOM,* vol. 58, no. 6, pp. 50-54, 2006.

[20] I. Galanakis and P. H. Dederichs, *Half-metallic alloys : fundamentals and applications* (Lecture notes in physics;676). Berlin: Springer, 2005.

[21] X. Y. Dong *et al.*, "Growth temperature controlled magnetism in molecular beam epitaxially grown Ni_2MnAl Heusler alloy," *Journal of Crystal Growth,* vol. 254, no. 3–4, pp. 384-389, 7 2003.

[22] N. Fukatani, H. Fujita, T. Miyawaki, K. Ueda, and H. Asano, "Structural and magnetic properties of antiferromagnetic Heusler Ru2MnGe Epitaxial thin films," *Journal of the Korean Physical Society,* vol. 63, no. 3, pp. 711-715, 2013// 2013.

[23] F. Heusler, *Verh. Dtsch. Phys. Ges.,* Article vol. 5, p. 219, 1903.

[24] J. H. Wernick, G. W. Hull, T. H. Geballe, J. E. Bernardini, and J. V. Waszczak, "Superconductivity in ternary Heusler intermetallic compounds," *Materials Letters,* Article vol. 2, no. 2, pp. 90-92, 1983.

[25] M. König *et al.*, "Quantum spin hall insulator state in HgTe quantum wells," *Science,* Article vol. 318, no. 5851, pp. 766-770, 2007.

[26] Y. Nishino, M. Kato, S. Asano, K. Soda, M. Hayasaki, and U. Mizutani, "Semiconductorlike behavior of electrical resistivity in Heusler-type Fe_2VAl compound," *Physical Review Letters,* vol. 79, no. 10, pp. 1909-1912, 1997.

[27] P. G. van Engen, K. H. J. Buschow, and M. Erman, "Magnetic properties and magneto-optical spectroscopy of Heusler alloys based on transition metals and Sn," *Journal of Magnetism and Magnetic Materials,* Article vol. 30, no. 3, pp. 374-382, 1983.

[28] T. Krenke *et al.*, "Inverse magnetocaloric effect in ferromagnetic Ni-Mn-Sn alloys," *Nature Materials,* Article vol. 4, no. 6, pp. 450-454, 2005.

[29] S. Wurmehl, H. C. Kandpal, G. H. Fecher, and C. Felser, "Valence electron rules for prediction of half-metallic compensated- ferrimagnetic behaviour of Heusler compounds with complete spin polarization," *Journal of Physics Condensed Matter,* Article vol. 18, no. 27, pp. 6171-6181, 2006, Art. no. 001.

[30] O. Heusler, "Kristallstruktur und Ferromagnetismus der Mangan-Aluminium-Kupferlegierungen," *Annalen der Physik,* Article vol. 411, no. 2, pp. 155-201, 1934.

[31] A. J. Bradley and J. W. Rodgers, "The Crystal Structure of the Heusler Alloys," *Proceedings of the Royal Society A: Mathematical, Physical and Engineering Sciences,* Article vol. 144, no. 852, 1934.

[32] T. Graf, C. Felser, and S. S. P. Parkin, "Simple rules for the understanding of Heusler compounds," *Progress in Solid State Chemistry,* vol. 39, no. 1, pp. 1-50, 5// 2011.

[33] C. e. Felser and A. e. Hirohata, *Heusler Alloys Properties, Growth, Applications*, 1st ed. 2016. ed. 2016.

[34] G. E. Bacon and J. S. Plant, "Chemical ordering in Heusler alloys with the general formula A 2BC or ABC," *Journal of Physics F: Metal Physics,* vol. 1, no. 4, pp. 524-532, 1971, Art. no. 325.

[35] L. Ma *et al.*, "Martensitic and magnetic transformation in $Mn_{50}Ni_{50-x}Sn_x$ ferromagnetic shape memory alloys," *Journal of Applied Physics,* vol. 112, no. 8, p. 083902, 2012.

[36] T. Graf, F. Casper, J. Winterlik, B. Balke, G. H. Fecher, and C. Felser, "Crystal structure of new heusler compounds," *Zeitschrift fur Anorganische und Allgemeine Chemie,* Article vol. 635, no. 6-7, pp. 976-981, 2009.

[37] P. J. Webster and K. R. A. Ziebeck, *Landolt-Börnstein-Group III Condensed Matter,* Article vol. 19, 1988.

[38] I. Galanakis, P. H. Dederichs, and N. Papanikolaou, "Slater-Pauling behavior and origin of the half-metallicity of the full-Heusler alloys," *Physical Review B - Condensed Matter and Materials Physics,* Article vol. 66, no. 17, pp. 1744291-1744299, 2002, Art. no. 174429.

[39] D. Brown *et al.*, "Photoelectron spectroscopy of manganese-based Heusler alloys," *Physical Review B,* vol. 57, no. 3, pp. 1563-1571, 01/15/ 1998.

[40] J. Sagar, "Optimisation of Heusler Alloy Thin Films for Spintronic Devices," PhD, University of York, 2013.

[41] J. C. Slater, "The ferromagnetism of nickel," *Physical Review,* Article vol. 49, no. 7, pp. 537-545, 1936.

[42] L. Pauling, "The nature of the interatomic forces in metals," *Physical Review,* Article vol. 54, no. 11, pp. 899-904, 1938.

[43] J. Kübler, *Theory of Itinerant Electron Magnetism,* Article 2000.

[44] S. Wurmehl *et al.*, "Geometric, electronic, and magnetic structure of Co_2FeSi: Curie temperature and magnetic moment measurements and calculations," *Physical Review B* vol. 72, no. 18, 2005, Art. no. 184434.

[45] R. Weht and W. E. Pickett, "Half-metallic ferrimagnetism in Mn_2VAl," *Physical Review B - Condensed Matter and Materials Physics,* Article vol. 60, no. 18, pp. 13006-13010, 1999.

[46] F. J. Yang, C. Wei, and X. Q. Chen, "Half-metallicity and anisotropic magnetoresistance of epitaxial Co_2FeSi Heusler films," *Applied Physics Letters,* vol. 102, no. 17, p. 172403, 2013.

[47] J. Kübler, A. R. William, and C. B. Sommers, "Formation and coupling of magnetic moments in Heusler alloys," *Physical Review B,* Article vol. 28, no. 4, pp. 1745-1755, 1983.

[48] R. A. de Groot, "Half-metallic magnetism in the 1990s," *Physica B: Physics of Condensed Matter,* Article vol. 172, no. 1-2, pp. 45-50, 1991.

[49] T. Jungwirth, X. Marti, P. Wadley, and J. Wunderlich, "Antiferromagnetic spintronics," *Nat Nano,* Review vol. 11, no. 3, pp. 231-241, 03//print 2016.

[50] L. Neel, "Magnetism and the local molecular field," *Nobel Lectures, Physics 1963-1970,* // 1970.

[51] W. H. Meiklejohn and C. P. Bean, "New magnetic anisotropy," *Phys. Rev.,* 10.1103/PhysRev.102.1413 vol. 102, pp. 1413-1414, // 1956.

[52] D. P. Oxley, R. S. Tebble, C. T. Slack, and K. C. Williams, "An anti-ferromagnetic heusler alloy, Cu2MnSb," *Nature,* Article vol. 194, no. 4827, p. 465, 1962.

[53] T. Kanomata, M. Kikuchi, H. Yamauchi, and T. Kaneko, "Magnetic properties of new heusler alloys Ru_2Mnz (Z=Si, Ge, Sn and Sb)," *Japanese Journal of Applied Physics,* Article vol. 32, no. S3, pp. 292-293, 1993.

[54] K. U. Neumann, J. Crangle, R. K. Kremer, N. K. Zayer, and K. R. A. Ziebeck, "Magnetic order in Pd_2TiIn: A new itinerant antiferromagnet?," *Journal of Magnetism and Magnetic Materials,* Article vol. 127, no. 1-2, pp. 47-51, 1993.

[55] T. Moriya, "Spin Fluctuations in Itinerant Electron Magnetism," *Springer Series in Solid-State Sciences,* vol. 56, 1985.

[56] E. Popiel, M. Tuszyński, W. Zarek, and T. Rendecki, "Investigation of $Fe_{3-x}V_xAl$ alloys with DO3 type structure by X-ray, magnetostatic and

Mössbauer effect methods," *Journal of the Less Common Metals,* vol. 146, pp. 127-135, 1989/01/01 1989.
[57] C. Venkatesh, V. Srinivas, V. V. Rao, S. K. Srivastava, and P. S. Babu, "Effect of site disorder on the electronic properties of Fe_2VAl Heusler alloy," *Journal of Alloys and Compounds,* vol. 577, pp. 417-425, 11/15/ 2013.
[58] D. J. Singh and I. I. Mazin, "Electronic structure, local moments, and transport in Fe2VA1," *Physical Review B - Condensed Matter and Materials Physics,* Article vol. 57, no. 22, pp. 14352-14356, 1998.
[59] Y. Feng *et al.*, "Physical properties of Heusler-like Fe_2VAl," *Physical Review B,* vol. 63, no. 16, p. 165109, 04/04/ 2001.
[60] M. Acet, E. Duman, E. F. Wassermann, L. Mañosa, and A. Planes, "Coexisting ferro- and antiferromagnetism in Ni_2MnAl Heusler alloys," *Journal of Applied Physics,* vol. 92, no. 7, pp. 3867-3871, 2002.
[61] M. Kawakami, K. Yamaguchi, and T. Shinohara, *J. Phys. Soc. Jpn.,* vol. 68, p. 2128, 1999.
[62] K. Endo, H. Matsuda, K. Ooiwa, and K. Itoh, "Antiferromagnetism in a Heusler Alloy Fe_2VSi," *Journal of the Physical Society of Japan,* Article vol. 64, no. 7, pp. 2329-2332, 1995.
[63] C. S. Lue, Y. K. Kuo, S. N. Hong, S. Y. Peng, and C. Cheng, *Phys. Rev. B,* vol. 71, p. 064202, 2005.
[64] N. Fukatani, K. Ueda, and H. Asano, "Epitaxial strain and antiferromagnetism in Heusler Fe_2VSi thin films," *Journal of Applied Physics,* vol. 109, no. 7, p. 073911, 2011.
[65] S. Ishida, S. Kashiwagi, S. Fujii, and S. Asano, "Magnetic and half-metallic properties of new Heusler alloys Ru_2MnZ (Z : Si, Ge, Sn and Sb)," *Physica B: Condensed Matter,* vol. 210, no. 2, pp. 140-148, 1995/04/02 1995.
[66] M. Gotoh, M. Ohashi, T. Kanomata, and Y. Yamaguchi, "Spin reorientation in the new Heusler alloys Ru_2MnSb and Ru_2MnGe," *Physica B: Condensed Matter,* vol. 213, pp. 306-308, 1995/08/01 1995.
[67] W. Thomson, "On the Electro-Dynamic Qualities of Metals:--Effects of Magnetization on the Electric Conductivity of Nickel and of Iron," *Proceedings of the Royal Society of London,* vol. 8, pp. 546-550, January 1, 1856 1856.
[68] T. McGuire and R. Potter, "Anisotropic magnetoresistance in ferromagnetic 3D alloys," *IEEE Trans. Magn.,* 10.1109/TMAG.1975.1058782 vol. 11, pp. 1018-1038, // 1975.
[69] I. A. Campbell and A. Fert, "Chapter 9 Transport properties of ferromagnets," in *Handbook of Ferromagnetic Materials*, vol. Volume 3: Elsevier, 1982, pp. 747-804.
[70] W. Gerlach, "Ferromagnetismus und elektrische Eigenschaften IV. Mitteilung," *Annalen der Physik,* vol. 404, no. 7, pp. 849-864, 1932.
[71] H. H. Potter, "On the Change of Resistance of Nickel in a Magnetic Field," *Proceedings of the Royal Society of London. Series A,* vol. 132, no. 820, pp. 560-569, 1931.
[72] N. F. Mott, "The Electrical Conductivity of Transition Metals," *Proceedings of the Royal Society of London. Series A - Mathematical and Physical Sciences,* vol. 153, no. 880, pp. 699-717, 1936.
[73] A. Fert and I. A. Campbell, "Two-Current Conduction in Nickel," *Physical Review Letters,* vol. 21, no. 16, pp. 1190-1192, 10/14/ 1968.

[74] A. Fert and I. A. Campbell, "Electrical resistivity of ferromagnetic nickel and iron based alloys," *Journal of Physics F: Metal Physics,* vol. 6, no. 5, p. 849, 1976.

[75] M. T. Sarah, "The discovery, development and future of GMR: The Nobel Prize 2007," *Journal of Physics D: Applied Physics,* vol. 41, no. 9, p. 093001, 2008.

[76] J. F. Gregg, I. Petej, E. Jouguelet, and C. Dennis, "Spin electronics—a review," *Journal of Physics D: Applied Physics,* vol. 35, no. 18, p. R121, 2002.

[77] B. Dieny *et al.*, "Spin-valve effect in soft ferromagnetic sandwiches," *Journal of Magnetism and Magnetic Materials,* vol. 93, pp. 101-104, 1991/02/01 1991.

[78] B. Dieny, V. S. Speriosu, S. S. P. Parkin, B. A. Gurney, D. R. Wilhoit, and D. Mauri, "Giant magnetoresistive in soft ferromagnetic multilayers," *Physical Review B,* vol. 43, no. 1, pp. 1297-1300, 01/01/ 1991.

[79] B. Dieny, "Giant magnetoresistance in spin-valve multilayers," *Journal of Magnetism and Magnetic Materials,* vol. 136, no. 3, pp. 335-359, 1994/09/02 1994.

[80] B. Dieny *et al.*, "Magnetotransport properties of magnetically soft spin-valve structures (invited)," *Journal of Applied Physics,* vol. 69, no. 8, pp. 4774-4779, 1991.

[81] A. Chaiken, P. Lubitz, J. J. Krebs, G. A. Prinz, and M. Z. Harford, "Low-field spin-valve magnetoresistance in Fe-Cu-Co sandwiches," *Applied Physics Letters,* vol. 59, no. 2, pp. 240-242, 1991.

[82] H. N. Fuke, K. Saito, Y. Kamiguchi, H. Iwasaki, and M. Sahashi, "Spin-valve giant magnetoresistive films with antiferromagnetic Ir-Mn layers," *Journal of Applied Physics,* vol. 81, no. 8, pp. 4004-4006, 1997.

[83] K. O'Grady, L. E. Fernandez-Outon, and G. Vallejo-Fernandez, "A new paradigm for exchange bias in polycrystalline thin films," *Journal of Magnetism and Magnetic Materials,* vol. 322, no. 8, pp. 883-899, 4// 2010.

[84] T. M. Nakatani, N. Hase, H. S. Goripati, Y. K. Takahashi, T. Furubayashi, and K. Hono, "Co-Based Heusler Alloys for CPP-GMR Spin-Valves With Large Magnetoresistive Outputs," *IEEE Transactions on Magnetics,* vol. 48, no. 5, pp. 1751-1757, 2012.

[85] M. Andreas *et al.*, "Magnetic recording: advancing into the future," *Journal of Physics D: Applied Physics,* vol. 35, no. 19, p. R157, 2002.

[86] HGST. (2007, 5.03). *Prependicular Magnetic Recording Technology*. Available: https://www.hgst.com/sites/default/files/resources/PMR_white_paper_final.pdf

[87] J. Chureemart, "Orientation and Thermal Stability of Advanced Recording Media " PhD, University of York, 2013.

[88] L. Berger, "Emission of spin waves by a magnetic multilayer traversed by a current," *Physical Review B - Condensed Matter and Materials Physics,* Article vol. 54, no. 13, pp. 9353-9358, 1996.

[89] J. C. Slonczewski, "Current-driven excitation of magnetic multilayers," *Journal of Magnetism and Magnetic Materials,* Article vol. 159, no. 1-2, 1996.

[90] J. A. Katine, F. J. Albert, R. A. Buhrman, E. B. Myers, and D. C. Ralph, "Current-Driven Magnetization Reversal and Spin-Wave Excitations in

Co/Cu /Co Pillars," *Physical Review Letters,* vol. 84, no. 14, pp. 3149-3152, 04/03/ 2000.

[91] S. Petit, F. Moussa, M. Hennion, S. Pailhès, L. Pinsard-Gaudart, and A. Ivanov, "Spin Phonon Coupling in Hexagonal Multiferroic $YMnO_3$," *Physical Review Letters,* vol. 99, no. 26, p. 266604, 12/28/ 2007.

[92] A. Hirohata and K. Takanashi, "Future perspectives for spintronic devices," *Journal of Physics D: Applied Physics,* vol. 47, no. 19, p. 193001, 2014.

[93] M. Julliere, "Tunneling between ferromagnetic films," *Physics Letters A,* Article vol. 54, no. 3, pp. 225-226, 1975.

[94] T. Miyazaki and N. Tezuka, "Giant magnetic tunneling effect in $Fe/Al_2O_3/Fe$ junction," *Journal of Magnetism and Magnetic Materials,* vol. 139, no. 3, pp. L231-L234, 1995/01/02 1995.

[95] J. S. Moodera, L. R. Kinder, T. M. Wong, and R. Meservey, "Large Magnetoresistance at Room Temperature in Ferromagnetic Thin Film Tunnel Junctions," *Physical Review Letters,* vol. 74, no. 16, pp. 3273-3276, 04/17/ 1995.

[96] D. J. Monsma and S. S. P. Parkin, "Spin polarization of tunneling current from ferromagnet/Al_2O_3 interfaces using copper-doped aluminum superconducting films," *Applied Physics Letters,* vol. 77, no. 5, pp. 720-722, 2000.

[97] W. H. Butler, X. G. Zhang, T. C. Schulthess, and J. M. MacLaren, "Spin-dependent tunneling conductance of Fe/MgO/Fe sandwiches," *Physical Review B* vol. 63, no. 5, 2001, Art. no. 054416.

[98] J. Mathon and A. Umerski, "Theory of tunneling magnetoresistance of an epitaxial Fe/MgO/Fe(001) junction," *Physical Review B - Condensed Matter and Materials Physics,* Article vol. 63, no. 22, pp. 2204031-2204034, 2001, Art. no. 220403.

[99] S. S. P. Parkin *et al.*, "Giant tunnelling magnetoresistance at room temperature with MgO (100) tunnel barriers," *Nature Materials,* Article vol. 3, no. 12, pp. 862-867, 2004.

[100] D. D. Djayaprawira *et al.*, "230% room-temperature magnetoresistance in CoFeB∕MgO∕CoFeB magnetic tunnel junctions," *Applied Physics Letters,* vol. 86, no. 9, p. 092502, 2005.

[101] J. Hayakawa, S. Ikeda, F. Matsukura, S. Takahashi, and H. Ohno, "Dependence of Giant Tunnel Magnetoresistance of Sputtered CoFeB/MgO/CoFeB Magnetic Tunnel Junctions on MgO Barrier Thickness and Annealing Temperature," *Japanese Journal of Applied Physics,* vol. 44, no. 4L, p. L587, 2005.

[102] S. Ikeda *et al.*, "Tunnel magnetoresistance of 604% at 300K by suppression of Ta diffusion in CoFeB∕MgO∕CoFeB pseudo-spin-valves annealed at high temperature," *Applied Physics Letters,* vol. 93, no. 8, p. 082508, 2008.

[103] T. Kawahara, K. Ito, R. Takemura, and H. Ohno, "Spin-transfer torque RAM technology: Review and prospect," *Microelectronics Reliability,* vol. 52, no. 4, pp. 613-627, 4// 2012.

[104] M. Yoshikawa *et al.*, "Tunnel Magnetoresistance Over 100% in MgO-Based Magnetic Tunnel Junction Films With Perpendicular Magnetic $L1_0$-FePt Electrodes," *IEEE Transactions on Magnetics,* vol. 44, no. 11, pp. 2573-2576, 2008.

[105] Y. Kay *et al.*, "High Magnetoresistance Ratio and Low Resistance–Area Product in Magnetic Tunnel Junctions with Perpendicularly Magnetized Electrodes," *Applied Physics Express,* vol. 3, no. 5, p. 053003, 2010.

[106] S. Ikeda *et al.*, "A perpendicular-anisotropy CoFeB–MgO magnetic tunnel junction," *Nat Mater,* 10.1038/nmat2804 vol. 9, no. 9, pp. 721-724, 09//print 2010.

[107] T. Kawahara, M. Horiguchi, Y. Kawajiri, G. Kitsukawa, T. Kure, and M. Aoki, "Subthreshold current reduction for decoded-driver by self-reverse biasing [DRAMs]," *IEEE Journal of Solid-State Circuits,* vol. 28, no. 11, pp. 1136-1144, 1993.

[108] A. P. Chandrakasan, S. Sheng, and R. W. Brodersen, "Low-power CMOS digital design," *IEEE Journal of Solid-State Circuits,* vol. 27, no. 4, pp. 473-484, 1992.

[109] Y. Nakagome, M. Horiguchi, T. Kawahara, and K. Itoh, "Review and future prospects of low-voltage RAM circuits," *IBM Journal of Research and Development,* vol. 47, no. 5.6, pp. 525-552, 2003.

[110] W. Zhi Gang and Y. Nakamura, "Spin tunneling random access memory (STram)," *IEEE Transactions on Magnetics,* vol. 32, no. 5, pp. 4022-4024, 1996.

[111] J. M. Daughton, "Magnetic tunneling applied to memory (invited)," *Journal of Applied Physics,* vol. 81, no. 8, pp. 3758-3763, 1997.

[112] S. Yakata *et al.*, "Enhancement of Thermal Stability Using Ferromagnetically Coupled Synthetic Free Layers in MgO-Based Magnetic Tunnel Junctions," *IEEE Transactions on Magnetics,* vol. 46, no. 6, pp. 2232-2235, 2010.

[113] B. Dieny, "MRAM 2," in *InMram Grenoble Summer School*, ed, 2013.

[114] S. Zhuiykov *et al.*, "Atomic layer deposition-enabled single layer of tungsten trioxide across a large area," *Applied Materials Today,* vol. 6, pp. 44-53, 3// 2017.

[115] R. O'Handley, *Modern Magnetic Materials: Principles and Applications* New York: Wiley, 2000.

[116] B. D. Cullity and C. D. Graham, *Introduction to Magnetic Materials*. Wiley-IEEE Press, 2008, p. 544.

[117] S. S. P. Parkin, N. More, and K. P. Roche, "Oscillations in exchange coupling and magnetoresistance in metallic superlattice structures: Co/Ru, Co/Cr, and Fe/Cr," *Physical Review Letters,* vol. 64, no. 19, pp. 2304-2307, 05/07/ 1990.

[118] G. Vallejo-Fernandez, L. E. Fernandez-Outon, and K. O'Grady, "Measurement of the anisotropy constant of antiferromagnets in metallic polycrystalline exchange biased systems," *Applied Physics Letters,* vol. 91, no. 21, p. 212503, 2007.

[119] P. Merodio *et al.*, "Penetration depth and absorption mechanisms of spin currents in $Ir_{20}Mn_{80}$ and $Fe_{50}Mn_{50}$ polycrystalline films by ferromagnetic resonance and spin pumping," *Applied Physics Letters,* vol. 104, no. 3, p. 032406, 2014.

[120] E. C. Stoner and E. P. Wohlfarth, "A Mechanism of Magnetic Hysteresis in Heterogeneous Alloys," *Philosophical Transactions of the Royal Society of London. Series A, Mathematical and Physical Sciences,* vol. 240, no. 826, pp. 599-642, 1948.

[121] W. H. Meiklejohn, "Exchange Anisotropy—A Review," in *Proceedings of the Seventh Conference on Magnetism and Magnetic Materials*, J. A. Osborn, Ed. Boston, MA: Springer US, 1962, pp. 1328-1335.
[122] U. Nowak, K. D. Usadel, J. Keller, P. Miltényi, B. Beschoten, and G. Güntherodt, "Domain state model for exchange bias. I. Theory," *Physical Review B,* vol. 66, no. 1, p. 014430, 07/17/ 2002.
[123] E. Fulcomer and S. H. Charap, "Thermal fluctuation aftereffect model for some systems with ferromagnetic-antiferromagnetic coupling," *Journal of Applied Physics,* vol. 43, no. 10, pp. 4190-4199, 1972.
[124] W. F. Brown, "Thermal Fluctuations of a Single-Domain Particle," *Physical Review,* vol. 130, no. 5, pp. 1677-1686, 06/01/ 1963.
[125] G. Vallejo-Fernandez, N. P. Aley, J. N. Chapman, and K. O’Grady, "Measurement of the attempt frequency in antiferromagnets," *Applied Physics Letters,* vol. 97, no. 22, p. 222505, 2010.
[126] R. Street and J. C. Woolley, "A Comparison of Magnetic Viscosity in Isotropic and Anisotropic High Coercivity Alloys," *Proceedings of the Physical Society. Section B,* vol. 69, no. 12, p. 1189, 1956.
[127] P. Gaunt, "Magnetic viscosity and thermal activation energy," *Journal of Applied Physics,* vol. 59, no. 12, pp. 4129-4132, 1986.
[128] K. O. Grady, R. Chantrell, J. Popplewell, and S. Charles, "Time dependent magnetization of a system of fine cobalt particles," *IEEE Transactions on Magnetics,* vol. 17, no. 6, pp. 2943-2945, 1981.
[129] M. El-Hilo, K. O'Grady, and R. W. Chantrell, "The ordering temperature in fine particle systems," *Journal of Magnetism and Magnetic Materials,* vol. 117, no. 1, pp. 21-28, 1992/11/01 1992.
[130] T. Hughes, H. Laidler, and K. O’Grady, "Thermal activation of magnetization reversal in spin-valve systems," *Journal of Applied Physics,* vol. 89, no. 10, pp. 5585-5591, 2001.
[131] P. A. A. v. d. Heijden, T. F. M. M. Maas, W. J. M. d. Jonge, J. C. S. Kools, F. Roozeboom, and P. J. v. d. Zaag, "Thermally assisted reversal of exchange biasing in NiO and FeMn based systems," *Applied Physics Letters,* vol. 72, no. 4, pp. 492-494, 1998.
[132] G. Vallejo-Fernandez, N. P. Aley, L. E. Fernandez-Outon, and K. O’Grady, "Control of the setting process in CoFe/IrMn exchange bias systems," *Journal of Applied Physics,* vol. 104, no. 3, p. 033906, 2008.
[133] L. E. Fernández-Outón, K. O’Grady, and M. J. Carey, "Thermal phenomena in IrMn exchange biased systems," *Journal of Applied Physics,* vol. 95, no. 11, pp. 6852-6854, 2004.
[134] S. Chikazumi, *Physics of magnetism*. Wiley, 1964.
[135] H. Sang, Y. W. Du, and C. L. Chien, "Exchange coupling in $Fe_{50}Mn_{50}/Ni_{81}Fe_{19}$ bilayer: Dependence on antiferromagnetic layer thickness," *Journal of Applied Physics,* vol. 85, no. 8, pp. 4931-4933, 1999.
[136] T. Ambrose and C. L. Chien, "Dependence of exchange coupling on antiferromagnetic layer thickness in NiFe/CoO bilayers," *Journal of Applied Physics,* vol. 83, no. 11, pp. 6822-6824, 1998.
[137] H. Uyama, Y. Otani, K. Fukamichi, O. Kitakami, Y. Shimada, and J.-i. Echigoya, "Effect of antiferromagnetic grain size on exchange-coupling field of $Cr_{70}Al_{30}/Fe_{19}Ni_{81}$ bilayers," *Applied Physics Letters,* vol. 71, no. 9, pp. 1258-1260, 1997.

[138] G. Vallejo-Fernandez, L. E. Fernandez-Outon, and K. O. Grady, "Antiferromagnetic grain volume effects in metallic polycrystalline exchange bias systems," *Journal of Physics D: Applied Physics,* vol. 41, no. 11, p. 112001, 2008.
[139] G. Vallejo-Fernandez, B. Kaeswurm, and K. O'Grady, "Defect and impurity effects in exchange bias systems," *Journal of Applied Physics,* vol. 109, no. 7, p. 07D738, 2011.
[140] Y. P. Varshni, "Van der Waals' a and Ionization Potential of Inert Gases," *The Journal of Chemical Physics,* vol. 21, no. 6, pp. 1119-1119, 1953.
[141] P. J. Kelly and R. D. Arnell, "Magnetron sputtering: a review of recent developments and applications," *Vacuum,* vol. 56, no. 3, pp. 159-172, 3// 2000.
[142] R. A. Surmenev, "A review of plasma-assisted methods for calcium phosphate-based coatings fabrication," *Surface and Coatings Technology,* vol. 206, no. 8–9, pp. 2035-2056, 1/15/ 2012.
[143] G. S. Anderson, W. N. Mayer, and G. K. Wehner, "Sputtering of Dielectrics by High-Frequency Fields," *Journal of Applied Physics,* vol. 33, no. 10, pp. 2991-2992, 1962.
[144] P. D. Davidse, "Theory and practice of RF sputtering," *Vacuum,* vol. 17, no. 3, pp. 139-145, 1967/03/01 1967.
[145] M. Vopsaroiu, G. V. Fernandez, M. J. Thwaites, J. Anguita, P. J. Grundy, and K. O. Grady, "Deposition of polycrystalline thin films with controlled grain size," *Journal of Physics D: Applied Physics,* vol. 38, no. 3, p. 490, 2005.
[146] S. P. Edgar, S. P. Javier, J. M. J. Garcia, and J. L. Fernando, "Chemical Vapor Deposition of Aluminum Oxide Thin Films Using a Low-cost Direct Liquid Injection Delivery System: An Educational Laboratory Experiment," *World Journal of Chemical Education,* vol. 4, no. 4, pp. 76-79, 2016.
[147] J. Sagar *et al.*, "Effect of Seed Layers on Polycrystalline Co_2FeSi Thin Films," *IEEE Transactions on Magnetics,* vol. 48, no. 11, pp. 4006-4009, 2012.
[148] H. Endo, A. Hirohata, J. Sagar, L. R. Fleet, T. Nakayama, and K. O. Grady, "Effect of grain size on exchange-biased Heusler alloys," *Journal of Physics D: Applied Physics,* vol. 44, no. 34, p. 345003, 2011.
[149] J. Balluff, M. Meinert, J.-M. Schmalhorst, G. Reiss, and E. Arenholz, "Exchange bias in epitaxial and polycrystalline thin film Ru_2MnGe/Fe bilayers," *Journal of Applied Physics,* vol. 118, no. 24, p. 243907, 2015.
[150] M. Meinert, B. Büker, D. Graulich, and M. Dunz, "Large exchange bias in polycrystalline MnN/CoFe bilayers at room temperature," *Physical Review B,* vol. 92, no. 14, p. 144408, 10/08/ 2015.
[151] P. J. Flanders, "An alternating-gradient magnetometer (invited)," *Journal of Applied Physics,* vol. 63, no. 8, pp. 3940-3945, 1988.
[152] K. O'Grady, V. G. Lewis, and D. P. E. Dickson, "Alternating gradient force magnetometry: Applications and extension to low temperatures (invited)," *Journal of Applied Physics,* vol. 73, no. 10, pp. 5608-5613, 1993.
[153] H. Zijlstra, "A Vibrating Reed Magnetometer for Microscopic Particles," *Review of Scientific Instruments,* vol. 41, no. 8, pp. 1241-1243, 1970.
[154] J. Mallinson, "Magnetometer Coils and Reciprocity," *Journal of Applied Physics,* vol. 37, no. 6, pp. 2514-2515, 1966.

[155] K. O. Grady, R. W. Chantrell, and I. L. Sanders, "Magnetic characterisation of thin film recording media," *IEEE Transactions on Magnetics,* vol. 29, no. 1, pp. 286-291, 1993.
[156] K. Inaba, "X-ray thin-film measurement techniques," *The Rigaku Journal,* vol. 24, no. 1, pp. 10-12, 2008.
[157] T. Mitsunaga, "X-ray thin-film measurement techniques," *The Rigaku Journal,* vol. 25, no. 1, pp. 7-10, 2009.
[158] T. Konya, "X-ray thin-film measurement techniques III. High resolution X-ray diffractometry," *The Rigaku Journal,* vol. 25, no. 2, pp. 1-8, 2009.
[159] S. Kobayashi, "X-ray tun film measurement techniques IV. In-plane XRD measurements," *The Rigaku Journal,* vol. 26, no. 1, pp. 3-11, 2010.
[160] K. Nagao and E. Kagami, "X-ray thin film measurement techniques VII. Pole figure measurement," *The Rigaku Journal,* vol. 27, no. 2, pp. 6-14, 2011.
[161] B. E. Warren, *X-ray diffraction*. Reading, Mass.: Addison-Wesley Pub. Co., 1969.
[162] F. T. L. Muniz, M. A. R. Miranda, C. M. dos Santos, and J. M. Sasaki, "The Scherrer equation and the dynamical theory of X-ray diffraction," (in English), *Acta Crystallographica a-Foundation and Advances,* Article vol. 72, pp. 385-390, May 2016.
[163] H. Borchert *et al.*, "Determination of nanocrystal sizes: A comparison of TEM, SAXS, and XRD studies of highly monodisperse $COPt_3$ particles," (in English), *Langmuir,* Article vol. 21, no. 5, pp. 1931-1936, Mar 2005.
[164] J. Goldstein, *Scanning Electron Microscopy and X-ray Microanalysis: Third Edition*. Plenum, 2003.
[165] Wittke H. J. (10.04.2017). *Introduction to scanning electron microscopes*. Available: http://nau.edu/CEFNS/Labs/Electron-Microprobe/GLG-510-Class-Notes/Instrumentation/#Intro
[166] D. B. Williams and C. B. Carter, *Transmission Electron Microscopy: A Textbook for Materials Science* (no. v. 2). Springer, 2009.
[167] P. D. Nellist, "The Principles of STEM Imaging," in *Scanning Transmission Electron Microscopy: Imaging and Analysis*, S. J. Pennycook and P. D. Nellist, Eds. New York, NY: Springer New York, 2011, pp. 91-115.
[168] H. S. v. Harrach, P. Dona, B. Freitag, H. Soltau, A. Niculae, and M. Rohde, "An integrated multiple silicon drift detector system for transmission electron microscopes," *Journal of Physics: Conference Series,* vol. 241, no. 1, p. 012015, 2010.
[169] P. D. Prewett and E. M. Kellogg, "Liquid metal ion sources for FIB microfabrication systems — recent advances," *Nuclear Instruments and Methods in Physics Research Section B: Beam Interactions with Materials and Atoms,* vol. 6, no. 1, pp. 135-142, 1985/01/01 1985.
[170] I. Galanakis and E. Şaşıoğlu, "Structural-induced antiferromagnetism in Mn-based full Heusler alloys: The case of Ni_2MnAl," *Applied Physics Letters,* vol. 98, no. 10, p. 102514, 2011.
[171] K. Özdoğan and I. Galanakis, "First-principles electronic and magnetic properties of the half-metallic antiferromagnet Cr_2MnSb," *Journal of Magnetism and Magnetic Materials,* Article vol. 321, no. 15, 2009.
[172] W. R. L. Lambrecht, M. Prikhodko, and M. S. Miao, "Electronic structure and magnetic interactions in MnN and Mn_3N_2," *Physical Review B,* vol. 68, no. 17, p. 174411, 11/07/ 2003.

[173] M. A. Herman, W. Richter, and H. Sitter, *Epitaxy: Physical Principles and Technical Implementation*. Springer Berlin Heidelberg, 2004.
[174] P. Stadelmann.
[175] T. Tsuchiya, T. Kubota, T. Sugiyama, T. Huminiuc, A. Hirohata, and K. Takanashi, "Exchange bias effects in Heusler alloy Ni_2MnAl/Fe bilayers," *Journal of Physics D: Applied Physics,* vol. 49, no. 23, p. 235001, 2016.
[176] J.-I. Hong, T. Leo, D. J. Smith, and A. E. Berkowitz, "Enhancing Exchange Bias with Diluted Antiferromagnets," *Physical Review Letters,* vol. 96, no. 11, p. 117204, 03/21/ 2006.
[177] S. Blomeier *et al.*, "Structural analysis of ion irradiated polycrystalline NiFe/FeMn exchange bias systems," (in English), *The European Physical Journal B - Condensed Matter and Complex Systems,* vol. 45, no. 2, pp. 213-218, 2005/05/01 2005.
[178] Balluff J., Huminiuc T., Meinert M., Reiss G., and Hirohata A., "Integration of antiferromagnetic Ru_2MnGe Heusler compound into spintronic devices," *Submitted for publication,* 2017.
[179] R. Yu, X. Chong, Y. Jiang, R. Zhou, W. Yuan, and J. Feng, "The stability, electronic structure, elastic and metallic properties of manganese nitrides," *RSC Advances,* 10.1039/C4RA10914G vol. 5, no. 2, pp. 1620-1627, 2015.